Thermal Science and Engineering

EnPress

https://systems.enpress-publisher.com/index.php/TSE

2024 Volume 7 Issue 2
ISSN: 2578-1782 (Online)

Editorial Board

Editor-in-Chief

Associate Editors

Editorial Board Members

Volume 7 Issue 2 • 2024

Thermal Science and Engineering

EnPress Publisher

EnPress Publisher

2024 | Volume 7 | Issue 2

Thermal Science and Engineering

https://systems.enpress-publisher.com/index.php/TSE

Contents

Articles

Reviews

Thermal Science and Engineering 2024, 7(2), 6914.
https://doi.org/10.24294/tse.v7i2.6914

Article

Numerical heat transfer enhancement in MHD boundary layer flow with Darcy-Forchheimer Bioconvection Nanofluid

Umar Farooq[1,*], Tao Liu[1], Umer Farooq[2]

[1] State Key Laboratory of Fluid Power and Mechatronic Systems, School of Mechanical Engineering, Zhejiang University, Hangzhou 310058, China
[2] College of Mathematical Science, Harbin Engineering University, Harbin city 150001, China
*** Corresponding author:** Umar Farooq, umar_f@zju.edu.cn

CITATION

Farooq U, Liu T, Farooq U. Numerical heat transfer enhancement in MHD boundary layer flow with Darcy-Forchheimer Bioconvection Nanofluid. Thermal Science and Engineering. 2024; 7(2): 6914. https://doi.org/10.24294/tse.v7i2.6914

ARTICLE INFO

Received: 27 February 2024
Accepted: 11 April 2024
Available online: 25 April 2024

Abstract: Scientists have harnessed the diverse capabilities of nanofluids to solve a variety of engineering and scientific problems due to high-temperature predictions. The contribution of nanoparticles is often discussed in thermal devices, chemical reactions, automobile engines, fusion processes, energy results, and many industrial systems based on unique heat transfer results. Examining bioconvection in non-Newtonian nanofluids reveals diverse applications in advanced fields such as biotechnology, biomechanics, microbiology, computational biology, and medicine. This study investigates the enhancement of heat transfer with the impact of magnetic forces on a linearly stretched surface, examining the two-dimensional Darcy-Forchheimer flow of nanofluids based on blood. The research explores the influence of velocity, temperature, concentration, and microorganism profile on fluid flow assumptions. This investigation utilizes blood as the primary fluid for nanofluids, introducing nanoparticles like zinc oxide (ZnO) and titanium dioxide (TiO_2). The study aims to explore their interactions and potential applications in the field of biomedicine. In order to streamline the complex scheme of partial differential equations (PDEs), boundary layer assumptions are employed. Through appropriate transformations, the governing partial differential equations (PDEs) and their associated boundary conditions are transformed into a dimensionless representation. By employing a local non-similarity technique with a second-degree truncation and utilizing MATLAB's built-in finite difference code (bvp4c), the modified model's outcomes are obtained. Once the calculated results and published results are satisfactorily aligned, graphical representations are used to illustrate and analyze how changing variables affect the fluid flow characteristics problems under consideration. In order to visualize the numerical variations of the drag coefficient and the Nusselt number, tables have been specially designed. Velocity profile of ZnO-blood and TiO_2-blood decreases for increasing values of $M, \lambda,$ and F_r, while temperature profile increases for increasing values of $M, \lambda,$ and Ec. Concentration profile decreases for increasing values of S_c, and microorganism profile increases for increasing values of Pe. For rising values of M, λ and F_r the drag coefficient increases and the Nusselt number decreases for rising values of M, λ, Ec and Q. The model introduces a novel approach by conducting a non-similar analysis of the Darchy-Forchheimer bioconvection flow of a two-dimensional blood-based nanofluid in the presence of a magnetic field.

Keywords: Bioconvection; MHD; Darcy-Forchheimer; non-similar modeling, bvp4c

1. Introduction

Nanofluids have a range of applications in engineering and biomedicine, including increasing the heat conductivity of fundamental fluids like ethylene glycol, water, kerosene, and others. These applications span the manufacturing industries, treatment for cancer, and conditioning. Buongiorno and Hu [1] conducted research on

the enhancement of nanofluid heat transfer for nuclear reactor applications. Buongiorno [2] conducted an extensive study that explored convective transport in nanofluids. The impact of nanofluids thermophysical characteristics on convective heat transfer was explored by Daungthongsuk and Wongwises [3]. Khan and Ali [4] investigated that the non-Newtonian behavior of power-law fluids and wall sliding conditions influences thermal and flow properties such as temperature distribution and viscous heating effects. Ali et al. [5] used a numerical solution based on the Carreau model to critically analyze the flow of a generalized Newtonian fluid over a nonlinearly stretched curved surface. Their research focused on understanding fluid behavior under different shear rates, as well as the effect of surface curvature on flow properties. Mehmood et al. [6] studied the complicated dynamics of these nanotube fluids, especially the effect of activation energy on quaternary autocatalytic exothermic and endothermic chemical processes.

The focus of the field of magneto-hydrodynamics (MHD) is the study of the intricate interaction between magnets and electrically conducting fluids. Due to its extensive practical applications in the chemical and mechanical sectors, this field of study has garnered significant interest. The analysis of MHD's impact on heat transfer and fluid flow over surfaces that are stretched linearly or nonlinearly has received a lot of attention. A comprehensive review conducted by Kandasamy et al. [7] encompassed various investigations that inspected the effect of magnetic fields and various hydrodynamic and thermal boundary conditions on fluid flow across a stretched sheet. Crane [8] published the first analytical solution for the flow of an incompressible viscous liquid over an expanding sheet. Yazdi et al. [9] focused on studying the Magnetohydrodynamic flow and heat transmission through a non-linear porous stretched sheet while considering chemical changes and partial slip. Farooq et al. [10] investigated the MHD flow of a Casson nanofluid with nanoparticles over an extending sheet. Abouasbe et al. [11] investigate the idea of soft solutions in the context of time-fractional Navier-Stokes equations, accounting for the impact of MHD effects. This study investigates the complicated dynamics of MHD in fluid systems.

In the past few decades, substantial advancements have been achieved in the investigation of boundary layer flow and thermal expansion over a extending sheet. This is particularly noteworthy because the findings have numerous practical applications in various industries and technological fields. Several examples include the refrigeration of an unending metal plate within a freezing vessel, the boundary layer along the material conveyor, the flow of liquid film during condensation procedures, cable rolling, paper manufacturing, heated rolling, glass manipulation, and the drawing of plastic foil. The focus of Magyari and Keller [12] was on examining how heat moves in a boundary layer flow due to an exponentially continuous stretching panel without any changes in fluid properties, while also exploring the use of magnetohydrodynamic (MHD). The findings of this study have wide-ranging applications in different environmental and industrial systems, including the design of heat transfer mechanisms, catalytic reactors, geothermal systems, and geophysics. These systems typically involve the saturation of porous materials.

Porous medium flow offers numerous benefits across a diverse range of applications, encompassing fermentation, grain storage, reservoir movement, groundwater contamination, petroleum production, fossil fuel systems, energy storage

units, nuclear waste disposal, solar panels, oil resources, groundwater sources, and beyond. Although Darcy's theory [13] formed the foundation for numerous investigations on porous media with low porosity and fluid velocities, it had its limitations with highly permeable media and greater transportation. In situations of high flow rates, the conventional Darcy's law did not consider inertial and edge effects. Thus, Darcy's theory was unsuitable for describing the physical conditions of high-porosity media and velocities. Forchheimer [14] suggested adding a squared flow velocity to the Darcy velocity model to overcome this drawback and allow for the investigation of both boundary parameters and inertia. An inclined stretching sheet with an associated magnetic field in a non-Darcy permeable medium was examined by Wang et al. [15].

The movement of motile microorganisms collectively induces bioconvection, which in turn generates macroscopic convective fluid motion due to density gradients. Bioconvection occurs when self-propelled microorganisms swim in a specific direction, causing an increase in the density of the underlying fluid. Hady et al. [16] examined natural convection around a vertically oriented cone immersed in a permeable medium saturated with gyrotactic microorganisms in a non-Darcian nanofluid. Several researchers [17–28] have explored different systems to comprehend the mechanisms governing the directional motion exhibited by various microorganisms. The researchers confirmed that the presence of self-propelled microorganisms in these nanofluids promotes fluid mixing and inhibits the clustering of nanoparticles, resulting in significant fluid motion at a broader scale in their investigation of nanofluids including bacteria.

Meta-intransitive systems can improve the understanding and optimization of hydrodynamics in porous media under Darcy-Forchheimer bioconvection nanofluids. Researchers can better explain and anticipate complex processes by taking into account nontransitive features such as variable nanoparticle interactions and flow dynamics. This understanding is critical for applications in sectors such as environmental engineering and biotechnology, where precise control of fluid flow and particle movement is required. Metaintransitive systems also pose significant challenges and opportunities in decision theory, game theory, and more complex systems. Incorporating intransitive preferences into the decision-making process is critical to conducting effective multicriteria analysis. Meta-intransitive strategies in game theory can lead to complex interaction structures and consequences that influence strategic decision making. Meta-intransitive qualities also provide insights into new phenomena such as autonomy and patterning that shed light on the dynamics of coupled systems.

The upper bound problem in the Darcy–Forchheimer theory of bioconvection nanofluids is a key problem with important implications. Its resolution can improve the theoretical framework and provide a deeper understanding of the behavior of nanofluids in various situations. Researchers can improve the performance and efficiency of nanofluid-based systems by setting the maximum achievable values of important parameters such as fluid velocity, temperature, nanoparticle concentration, and microbial behavior. Solving this problem is critical to advancing scientific knowledge and practical applications in fields such as environmental engineering, medicine, and nanomaterials.

Many real-life scenarios are intrinsically unique, and this article offers a novel perspective. The non-dimensionalization technique, which uses non-similarity transformations, is more physics-based and accountable. Our key goal is to properly handle non-similar phrases resulting from similarity modifications. To the author's knowledge, no earlier academic works have explored bioconvective nanofluid flow across a stretched surface with temperature-dependent viscosity, as indicated by the literature survey. In our future initiatives, we intend to integrate this research with the subject of Mechatronics, concentrating on the creation and improvement of advanced systems. Our primary focus is on biomedical equipment and biomechanics. This multidisciplinary collaboration has enormous potential since it leverages the information created by our research to promote pioneering solutions that promise in healthcare and biotech. Our goal is to help translate theoretical discoveries into real-world uses, making major contributions to technological advances.

With a keen interest in the aforementioned discoveries and their increasing applicability across various industries, such as engineering, biochemical mechanisms, and biological sciences, our objective is to explore the non-similar analysis of MHD boundary layer flow involving Darcy-Forchheimer convection nanofluids. Specifically, we are concentrating on a flow consisting predominantly of two different nanoparticles, namely ZnO and TiO_2, combined with blood as the base fluid. The addition of ZnO and TiO_2 nanoparticles to blood-base fluid results in a complicated interaction between nanoparticles and the biological system. These nanoparticles, which have a wide range of uses, interact differently inside the circulation due to characteristics such as dimension, chemistry of the surface, and biological compatibility. Knowing these interactions is critical for investigating possible biological applications such as medication administration and medical imaging, while taking into account both the benefits and drawbacks of nanoparticle-blood interactions. To account for the influence of the magnetic field, heat generation, and porosity, we have employed the single-phase nanofluid model developed by Tiwari and Das [29]. The control system has been transformed into a non-similar configuration using suitable transformations. To solve the modified equations, we employed the local non-similarity technique (LNS) developed by Sparrow and Yu [30] and the bvp4c package within the MATLAB computational software. As far as our understanding goes, no prior research has been conducted on this subject. A graphical analysis has been employed to comprehensively examine the effects of dimensionless growth factors on velocity, energy, concentration, and microorganism profiles. Additionally, we present a further numerical investigation of skin friction, the local Nusselt number, and microorganism flux using appropriate methods.

2. Problem formulation

Consider the flow of an incompressible MHD nanofluid in a steady two-dimensional boundary layer containing nanoparticles of titanium dioxide (TiO_2) and zinc oxide (ZnO) disseminated in the base liquid (blood) over a linearly stretched surface with Darcy-Forchheimer bioconvection nanofluids. The Darcy Forchheimer model is employed to explain the porous media. The velocity of the stretched fluid, denoted as U_w, is aligned with the stretched surface, while the ambient velocity

remains at zero and the ambient temperature is equivalent to T_∞. $F = \frac{C_b}{\sqrt{k}}$ denoted the porous material inertial coefficient, The variables $T, C,$ and n represent fluid temperature, nanoparticle concentration, and microbe distribution function, respectively. Additionally, the stretched surface is positioned perpendicular to the applied magnetic field B_o. Furthermore, the influence of both porosity and the heat source is considered. **Figure 1** presented illustrates the flow configuration and flow chart of the current investigation. The equations that describe the conservation of mass, momentum, energy, concentration, and microorganism within the boundary layer are also included [10,25,31].

$$\frac{\partial u}{\partial x} + \frac{\partial v}{\partial y} = 0, \tag{1}$$

$$\rho_{nf}\left(u\frac{\partial u}{\partial x} + v\frac{\partial u}{\partial y}\right) = \mu_{nf}\frac{\partial^2 u}{\partial y^2} - \sigma_{nf}B_o^2 u - \frac{\mu_{nf}}{K}u - Fu^2, \tag{2}$$

$$(\rho c_P)_{nf}\left(u\frac{\partial T}{\partial x} + v\frac{\partial T}{\partial y}\right) = k_{nf}\frac{\partial^2 T}{\partial y^2} + \sigma_{nf}(uB_o)^2 + \frac{\mu_{nf}}{K}u^2 + Q_o(T - T_\infty) + Fu^3 \tag{3}$$

$$u\frac{\partial C}{\partial x} + v\frac{\partial C}{\partial y} = D_{nf}\frac{\partial^2 C}{\partial y^2} - K_o(C - C_\infty) + \frac{D_m}{T_m}K_T\frac{\partial^2 T}{\partial y^2}, \tag{4}$$

$$u\frac{\partial n}{\partial x} + v\frac{\partial n}{\partial y} = D_m\frac{\partial^2 n}{\partial y^2} + \frac{bW_c}{(C_w - C_\infty)}\left(\frac{\partial}{\partial y}\left(n\frac{\partial C}{\partial y}\right)\right). \tag{5}$$

Associated boundaries [32] are:

$$\begin{gathered} u = U_w = ax,\ v = v_w = 0,\ T = T_w,\ C = C_w,\ n = n_w,\ at\ y = 0, \\ u \to 0, n \to n_\infty, T \to T_\infty, C \to C_\infty\ as\ y \to \infty. \end{gathered} \tag{6}$$

Here, Equation (1) represents the continuity equation based on the law of conservation of mass; Equation (2) is the momentum equation based on Newton's second law of motion; Equation (3) is the energy equation based on the first law of thermodynamics; Equation (4) is the concentration equation or advection-diffusion equation based on the law of conservation of mass for the scalar quantity; and Equation (5) is the microorganisms equation, which is based on the law of conservation of mass for microorganisms, random motility, and chemotaxis. The associated boundary conditions at the wall surface and far away from the wall are given in Equation (6).

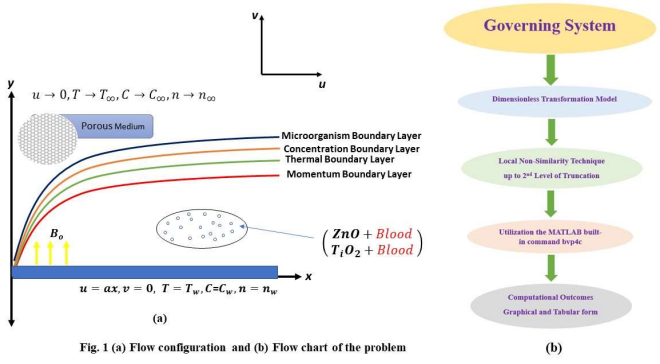

Fig. 1 (a) Flow configuration and (b) Flow chart of the problem

Figure 1. (a) Flow configuration and **(b)** Flow chart of the problem.

Introducing $\xi(x)$ and $\eta(x, y)$ as new terms to create a non-similar flow.

$$\xi = \frac{x}{l},\ \eta = \sqrt{\frac{c}{\upsilon_f}}y, u = cx\frac{\partial f(\xi,\eta)}{\partial \eta},\ v = -\sqrt{\upsilon_f c}\left(\frac{\partial f(\xi,\eta)}{\partial \xi}\xi + f(\xi,\eta)\right),$$
$$\theta(\xi,\eta) = \frac{T - T_\infty}{T_w - T_\infty}, \qquad \varphi(\xi,\eta) = \frac{C - C_\infty}{C_w - C_\infty}, \qquad \chi(\xi,\eta) = \frac{\mathrm{n} - n_\infty}{n_w - n_\infty} \tag{7}$$

Utilizing Equation (7), Equation (1) is perfectly satisfied given the above transformations, while Equations (2)– (5) become:

$$\frac{\mu_{nf}}{\mu_f}\frac{\partial^3 f}{\partial \eta^3} - \frac{\sigma_{nf}}{\sigma_f}M\frac{\partial f}{\partial \eta} - \frac{\mu_{nf}}{\mu_f}\lambda\frac{\partial f}{\partial \eta} - \left(\frac{\partial f}{\partial \eta}\right)^2\left(\frac{\rho_{nf}}{\rho_f} + F_r\right) + \frac{\rho_{nf}}{\rho_f}f\frac{\partial^2 f}{\partial \eta^2} = \xi\frac{\rho_{nf}}{\rho_f}\left(\frac{\partial f}{\partial \eta}\frac{\partial^2 f}{\partial \xi \partial \eta} - \frac{\partial f}{\partial \xi}\frac{\partial^2 f}{\partial \eta^2}\right), \tag{8}$$

$$\frac{k_{nf}}{k_f}\frac{\partial^2 \theta}{\partial \eta^2} + PrEc\xi^2\left(\frac{\partial f}{\partial \eta}\right)^2\left(\frac{\sigma_{nf}}{\sigma_f}M + \frac{\mu_{nf}}{\mu_f}\lambda\right) + Pr\left(Q\theta + \frac{(\rho C_p)_{nf}}{(\rho C_p)_f}f\frac{\partial \theta}{\partial \eta}\right) + \frac{(\rho C_p)_f}{(\rho C_p)_{nf}}F_r Ec\xi^3\left(\frac{\partial f}{\partial \eta}\right)^3 = Pr\xi\frac{(\rho C_p)_{nf}}{(\rho C_p)_f}\left(\frac{\partial f}{\partial \eta}\frac{\partial \theta}{\partial \xi} - \frac{\partial f}{\partial \xi}\frac{\partial \theta}{\partial \eta}\right), \tag{9}$$

$$\frac{D_{nf}}{D_f}\frac{\partial^2 \varphi}{\partial \eta^2} + S_c\left(f\frac{\partial \varphi}{\partial \eta} - K_r\varphi + S_r\frac{\partial^2 \theta}{\partial \eta^2}\right) = \xi S_c\left(\frac{\partial f}{\partial \eta}\frac{\partial \varphi}{\partial \xi} - \frac{\partial f}{\partial \xi}\frac{\partial \varphi}{\partial \eta}\right), \tag{10}$$

$$\frac{\partial^2 \chi}{\partial \eta^2} + Pe\left(\frac{\partial^2 \varphi}{\partial \eta^2}(\chi + \delta_1) + \frac{\partial \chi}{\partial \eta}\frac{\partial \varphi}{\partial \eta}\right) + fLe\frac{\partial \chi}{\partial \eta} = \xi Le\left(\frac{\partial f}{\partial \eta}\frac{\partial \chi}{\partial \xi} - \frac{\partial f}{\partial \xi}\frac{\partial \chi}{\partial \eta}\right). \tag{11}$$

The associated non-similar boundaries are as follows:

$$\frac{\partial f}{\partial \eta}(\xi,0) = 1, f(\xi,0) + \xi\frac{\partial f}{\partial \xi}(\xi,0) = 0, \theta(\xi,0) = 1, \varphi(\xi,0) = 1,\ \chi(\xi,0) = 1, \quad \text{at } \eta = 0,$$
$$\frac{\partial f}{\partial \eta}(\xi,\infty) \to 0, \chi(\xi,\infty) \to 0, \theta(\xi,\infty) \to 0, \varphi(\xi,\infty) \to 0, \text{as } \eta \to \infty. \tag{12}$$

In above equations $M, F_r, \lambda, Pr, Ec, Q, S_c, K_r, S_r, Pe, \delta_1$, $Le, f, \theta, \varphi,$ and χ represents the magnetic field parameter, Forchheimer number, Porosity parameter, Prandlt number, Eckert number, Heat source, Schmidt number, chemical response parameter, Soret number, Peclet number, microorganism difference parameter, Lewis number, dimensionless stream function, temperature, concentration, and gyrotactic microorganism respectively.

Therefore, the following parameters are defined:

$$\boldsymbol{M = \frac{\sigma_f B_0^2}{c\rho_f}} \qquad \boldsymbol{Q = \frac{Q_0}{c(\rho C_P)_f}} \qquad \boldsymbol{Pe = \frac{bW_c}{D_m}}$$
$$\boldsymbol{F_r = \frac{2Fl}{\rho_f}} \qquad S_c = \frac{\nu_f}{D_f} \qquad \delta_1 = \frac{n_\infty}{n_w - n_\infty}$$
$$\boldsymbol{Pr = \frac{\nu_f(\rho C_p)_f}{k_f}} \qquad K_r = \frac{K_o}{a} \qquad Le = \frac{\nu_f}{D_m}$$
$$\boldsymbol{Ec = \frac{c^2 l^2}{(c_p)_f(T_w - T_\infty)}} \qquad S_r = \frac{D_m K_T}{\nu T_m}\frac{(T_w - T_\infty)}{(C_w - C_\infty)}$$

A list of relevant physical quantities can be found in some references [33,34].

$$C_f = \frac{\tau_w}{\rho_f U^2{}_W}, Nu = \frac{xq_w}{k_f(T_w - T_\infty)}, \tau_w = \left(\mu_{nf}\frac{\partial u}{\partial y}\right)_{y=0}, \tag{13}$$

$$q_w = \left(k_{nf}\frac{\partial T}{\partial y}\right)_{y=0}.$$

here C_f, Nu, τ_w, and q_w represents drag coefficient, Nusselt number, surface shear stress, and surface flux.

Dimensionless form of Equation (13) is:

$$C_f(Re_x)^{\frac{1}{2}} = \xi^{-1}\frac{\partial^2 f}{\partial \eta^2}(\xi,0),\ Nu_x(Re_x)^{-\frac{1}{2}} = -\frac{k_{nf}}{k_f}\frac{\partial \theta}{\partial \eta}(\xi,0) \tag{14}$$

3. Methodology for local non-similarity

To investigate the flow of nanofluid over a stretched surface within the boundary layer, we employ the local non-similarity (LNS) method on the dimensionless governing model presented in Equation (8–11) along with the specified boundary conditions (12). In the subsequent section, a thorough, step-by-step elucidation of the LNS method applied to address the given problem will be provided.

The main advantage of LNS is that it doesn't require the resolution of other streamwise points to get non-similar solutions for any streamwise point. Furthermore, the differential equations from which these localized solutions are obtained are ordinary differential equations for computing convenience. Furthermore, this technique allows for a certain degree of precise self-validation. The preparatory process for applying the local non-similarity technique to a particular problem consists of an organized sequence of discrete phases. The actual coordinates x and y are first replaced with the carefully selected transformed coordinates ξ and η. The η coordinate, which includes y, is represented as a pseudo-similarity variable. Its main goal is to reduce the degree to which the answer depends on the streamwise variable x, in the same way that a genuine similarity variable completely eliminates x-dependency. On the other hand, the coordinate ξ depends just on x, and it is frequently used in many problems as a dimensionless representation of x. Because the resultant equations effectively become ordinary differential equations, the computing complexity is decreased by eliminating terms involving $\frac{\partial}{\partial \xi}(.)$. This simplifying also removes the streamwise connection, allowing locally independent solutions to be achieved. While there are computational benefits to this "local similarity" technique, the correctness of the findings may not always be guaranteed.

3.1. First level of truncation

Considering the term ξ are significantly smaller than one at the first truncation level, the right-hand sides of Equations (8–11) become zero. This results in the modified system of equations taking the following form.

$$\frac{\mu_{nf}}{\mu_f}(f''' - \lambda f') - \frac{\sigma_{nf}}{\sigma_f}Mf' + \frac{\rho_{nf}}{\rho_f}(ff'' - (f')^2) - (f')^2 F_r = 0, \tag{15}$$

$$\begin{aligned}\frac{k_{nf}}{k_f}\theta'' + PrEc\xi^2(f')^2\left(\frac{\sigma_{nf}}{\sigma_f}M + \frac{\mu_{nf}}{\mu_f}\lambda\right) + Pr\left(Q\theta + \frac{(\rho C_p)_{nf}}{(\rho C_p)_f}f\theta'\right) \\ + \frac{(\rho C_p)_f}{(\rho C_p)_{nf}}F_r Ec\xi^3(f')^3 = 0,\end{aligned} \tag{16}$$

$$\frac{D_{nf}}{D_f}\varphi'' + S_c(f\varphi' - K_r\varphi + S_r\theta'') = 0, \tag{17}$$

$$\chi'' + Pe(\varphi''(\chi + \delta_1) + \chi'\varphi') + fLe\chi' = 0. \tag{18}$$

With boundary conditions,

$$\begin{gathered} f(\xi,0) = 0, f'(\xi,0) = 1, \theta(\xi,0) = 1, \varphi(\xi,0) = 1, \chi(\xi,0) = 1, \text{at } \eta = 0, \\ f'(\xi,\infty) \to 0, \theta(\xi,\infty) \to 0, \varphi(\xi,\infty) \to 0, \chi(\xi,\infty) \to 0, \text{as } \eta \to \infty. \end{gathered} \tag{19}$$

3.2. Second level of truncation

To achieve a second-order truncation, it is essential to differentiate Equations (8) – (11) with respect to ξ and introduce additional functions.

In order to achieve the second degree of truncation, the following relations are incorporated:

$$\frac{\partial f}{\partial \xi} = k, \frac{\partial \theta}{\partial \xi} = l, \frac{\partial \varphi}{\partial \xi} = m, \frac{\partial \chi}{\partial \xi} = n \text{ and } \frac{\partial k}{\partial \xi} = \frac{\partial l}{\partial \xi} = \frac{\partial m}{\partial \xi} = \frac{\partial n}{\partial \xi} = 0 \tag{20}$$

Therefore, the modified system of equations at the second degree of iteration is:

$$\frac{\mu_{nf}}{\mu_f}k''' = \frac{\rho_{nf}}{\rho_f}\{3f'k' - 2kf' - fk'' + \xi((k')^2 - kk'')\} + k'\left(\frac{\sigma_{nf}}{\sigma_f}M + \frac{\mu_{nf}}{\mu_f}\lambda\right) \tag{21}$$

$$\begin{aligned} \frac{k_{nf}}{k_f}l'' = {} & -2PrEc\xi f'\left(\frac{\sigma_{nf}}{\sigma_f}M + \frac{\mu_{nf}}{\mu_f}\lambda\right)(f' + \xi k') \\ & - Pr\frac{(\rho C_p)_{nf}}{(\rho C_p)_f}\{fl' + f'l + \xi(k'l - kl')\} + PrQl' \\ & - \frac{(\rho C_p)_f}{(\rho C_p)_{nf}}3F_rEc(\xi^2(f')^3 + \xi^3(f')^2k'), \end{aligned} \tag{22}$$

$$\begin{aligned} \frac{D_{nf}}{D_f}m'' = {} & Sc(f'm - k\varphi') + \xi Sc(k'm - km') \\ & - Sc(k\varphi' + fm' - Krm + Srl''), \end{aligned} \tag{23}$$

$$n'' = Le(\xi(k'n - kn') - 2k\chi') - Pe(m''(\chi + \delta_1) + \phi''n + n'\phi' + \chi'm'). \tag{24}$$

With associated boundaries,

$$k'(\xi,0) = 0, k(\xi,0) = 0, l(\xi,0) = 0, m(\xi,0) = 0, n(\xi,0) = 0, \text{at } \eta = 0, \tag{25}$$

$$k'(\xi,\infty) \to 0, l(\xi,\infty) \to 0, m(\xi,\infty) \to 0, n(\xi,\infty) \to 0, \text{as } \eta \to \infty. \tag{26}$$

4. Result and discussion

This section presents a physical discussion using graphs that were generated to inspect the behavior of several dimensionless material variables in relation to velocity, temperature, concentration, and microorganism profiles. Each graph provides a comparison between the two nanofluids ZnO + blood and TiO_2 + blood.

Figure 2 depicts how (M) alters the velocity profile. According to research, larger values of the (M) correlate with lower velocity estimations. Magnetic fields affect fluid flow, causing the velocity profile to fall. The magnetic field creates a Lorentz force in the fluid, which opposes both the magnetic field and the direction of flow. This force stops the fluid from flowing, slows it down, and alters the flow pattern. **Figure 3** depicts the impact of porosity on velocity profiles. By raising the porosity parameter, the porous media becomes more permeable, allowing fluid to flow more

easily over it. This raises the fluid's total flow rate. The velocity profile, on the other hand, drops when the flow rate rises because the fluid's internal velocity gradient increases. **Figure 4** shows how changing the Forchheimer number affects the deviation of the velocity distribution. As the Forchheimer number increases, the effect of inertial forces on fluid flow becomes more apparent, resulting in a decrease in fluid velocity. This occurs because the fluid encounters greater resistance when passing through a porous medium due to the combined effects of viscous and inertial drag forces. The higher the Forchheimer number, the stronger the inertial effects, which leads to a decrease in flow acceleration. As a result, the fluid velocity profile is leveled out, demonstrating a more uniform velocity distribution across the flow cross-section. In addition, the boundary layer thickens, which is the region along the wall where the fluid velocity changes from zero (due to the no-slip condition at the wall) to the free-stream velocity. The thickening of the boundary layer is caused by increased drag, which greatly slows down the fluid at the wall, expanding the region over which velocity gradients can be measured.

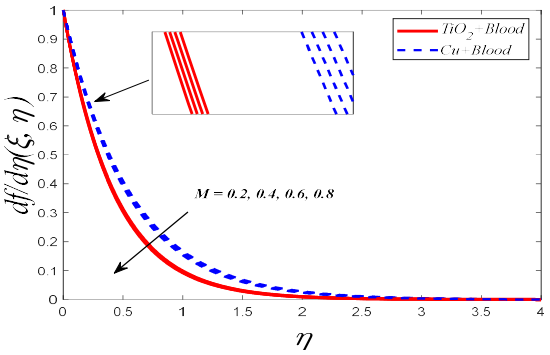

Figure 2. Variation of velocity profile with different values of "M".

If $\xi = 0.5, Q = 1.1, Ec = 1.8, Pr = 21, M = 0.25, \lambda = 1.5, F_r = 1.3, S_c = 2.8, K_r = 0.2, S_r = 0.1, Le = 0.7, \delta_1 = 0.3.$

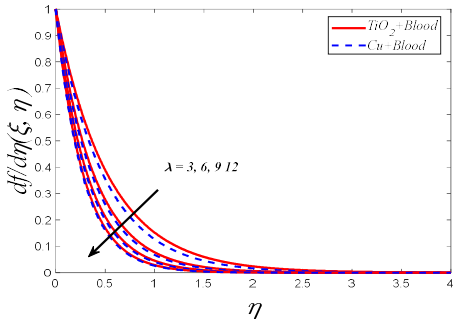

Figure 3. Variation of velocity profile with different values of λ.

If $\xi = 0.5, Q = 1.1, Ec = 1.8, Pr = 21, M = 0.25, \lambda = 1.5, F_r = 1.3, S_c = 2.8, K_r = 0.2, S_r = 0.1, Le = 0.7, \delta_1 = 0.3.$

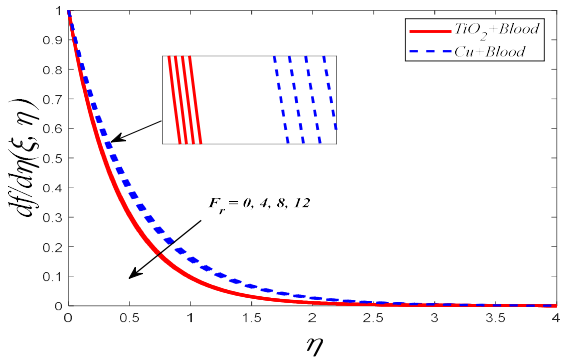

Figure 4. Variation of velocity profile with different values of F_r.

If $\xi = 0.5, Q = 1.1, Ec = 1.8, Pr = 21, M = 0.25, \lambda = 1.5, F_r = 1.3, S_c = 2.8, K_r = 0.2, S_r = 0.1, Le = 0.7, \delta_1 = 0.3$.

Figures 5–7 show that the temperature profile varies depending on the magnetic field parameter (M), porosity parameter (λ) and Eckert number (Ec).

It was found that increasing the magnetic field parameter (M) enhances the magnetic field surrounding the linearly stretched sheet. This stronger magnetic field induces an electric current in the fluid, causing the Lorentz force to resist the fluid's movement. The counteracting Lorentz force leads to an increase in the coefficient of surface friction and the rate of heat transfer on the surface of the sheet. As a result of the increase in thermal energy created by the work done against the Lorentz force, the temperature profile increases. Increasing the porosity parameter (λ) reduces the fluid flow inside the porous medium. This additional obstacle increases the velocity gradient near the linearly stretched layer, causing the fluid to take a more tortuous course. Due to higher frictional heating and viscous energy dissipation, an increase in the velocity gradient leads to an increase in the temperature gradient. As a result, when the porosity parameter increases, the temperature profile also increases. Likewise, an increase in the Eckert number (Ec) indicates that the fluid contains more kinetic energy than thermal energy. This increase in kinetic energy causes greater viscous dissipation, which converts it into thermal energy. As a result, the velocity gradient near the linearly extending sheet increases, resulting in a larger temperature difference. The conversion of kinetic energy to heat increases the temperature profile, demonstrating a clear correlation between the Eckert number and temperature rise. **Figures 8** and **9** show that the Schmidt number (S_c) and Soret number (S_r) vary throughout the concentration profile. As the Schmidt number (S_c) increases, the concentration profiles decrease. The Schmidt number is defined as kinematic viscosity (momentum diffusion coefficient)/mass diffusion coefficient. A larger Schmidt number indicates that mass diffusion is lower than momentum diffusion, meaning that mass (or species) diffuses more slowly than momentum. This reduced mass diffusion rate results in a faster decrease in nanofluid concentration, resulting in a lower concentration profile. From a physical perspective, this means that particles in a nanofluid are less likely to disperse and mix with the surrounding fluid, resulting in steeper concentration gradients and lower overall concentration levels. On the contrary, an increase in the Soret number $(S_r$)leads to an increase in the concentration profile. The Soret effect, or thermal diffusion, occurs when a temperature gradient causes mass transfer. A higher Soret number indicates that thermal diffusion is more significant

than mass diffusion. This means that temperature gradients play a large role in mass transport, causing species to migrate more efficiently from regions of higher temperature to regions of lower temperature. This thermal diffusion effect increases the nanofluid concentration, providing an additional mechanism for mass movement beyond simple mass diffusion. As a result, the concentration profile shifts, revealing greater species concentrations in locations exposed to the temperature gradient. **Figures 10** and **11** depict the dispersion of microbial profiles for different Peclet numbers (Pe) and Lewis numbers. As the Peclet number (Pe) increases, the advection of microorganisms dominates over diffusion. The Peclet number is the ratio of the rates of advective and diffusive transport. A higher Peclet number indicates that the fluid flow is effectively transporting microorganisms down the stretched sheet. This improved advective transport means that microorganisms are carried further from their original position by the fluid flow, resulting in a higher profile of microorganisms in the downstream area. In physical terms, this means that microbes are influenced more by volumetric fluid movement than by random diffusion of molecules, resulting in greater concentrations of bacteria downstream. Conversely, increasing the Lewis number (Le) makes the thermal conductivity coefficient more important than the mass diffusivity coefficient. The Lewis number is calculated as the ratio of the thermal conductivity coefficient to the mass diffusion coefficient. A higher Lewis number indicates that heat travels through the nanofluid faster than microorganisms. As a result, the nanofluid thermally diffuses faster than microorganisms. Thermal diffusion, which is more efficient, affects the temperature distribution within the liquid but does not contribute to the mobility of microbes. As a result, the concentration of microorganisms drops, resulting in a lower microbial profile. This suggests that when Lewis numbers increase, the ability of microbes to spread by diffusion decreases due to the suppressive effect of heat diffusion.

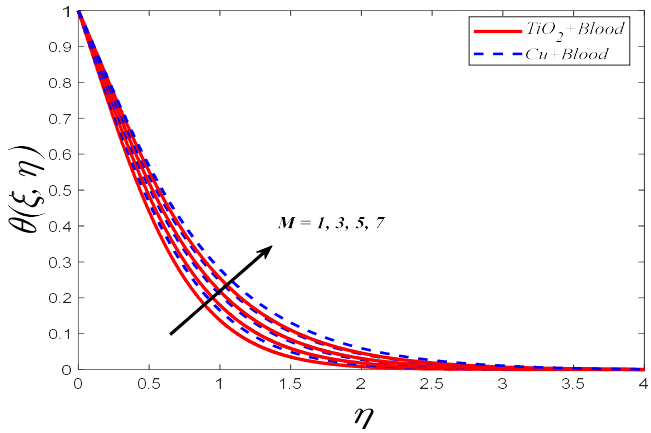

Figure 5. Variation of temperature profile with different values of "M".

If $\xi = 0.5, Q = 1.1, Ec = 1.8, Pr = 21, M = 0.25, \lambda = 1.5, F_r = 1.3, S_c = 2.8, K_r = 0.2, S_r = 0.1, Le = 0.7, \delta_1 = 0.3.$

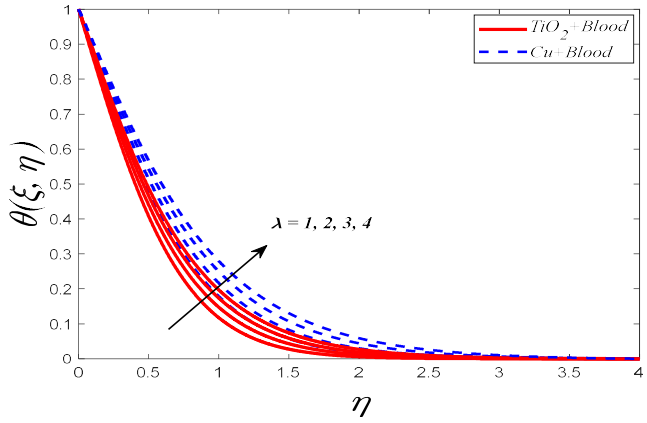

Figure 6. Variation of temperature profile with different values of "λ".

If $\xi = 0.5, Q = 1.1, Ec = 1.8, Pr = 21, M = 0.25, \lambda = 1.5, F_r = 1.3, S_c = 2.8, K_r = 0.2, S_r = 0.1, Le = 0.7, \delta_1 = 0.3.$

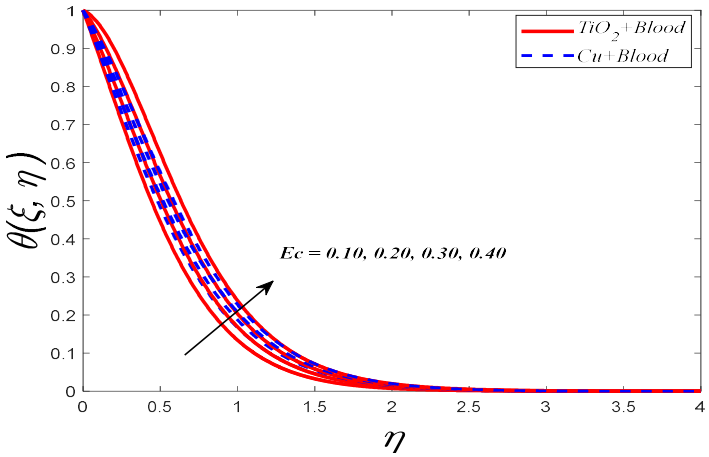

Figure 7. Variation of temperature profile with different values of "Ec".

If $\xi = 0.5, Q = 1.1, Ec = 1.8, Pr = 21, M = 0.25, \lambda = 1.5, F_r = 1.3, S_c = 2.8, K_r = 0.2, S_r = 0.1, Le = 0.7, \delta_1 = 0.3.$

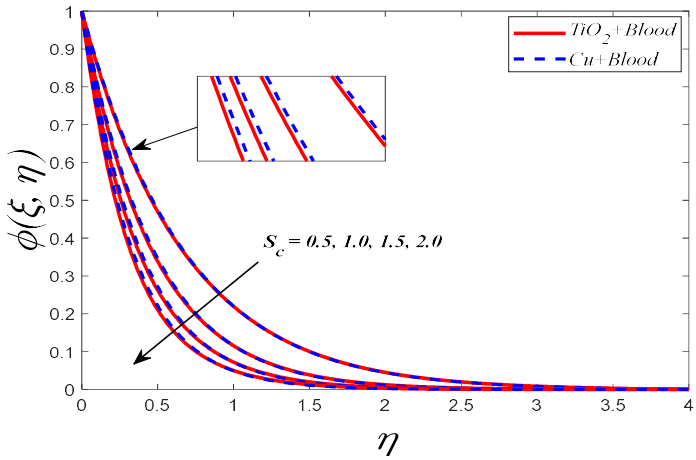

Figure 8. Variation of concentration profile with different values of "S_c".

If $\xi = 0.5, Q = 1.1, Ec = 1.8, Pr = 21, M = 0.25, \lambda = 1.5, F_r = 1.3, S_c = 2.8, K_r = 0.2, S_r = 0.1, Le = 0.7, \delta_1 = 0.3.$

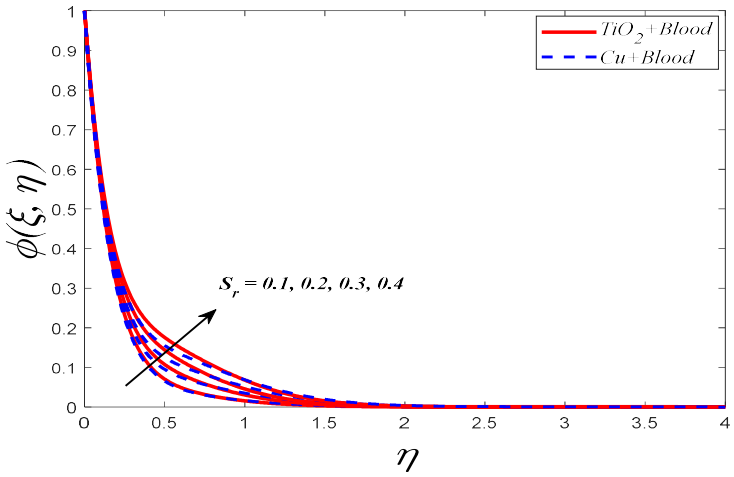

Figure 9. Variation of concentration profile with different values of "S_r".

If $\xi = 0.5, Q = 1.1, Ec = 1.8, Pr = 21, M = 0.25, \lambda = 1.5, F_r = 1.3, S_c = 2.8, K_r = 0.2, S_r = 0.1, Le = 0.7, \delta_1 = 0.3.$

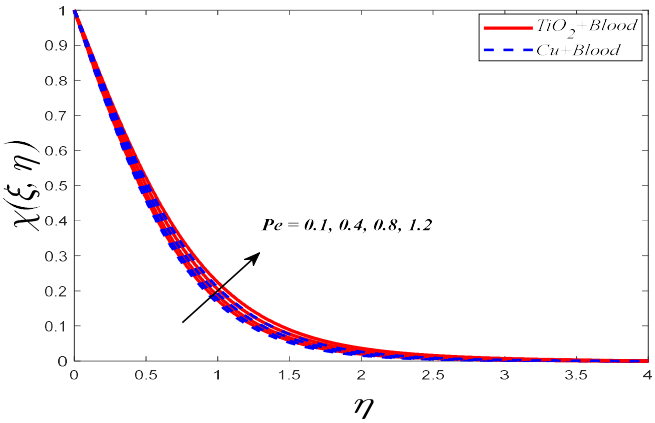

Figure 10. Variation of microorganism profile with different values of "Pe".

If $\xi = 0.5, Q = 1.1, Ec = 1.8, Pr = 21, M = 0.25, \lambda = 1.5, F_r = 1.3, S_c = 2.8, K_r = 0.2, S_r = 0.1, Le = 0.7, \delta_1 = 0.3.$

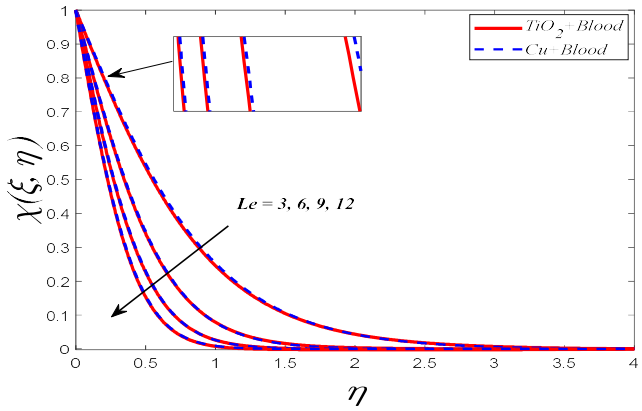

Figure 11. Variation of microorganism profile with different values of "Le".

If $\xi = 0.5, Q = 1.1, Ec = 1.8, Pr = 21, M = 0.25, \lambda = 1.5, F_r = 1.3, S_c = 2.8, K_r = 0.2, S_r = 0.1, Le = 0.7, \delta_1 = 0.3$.

Table 1 depicts the thermophysical characteristics of the nanofluid.

Table 1. The thermophysical characteristics of the nanofluid [25].

Property	Symbol	Defined
Viscosity	μ_{nf}	$\mu_{nf} = \frac{\mu_f}{(1-\phi)^{2.5}}$
Density	ρ_{nf}	$\rho_{nf} = (1-\phi)\rho_f + \phi\rho_s$
Heat Capacitance	$(\rho C_p)_{nf}$	$(\rho C_p)_{nf} = (1-\phi)(\rho C_p)_f + \phi(\rho C_p)_s$
Electric conductivity	σ_{nf}	$\sigma_{nf} = \left\{1 + \frac{3\left(\frac{\sigma_s}{\sigma_f} - 1\right)\phi}{\left(\frac{\sigma_s}{\sigma_f} + 2\right) - \left(\frac{\sigma_s}{\sigma_f} - 1\right)\phi}\right\}\sigma_f$
Thermal Conductivity	k_{nf}	$k_{nf} = \frac{(k_s + 2k_f) - 2\phi(k_f - k_s)}{(k_s + 2k_f) + \phi(k_f - k_s)}k_f$
Mass Diffusivity	D_{nf}	$D_{nf} = (1-\phi)D_f$

Table 2 presents the thermophysical properties of both base fluids and nanoparticles.

Table 2. The thermophysical characteristics of nanoparticles in conjunction with the base fluid.

Physical property	Blood	ZnO	TiO_2
$\rho(m^{-3}Kg)$	1063	5700	4250
$C_p(K^{-1}JKg^{-1})$	3594	523	686.2
$k(K^{-1}Wm^{-1})$	0.492	25	8.9538
$\sigma(\Omega.m^{-1})$	0.8	2×10^{-6}	1.0×10^{-12}

Tables 3 and **4** present a discussion on the Nusselt number and drag force coefficient responses for different parameter values.

Table 3 shows the direct relation of different parameters with $Re^{\frac{1}{2}}C_f$, as the parameters M, λ, and F_r increase, the value of $Re^{\frac{1}{2}}C_f$ also increase.

Table 3. Calculated the $-Re^{\frac{1}{2}}C_f$ values for different $M, \lambda,$ and F_r predictions, assuming ξ=0.5, and $Pr = 21$.

M	λ	F_r	ZnO + Blood	TiO_2 + Blood
0.2	0.5	0.6	0.43782910	0.40347623
0.4	0.5	0.6	0.43871489	0.40448743
0.6	0.5	0.6	0.43946105	0.40452139
0.8	0.5	0.6	0.44163052	0.40453278
0.25	1	0.6	0.01638520	0.06201482
0.25	3	0.6	0.02561956	0.06321946
0.25	5	0.6	0.02581405	0.06422105

Table 3. (*Continued*).

M	λ	F_r	ZnO + Blood	TiO_2 + Blood
0.25	7	0.6	0.02816391	0.07249543
0.25	0.5	0.5	0.13734056	0.27510531
0.25	0.5	1.0	0.14246190	0.27621021
0.25	0.5	1.5	0.14349561	0.29218945
0.25	0.5	2.0	0.15302185	0.29317220

Table 4 shows the inverse relation of different parameters with $Re^{\frac{1}{2}}Nu$, as the parameters M, λ, Ec, and Q increase, the value of $Re^{\frac{1}{2}}Nu$ decrease.

Table 4. Calculated the $-Re^{\frac{1}{2}}Nu$ values for $M, \lambda, Ec,$ and Q predictions, assuming ξ=0.5, and $Pr = 21$.

M	λ	Ec	Q	ZnO + Blood	TiO_2 + Blood
0.2	0.5	0.2	0.4	0.71026721	0.62393745
0.4	0.5	0.2	0.4	0.70827642	0.62137012
0.6	0.5	0.2	0.4	0.70472011	0.61274624
0.8	0.5	0.2	0.4	0.69321064	0.59387251
0.25	1	0.2	0.4	0.39174290	0.33865102
0.25	3	0.2	0.4	0.37812301	0.33682306
0.25	5	0.2	0.4	0.37520173	0.31852047
0.25	7	0.2	0.4	0.34193084	0.31638561
0.25	0.5	0.4	0.4	0.51030618	0.48261823
0.25	0.5	0.8	0.4	0.50593821	0.47726582
0.25	0.5	1.2	0.4	0.50262145	0.45451894
0.25	0.5	1.6	0.4	0.48923073	0.44327632
0.25	0.5	0.2	0.3	0.03914723	0.29526081
0.25	0.5	0.2	0.5	0.01736814	0.29418652
0.25	0.5	0.2	0.7	0.01519354	0.27862091
0.25	0.5	0.2	0.9	0.01284067	0.27127912

Table 5 illustrates a comparison between our study and the works done by El. Aziz [35], Loganathan and Vimla [36], and Sharma [37].

Table 5. Comparison of $-\theta'(0)$ across various values of Pr, in a scenario where Q, Ec, M and λ are all equal to zero, and ξ is set to 0.5.

Pr	El. Aziz [35]	Loganathan and Vimla [36]	Sharma [37]	Present Study
1	0.954785	0.955870	0.954788	0.955271
3	1.869074	1.868878	1.869073	1.868219
5	2.500132	2.499982	2.500121	2.522403
10	3.660372	3.660239	3.660289	3.661172

5. Conclusion

In the problem being examined, a non-similar analysis of MHD boundary layer flow with Darcy-Forchheimer bioconvection of nanofluids is proposed in the study. The study has provided insights into the impact of the nanoparticles TiO_2 and ZnO on the flow dynamics and transport phenomena within the boundary layer. Further investigations may be warranted to explore the long-term effects and potential applications of utilizing TiO_2 and ZnO in nanofluid systems, particularly in the context of medical treatments and therapies. Understanding the behavior of these particles within MHD boundary layer flows is crucial for optimizing their utilization and ensuring their safe and effective implementation in various fields. The study investigates the impact of relevant parameters on velocity, temperature, nanoparticles volume fraction, and microorganism distribution within appropriate ranges. To tackle the highly nonlinear governing system, a combination of the LNS technique and the MATLAB bvp4c (built-in package) is employed successfully. This study's findings can be summed up as follows:

- The velocity profile collapses with the higher magnetic field (M), porosity (λ), and Forchheimer number (F_r) parameters.
- By enhancing the magnetic field, porosity, and Eckert number parameters, the temperature profile improved.
- The concentration profile is reduced when the Schmidt number (Sc) is increased but improved when the Soret number (Sr) is increased.
- The microorganism's profile reduced as the Lewis number (Le) grew, whereas it increased as the Peclet number (Pe) increased.
- Increases in the magnetic field, porosity, and Forchheimer number lead to an rise in the drag coefficient.
- The local Nusselt number decreases as the magnetic field, porosity, Eckert number, and heat source increase.
- A comparative study has been conducted to bolster the current research, showcasing the coherence of the current findings.
- Future endeavors may focus on the refinement of medical imaging modalities such as magnetic resonance imaging (MRI), the optimization of radiation therapy methodologies for cancer treatment, and the incorporation of perspectives from heat transfer studies on stretched surfaces into biomedical device development, to improve both safety and effectiveness in medical era.

Author contributions: Conceptualization, methodology, software, writing, UF (Umar Farooq); supervision and project administration, TL; formal analysis, review and editing, data curation, UF (Umer Farooq). All authors have read and agreed to the published version of the manuscript.

Acknowledgments: This work was supported in part by the NSFC Grant No. 52175033 and No. U21A20120; the Key Research and Development Program of Zhejiang under awards 2022C03103 and 2021C03051. Umar Farooq, Tao Liu are with the State Key Laboratory of Fluid Power & Mechatronic Systems, School of Mechanical Engineering, Zhejiang University, 310027, Hangzhou.

Conflict of interest: The authors declare no conflict of interest.

References

1. Buongiorno J, Hu LW. Nanofluid Heat Transfer Enhancement for Nuclear Reactor Applications. Available online: https://dspace.mit.edu/handle/1721.1/65899 (accessed on 17 March 2024).
2. Buongiorno J. Convective Transport in Nanofluids. Journal of Heat Transfer. 2005; 128(3): 240-250. doi: 10.1115/1.2150834
3. Duangthongsuk W, Wongwises S. Effect of thermophysical properties models on the predicting of the convective heat transfer coefficient for low concentration nanofluid. International Communications in Heat and Mass Transfer. 2008; 35(10): 1320-1326. doi: 10.1016/j.icheatmasstransfer.2008.07.015
4. Khan MWS, Ali N. Thermal entry flow of power-law fluid through ducts with homogeneous slippery wall(s) in the presence of viscous dissipation. International Communications in Heat and Mass Transfer. 2021; 120: 105041. doi: 10.1016/j.icheatmasstransfer.2020.105041
5. Ali N, Khan MWS, Saleem S. Critical analysis of generalized Newtonian fluid flow past a non-linearly stretched curved surface: A numerical solution for Carreau model. ZAMM - Journal of Applied Mathematics and Mechanics / Zeitschrift für Angewandte Mathematik und Mechanik. 2023; 104(2). doi: 10.1002/zamm.202300100
6. Mehmood Y, Shafqat R, Sarris IE, et al. Numerical Investigation of MWCNT and SWCNT Fluid Flow along with the Activation Energy Effects over Quartic Auto Catalytic Endothermic and Exothermic Chemical Reactions. Mathematics. 2022; 10(24): 4636. doi: 10.3390/math10244636
7. Kandasamy R, Loganathan P, Arasu PP. Scaling group transformation for MHD boundary-layer flow of a nanofluid past a vertical stretching surface in the presence of suction/injection. Nuclear Engineering and Design. 2012; 241(6): 2053-2059. doi: 10.10115/2012/934964
8. Crane LJ. Flow past a stretching plate. Zeitschrift für angewandte Mathematik und Physik ZAMP. 1970; 21(4): 645-647. doi: 10.1007/bf01587695
9. Yazdi MH, Abdullah S, Hashim I, et al. Slip MHD liquid flow and heat transfer over non-linear permeable stretching surface with chemical reaction. International Journal of Heat and Mass Transfer. 2011; 54(15-16): 3214-3225. doi: 10.1016/j.ijheatmasstransfer.2011.04.009
10. Farooq U, Hussain M, Farooq U. Non-similar analysis of chemically reactive bioconvective Casson nanofluid flow over an inclined stretching surface. ZAMM - Journal of Applied Mathematics and Mechanics/Zeitschrift für Angewandte Mathematik und Mechanik. 2023; 104(2). doi: 10.1002/zamm.202300128
11. Abuasbeh K, Shafqat R, Niazi AUK, et al. Mild Solutions for the Time-Fractional Navier-Stokes Equations with MHD Effects. Symmetry. 2023; 15(2): 280. doi: 10.3390/sym15020280
12. Magyari E, Keller B. Heat and mass transfer in the boundary layers on an exponentially stretching continuous surface. Journal of Physics D: Applied Physics. 1999; 32(5): 577-585. doi: 10.1088/0022-3727/32/5/012
13. Darcy H. Les Fontaines publiques de la ville de Dijon; Exposition et application des principes à suivre et des formules à employer dans les questions de distribution d'eau ... (French). Legare Street Press; 2022.
14. Forchheimer PH. Water movement through soil (German). Available online: https://cir.nii.ac.jp/crid/1572261549273889536 (accessed on 16 March 2024).
15. Wang J, Mustafa Z, Siddique I, et al. Computational Analysis for Bioconvection of Microorganisms in Prandtl Nanofluid Darcy–Forchheimer Flow across an Inclined Sheet. Nanomaterials. 2022; 12(11): 1791. doi: 10.3390/nano12111791
16. Hady FM, Mohamed RA, Mahdy A, et al. Non-Darcy Natural Convection Boundary Layer Flow Over a Vertical Cone in Porous Media Saturated with a Nanofluid Containing Gyrotactic Microorganisms with a Convective Boundary Condition. Journal of Nanofluids. 2016; 5(5): 765-773. doi: 10.1166/jon.2016.1256.
17. Akbar, Y., Alotaibi, H., Iqbal, J., Nisar, K. S., & Alharbi, K. A. M. (2022). Thermodynamic analysis for bioconvection peristaltic transport of nanofluid with gyrotactic motile microorganisms and Arrhenius activation energy. Case Studies in Thermal Engineering, 34, 102055.
18. Iqbal J, Abbasi FM, Nawaz R. Numerical investigation of magnetohydrodynamic bioconvection peristalsis of Powell–Eyring nanofluid. Numerical Heat Transfer, Part A: Applications. Published online March 2024: 1-22. doi: 10.1080/10407782.2024.2322102.

19. Farooq U, Liu T, Farooq U, et al. Non-similar analysis of bioconvection MHD micropolar nanofluid on a stretching sheet with the influences of Soret and Dufour effects. Applied Water Science. 2024; 14(6). doi: 10.1007/s13201-024-02143-0
20. Abbas A, Shafqat R, Jeelani MB, et al. Convective Heat and Mass Transfer in Third-Grade Fluid with Darcy–Forchheimer Relation in the Presence of Thermal-Diffusion and Diffusion-Thermo Effects over an Exponentially Inclined Stretching Sheet Surrounded by a Porous Medium: A CFD Study. Processes. 2022; 10(4): 776. doi: 10.3390/pr10040776
21. Farooq U, Liu T, Farooq U, et al. Heat transfer analysis of ternary hybrid Williamson nanofluids with gyrotactic microorganisms across stretching surfaces: Local non-similarity method. Numerical Heat Transfer, Part A: Applications. Published online April 15, 2024: 1-22. doi: 10.1080/10407782.2024.2341431
22. Saeed Khan MW, Ali N, Bég OA. Thermal entrance problem for blood flow inside an axisymmetric tube: The classical Graetz problem extended for Quemada's bio-rheological fluid with axial conduction. Proceedings of the Institution of Mechanical Engineers, Part H: Journal of Engineering in Medicine. 2022; 236(6): 848-859. doi: 10.1177/09544119221086479
23. Abbas A, Shafqat R, Jeelani MB, et al. Significance of Chemical Reaction and Lorentz Force on Third-Grade Fluid Flow and Heat Transfer with Darcy–Forchheimer Law over an Inclined Exponentially Stretching Sheet Embedded in a Porous Medium. Symmetry. 2022; 14(4): 779. doi: 10.3390/sym14040779
24. Khan MWS, Ali N. Theoretical analysis of thermal entrance problem for blood flow: An extension of classical Graetz problem for Casson fluid model using generalized orthogonality relations. International Communications in Heat and Mass Transfer. 2019; 109: 104314. doi: 10.1016/j.icheatmasstransfer.2019.104314
25. Farooq U, Farooq U. Non-similar analysis of bio-convective micropolar nanofluid flow including gyrotactic microorganisms across a stretched geometry. Numerical Heat Transfer, Part B: Fundamentals. 2024: 1-18. doi: 10.1080/10407790.2024.2333022
26. Khan MWS, Ali N. Thermal entry flow problem for Giesekus fluid inside an axis-symmetric tube through isothermal wall condition: a comparative numerical study between exact and approximate solution. Zeitschrift für Naturforschung A. 2021; 76(11): 973-984. doi: 10.1515/zna-2021-0098
27. Kuznetsov AV. Nanofluid bioconvection in water-based suspensions containing nanoparticles and oxytactic microorganisms: oscillatory instability. Nanoscale Research Letters. 2011; 6(1). doi: 10.1186/1556-276x-6-100
28. Farooq U, Liu T. Non-similar analysis of MHD bioconvective nanofluid flow on a stretching surface with temperature-dependent viscosity. Numerical Heat Transfer, Part A: Applications. 2023; 1-17. doi: 10.1080/10407782.2023.2279249
29. Tiwari RK, Das MK. Heat transfer augmentation in a two-sided lid-driven differentially heated square cavity utilizing nanofluids. International Journal of Heat and Mass Transfer. 2007; 50(9-10): 2002-2018. doi: 10.1016/j.ijheatmasstransfer.2006.09.034
30. Sparrow EM, Yu HS. Local Non-Similarity Thermal Boundary-Layer Solutions. Journal of Heat Transfer. 1971; 93(4): 328-334. doi: 10.1115/1.3449827
31. Rehman MIU, Chen H, Hamid A, et al. Theoretical investigation of Darcy-Forchheimer flow of bioconvection Casson fluid in the presence of chemical reaction effect. Biomass Conversion and Biorefinery. Published online July 27, 2022. doi: 10.1007/s13399-022-03060-5
32. Puneeth V, Anandika R, Manjunatha S, et al. Implementation of modified Buongiorno's model for the investigation of chemically reacting rGO-Fe3O4-TiO2-H2O ternary nanofluid jet flow in the presence of bio-active mixers. Chemical Physics Letters. 2022; 786: 139194. doi: 10.1016/j.cplett.2021.139194
33. Salahuddin T, Khan M, Saeed T, et al. Induced MHD impact on exponentially varying viscosity of Williamson fluid flow with variable conductivity and diffusivity. Case Studies in Thermal Engineering. 2021; 25: 100895. doi: 10.1016/j.csite.2021.100895
34. Devi SU, Devi SA. Heat transfer enhancement of Cu-Al_2O_3/water hybrid nanofluid flow over a stretching sheet. Journal of the Nigerian Mathematical Society. 2017; 36(2): 419-433.
35. Abd El-Aziz M. Viscous dissipation effect on mixed convection flow of a micropolar fluid over an exponentially stretching sheet. Canadian Journal of Physics. 2009; 87(4): 359-368. doi: 10.1139/p09-047
36. Loganathan P, Vimala C. MHD Boundary Layer Flow of a Nanofluid Over an Exponentially Stretching Sheet in the Presence of Radiation. Heat Transfer—Asian Research. 2013; 43(4): 321-331. doi: 10.1002/htj.21077
37. Sharma S. MHD Boundary Layer Flow Past an Exponentially Stretching Sheet with Darcy-Forchheimer Flow of Nanofluids. Indian Journal Of Science And Technology. 2022; 15(33): 1594-1604. doi: 10.17485/ijst/v15i33.607

Thermal Science and Engineering 2024, 7(2), 5943.
https://doi.org/10.24294/tse.v7i2.5943

Article

The effect of co-combustion of cattle manure and sawdust on energy recovered

Samomssa Inna*, Bisso Abazeh, Kamga Richard

Department of Applied Chemistry, National Advanced School of Agro-Industrial Sciences (ENSAI) of the University of Ngaoundere, Ngaoundere 455, Cameroon
*** Corresponding author:** Samomssa Inna, samomssa@yahoo.fr

CITATION

Inna S, Abazeh B, Richard K. The effect of co-combustion of cattle manure and sawdust on energy recovered. Thermal Science and Engineering. 2024; 7(2): 5943. https://doi.org/10.24294/tse.v7i2.5943

ARTICLE INFO

Received: 22 February 2024
Accepted: 2 April 2024
Available online: 10 April 2024

Abstract: The co-hydrothermal carbonization of biomasses has shown many advantages on charcoal yield, carbonization degree, thermal-stability of hydrocar and energy recovered. The goal of this study is to investigate the effect of co-combustion of cattle manure and sawdust on energy recovered. The results show that ash content ranged between 10.38%–20.00%, indicating that the proportion of each variable influences energy recovered. The optimum is obtained at 51% cattle manure and 49% sawdust revealing 37% thermal efficiency and 3.9 kW fire power. These values are higher compared to cattle manure individually which gives values of 30% and 2.3 kW respectively for thermal efficiency and fire power. Thus, the mixture of biomasses enhances energy recovered both in combustion and hydrothermal carbonization. Volatile matter is lower in mixture predicting that the flue gas releases is lower during combustion. Fixed carbon is higher in mixture predicting that energy recovered increases during the combustion of mixture than cattle manure individually. Higher Carbon content was noticed in mixture than cattle manure indicating that the incorporation of sawdust enhances heating value. The incorporation of sawdust in cattle manure can also enhance energy recovered and is more suitable for domestic and industrial application.

Keywords: biomasses; mixture; co-combustion; energy enhancing

1. Introduction

One of the main challenges faced by most developing countries like Cameroon is the lack of clean and affordable fuels for domestic cooking and other industrial activities [1,2]. In these countries, the populations use gas, electricity, wind and solar energies for their various energy activities [3,4]. Furthermore, in the most remote areas of these countries, citizens do not have the means to access these fuels due to their high cost [5]. Thus, they use wood for their energy needs which contributes to fast deforestation [6,7]. Indeed, the use of some of these energies causes environmental problems, mainly the emission of greenhouse gases which is the origin of global warming of the planet [8–11]. These limits lead to find other alternatives energy sources [12,13]. The valorization of biomass is considered as promising route due to its availability and diversity [14–16]. The choice of biomass as energy sources in a given area depends on its availability [17–19]. Thus, in the Adamawa region of Cameroon, cattle breeding predominates peasant life with a herd of around 3.5 million head and produces approximately 1,900,000 dry bons tons of cattle manure per year [20]. The conversion of cattle manure into energy would permit to recycle this waste and clean up the environment as his higher heating value is ranged between 14 MJ/kg and 18 MJ/kg in function of manure origin animal diet and housing system [20–23].

However, the direct use of biomass as energy sources is limited by some

unappropriated properties such as high moisture content, low heating value, high heterogeneity, high alkali content, poor grindability, low bulk density and storage problems [24,25]. Hence, for an efficient use as energy, biomass needs to be converted [20]. Thus, literature reveals many efficient processes of converting biomass to energy biofuels namely physical, thermochemical and biochemical [25]. In physical method of conversion, biomass is densified into solid briquettes while thermochemical process of conversion includes combustion, pyrolysis, gasification and biochemical route consists to convert biomass to ethanol and methane by fermentation and anaerobic digestion [22,25].

Among the methods of converting biomass into energy, the production of fuel briquettes seems to be appropriated for underprivileged populations [25,26]. However, briquettes made from cattle manure often causes problem during combustion due to the high ash content ranging between 22% to 30% in function of housing system. In fact, Kenney et al. [27], Samomssa et al. [20] have shown that biomasses with high ash content more than 10% pose the problem of sintering, agglomeration, deposition, erosion and corrosion caused by the low melting point of ashes. Furthermore, Li et al. [28] indicated that the mixture of biomasses with varied biochemical compositions (cellulose, hemicellulose and protein) enhanced energy recovered during thermochemical conversion. These studies have been investigated on hydrocarbonization process and satisfactory result were obtained on charcoal yield, carbonization degree, thermal-stability of hydrocar and energy recovered. More so, Wang et al. [29], Bardhan et al. [30], Leng et al. [31] justified this result by the fact that the interaction between cellulose, hemicellulose and proteins improves the energy properties during carbonization which occurs in anaerobic conditions and some time at subcritical water conditions under self-generated pressures [32]. The question we ask is the mixture of biomass can also improve energy recovered during combustion which occurs in aerobic conditions? Thus, the sawdust which is abundant in Adamawa region of Cameroon is estimated at 69,000 dry bones tons per year [33] can be combined with cattle manure to probably increase its energy efficiency during combustion. The objective of this study is the valorization of cattle manure and sawdust for the production of energy briquettes. More precisely, it will be: find the best formulation which gives better combustion; carry out a physico-chemical and energetic characterization; produce briquettes and evaluate their properties.

2. Materials and methods

2.1. Sampling

The cattle manure was provided by School of Veterinary Medicine and Sciences of the University of Ngaoundere while, the sawdust was collected from the furniture factory in Ngaoundere city. These samples were taken in bags to the Analytical Chemistry laboratory of ENSAI. The compositional characteristics were reported by Samomssa et al. [20] and Tchouanti et al. [34] and is presented in **Table 1**.

Table 1. Compositional characteristics of cattle manure on dry basis (%) [20,34].

Structural analysis		
Cattle manure [20]		**Ayous sawdust [34]**
Cellulose	32.21 ± 0.02	46.5 ± 3.54
Hemicellulose	15.67 ± 0.06	16.2 ± 1.56
Lignin	18.50 ± 2.12	16.2 ± 1.56
Proximate analysis		
Volatile matter	64.67 ± 2.08	98.10 ± 0.06
Ash	22.31 ± 2.52	1.90 ± 0.06
Fixed carbon	13.02 ± 4.06	10.90 ± 0.38
Ultimate analysis		
Carbon	37.72 ± 1.84	-
Hydrogen	4.69 ± 0.12	-
Oxygen	34.74 ± 0.63	-
Nitrogen	0.80 ± 0.04	-

2.2. Formulation of best mixture

The best mixture from cattle manure and sawdust was found by the mean of simplex centroid mixture design. Variables were the proportions of cattle manure (X_1) and sawdust (X_2) while the response is ash content. The model is expressed using Schefe model and is presented by Equation (1). This equation does not have a constant and can justify the fact that the sum of the proportion of each experiment has to be equal to 1. The experiment with proportions (1/2, 1/2) and (5/2, 6/2) were added to allow better statistical analysis of the results and the construction of more precise iso-response surfaces. This matrix gives the total of seven (7) experiments.

$$Y = b_1X_1 + b_2X_2 + b_1b_2X_1X_2 \quad (1)$$

2.3. Characterization of the best mixture

The characterization of the best mixture from cattle manure and sawdust included Fourier transformation infrared (FTIR), scanning electron microscope **(**SEM), thermogravimetry (TGA), proximate, ultimate and structural analyses.

FTIR:

FTIR analysis was performed on a Perkin Elmer FTIR spectrometer. The samples were placed on an ATR crystal, pressed down and irradiated with a narrow band of IR light (middle part of the spectrum). The signal of the reflected IR light is detected.

Thermogravimetry:

Thermogravimetry analysis was performed on a Q500 thermogravimeter. The raw and pre-treated biomasses were heated at 650 °C, 10 °C/min heating rate in nitrogen atmosphere as described by Samomssa et al. [25]. A thermocouple measured the temperature difference between the sample and the control. In the absence of transformation, the temperature difference between the control and the sample was low and the thermogram was flat. When a transformation takes place in the sample, a peak is recorded whose orientation indicates whether it is an endothermic or exothermic reaction. Approximately 5 mg of sample was used each time. The heating

rate was 10 °C/min and the nitrogen flow rate was 500 mL min^{-1}.

Scanning electron microscope (SEM):

The morphological, micrograph and microstructure were conducted using Scanning Electron Microscope (SEM) Hitachi S4800 based on interaction between electron and sample. The preparation of the samples consists in dispersing a small quantity on a double-sided carbon adhesive glued to an aluminum sample holder.

Elemental dispersive Xray analysis (EDX):

The EDX analyses were studied to obtain elemental composition by the mean of Hitachi S4500. The measuring device is the Hitachi S4500 microscope operating under vacuum and at an acceleration voltage varying from 0.5 to 30 kV and coupled to an EDX thermofisher detector allowing chemical analysis on the samples from the boron element. It is equipped with a field emission cannon which allows very good spatial resolution. This microscope has been used in environmental mode to limit the charge effects due to the accumulation of electrons on poorly conductive surfaces

Structural analysis:

The cellulose content experiment consisted to treat 1 g of mixture with 5 mL of concentrated nitric and boil the whole in a bain-marie thermostated at 95 °C for 1 h. After decantation and subsequent filtration, a new treatment was carried out under the same conditions. The operation was repeated three times on the same sample. At the end of the third boiling, the white paste obtained was washed with ethanol (20 mL) and then dried in an oven at 105 °C. The residue obtained represents the cellulose content.

The lignin content is determined by taking 50 mL of sulfuric acid (72%) and introducing in the beaker which previously contain 1 g (mL) of sample. The mixture was heated for 3 h, and subsequently filtered. The filtrate was dried for 24 h at 105 °C then incinerated at 550 °C for 4 h. The masses after drying and incineration were weighed and noted m_S and m_I respectively. The lignin content was calculated by the Equation (2).

$$\% \text{ Lignine} = \frac{m_S - m_I}{m_1} \times 100 \quad (2)$$

The alkaline extraction method was used to assess hemicellulose content. 1 g (m_1) of sample was mixed with 25 mL of 0.5 M NaOH. And the was boiled for 4 h, filtered and washed with distilled water until total elimination of residual NaOH. The residues obtained were dried at 105 °C to constant mass (m_2, representing hemicellulose).

Proximate analysis:

Moisture content (MC), volatile mater (VM), ash content (AC) were estimated according to ASTM E871-82 (2006) [35], ASTM E872-82 (2006) [36], and ASTMD 1102-84 (2007) [37] respectively.

Moisture content consisted to weight 1 g of sample ($M1$) then dry at 105 °C for 24 h in oven ad weight again ($M2$). The moisture content was given by Equation (3):

$$MC = \left(\frac{M1 - M2}{M1}\right) \times 100 \quad (3)$$

The volatile matter (VM) was carried out by drying 1 g of powder in an oven at 105 °C until constant mass ($M1$). The dried powder was then calcined in a muffle furnace at 550 °C for 30 min in an anaerobic crucible ad weight ($M2$). The volatile matter content was given by Equation (4):

$$VM = ((M1 - M2)/M1) \times 100 \quad (4)$$

The determination of ash content (AC) follows the same process as the volatile matter, with the difference that the dried sample is calcined at 550 °C in the muffle furnace for 4 h in an aerobic crucible and the mass obtained was noted *M*3. The expression for AC is given by Equation (5).

$$AC = (M3/M1) \times 100 \quad (5)$$

Fixed carbon (FC) expressed as a percentage is calculated using Equation (6):

$$FC = 100 - (VM + AC) \quad (6)$$

where: FC (%) the fixed carbon, VM (%) the volatile matter, AC (%) the ash content.

Ultimate analysis and higher heating value modeling:

The carbon (*C*), hydrogen (*H*), total nitrogen (*N*), sulfur (*S*), oxygen (*O*) and higher heating value were calculated according to the models illustrated by Equations (7)–(13). These models have been developed in order to solve the accessibility of the CHNOS analyser and bomb calorimeter. These models were reviewed by Samomssa et al. [20].

$$C = 0.637FC + 0.455MV \quad (7)$$

Mass concentration of hydrogen (*H*)

$$H = 0.052FC + 0.062MV \quad (8)$$

Mass concentration of total nitrogen (*N*):

$$N = 2.10 - 0.020MV \quad (9)$$

Oxygen mass concentration:

$$O = 0.304FC + 0.476MV \quad (10)$$

Sulfur mass concentration (*S*):

$$S = 100 - (H + C + O + N) \quad (11)$$

$$HHV = 3.393 + 0.507[C] - 0.341[H] + 0.067[N] \quad (12)$$

$$HHV = 27.239 - 0.306 \times [AC] - 0.089 \times [VM] \quad (13)$$

2.4. Fuel briquette production and characterization

Fuel briquettes were produced using Hydraulic mechanic press. Preliminary tests and literature review guided to fix some parameters such as briquetting mass, briquetting pressure and raw material moisture content at 10 g, 10 MPa, 12% respectively. Mechanical and combustion properties were assessed to the obtained fuel briquettes by the method described by Samomssa et al. [25].

Degradation rate of briquette (DRB) was determined by the ratio of the burned distance as a function of time. Thermal efficiency and fire power were also determined by the Equations (14) and (15) respectively.

$$\text{Thermal efficiency} = \frac{Vi \times Cp \times \Delta T}{m \times HV} \times 100 \quad (14)$$

where, *Vi* = Initial volume of distilled water (kg), *Cp*: Specific heat of water (kcal/kg), *ΔT*: Rise in temperature of water (°C), *m*: Mass of fuel used to boil water (kg), *HV*: Heating value, kcal/kg.

$$\text{Fire power} = \frac{m \times HV}{60 \times \Delta T} \quad (15)$$

Index resistance impact (IRI) was evaluated by dropping the fuel briquette several times without initial Vitesse until it breaks. Ten drops were set as a standard for all experiments. IRI is expressed by Equation (16).

$$\text{IRI} = \frac{100 \times \text{Nomber of drops}}{\text{Nomber of broken pieces}} \quad (16)$$

3. Results and discussion

3.1. Best mixture

Table 2 presents the experimental design and showing that ash content ranged between 10.38%–20.00%, indicating that the proportion of each variable influences the response. Taking individually, ash content of cattle manure is 20%, then this value decreases until 10.38% when sawdust is incorporated. According to this result, it can be concluded that, the mixture of biomasses with different biochemical composition improves energy recovered both in combustion and in hydrothermal carbonization. The result in hydrothermal carbonization has been demonstrated by Li et al. [28] and Wang et al. [29]. The viability of result obtained in combustion is better explained by the validation condition of the model presented in **Table 3**.

Table 2. Response matrix.

Experiments	Cattle manure proportion (g)	Sawdust proportion (g)	Ash content (%)
1	2.00	0.00	20.00
2	1.50	0.50	12.02
3	1.00	1.00	10.38
4	0.50	1.50	11.03
5	1.75	0.25	15.81
6	1.25	0.75	12.97
7	2.00	0.00	20.00

Table 3. Validation of model using validation index.

Validation index	Values	Validation condition
R^2	0.98	$R^2 \geq 0.90$
AAD	0.07	AADM = 0
Bf	0.99	0.75 *Bf* 1.25
Af_1	0.99	0.75 Af_1 1.25
Af_2	1.02	0.75 Af_2 1.25

The conditions used to validate the model are reviewed by Samomssa et al. [25] that adjusted R^2 closer to 100%, absolute average deviation (AAD) closer to zero, bias and exactitude factors ranged between 0.75 to 1.25. It is evident from **Table 3** that the validation index is in the intervals set, thus the model of ash content in function of proportion of cattle manure and sawdust is valid and it is illustrated by Equation (13) where X_1 and X_2 represent the proportions of cattle manure and sawdust respectively.

This equation reveals that the proportion of cattle manure (X_1) and sawdust (X_2) positively influence ash content. This influence is two time more observed for cattle manure than sawdust. From Equation (17), the interaction of cattle manure (X_1) and sawdust (X_2) decreases ash content. This result can justify the fact that, the mixture of biomasses enhances energy recovered during combustion probably due to interaction

between cellulose, hemicellulose and protein of each biomass as indicated by Li et al. [28] and Wang et al. [29] in the case of hydrothermal carbonization. In fact, Torgrip and Fernandeze [38] reported that heating value increases when ash content decreases. The influence of each proportion is better described by iso curve response presented in **Figure 1**.

$$\text{Ash content} = 18.786X_1 + 10.918X_2 \times 8.125X_1X_2 \quad (17)$$

This figure reveals two plots notably red and blue. The red plot indicates that the proportion of sawdust decreases ash content while the blue plot illustrates that the proportion of cattle manure increases it. The intersection of the two plots shows the lower value of ash content and justified the fact that the mixture of biomasses enhances energy recovered during combustion. The probability is 0.03 which is less than 0.05 attesting to the viability of the model. The optimum is indicated by the intersection of the two plots revealing 51% of cattle manure and 49% of sawdust.

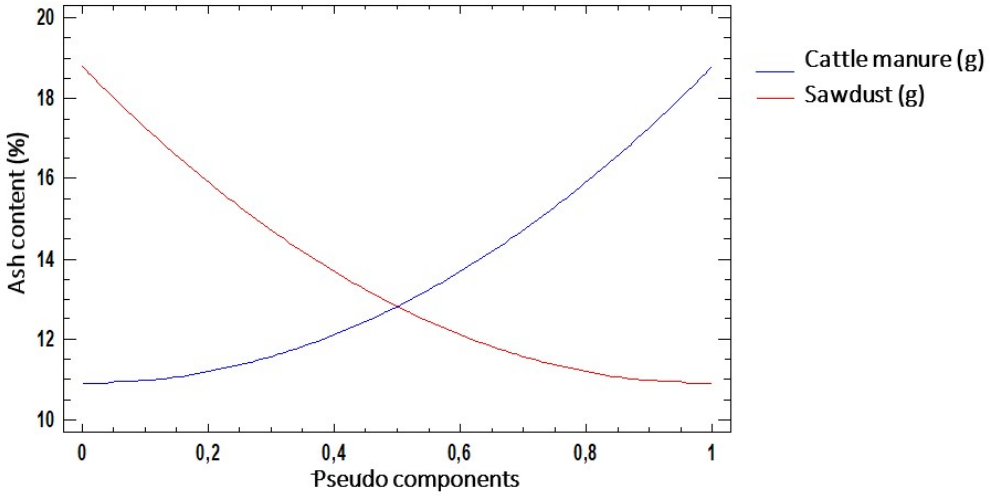

Figure 1. Iso curve response.

3.2. Characterization of the best mixture

Functional groups:

Figure 2 shows infrared spectra illustrating four main adsorption bands, namely between 3100–3500 cm^{-1}; 2000 cm^{-1}; 1500 cm^{-1} and 1000–500 cm^{-1}. The wide absorption band between 3100 cm^{-1} and 3500 cm^{-1} is attributed to the elongation vibration of OH bonded alcohol. This would be due to the presence of cellulose hemicellulose and lignin. The thin absorption band at 2000 cm^{-1} reveals the presence of the C–H elongation bond. The adsorption band at 1500 cm^{-1} is characteristic of elongation of the C–O bond and corresponds to the C–C bond. The absorption band between 1000 cm^{-1} and 500 cm^{-1} are attributed to KCl, $CaCl_2$, phosphate (PO_4^{3-}) and carbonate (CO_3^{2-}) due to the inorganic halogen compounds and mineral components.

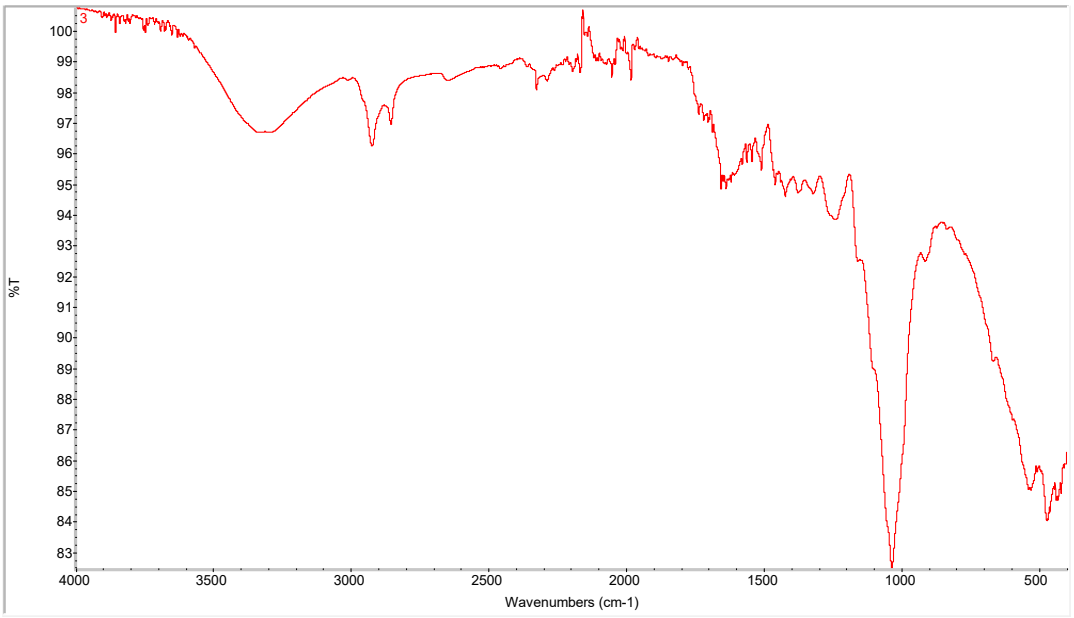

Figure 2. FTIR spectra.

Scanning electron microscope (SEM):

Figure 3 presents the microstructure of the mixture revealing heterogeneous particle size. Ormaechea et al. [39] justified the heterogeneous particle size by the variable proportion of cellulose, hemicellulose and lignin. **Figure 3** also reveals the macro porous structure. Samomssa et al. [25] and Tsai and Liu [40] reviewed that the porous structure is justified by the fact that the space between cellulose is filled by lignin which is distributed across the different layers of the cell wall and reduces the available surface area. Additionally, Tsai and Liu [40] reported that lignocellulosic constituents combined to C and O contain a few amount of mineral elements.

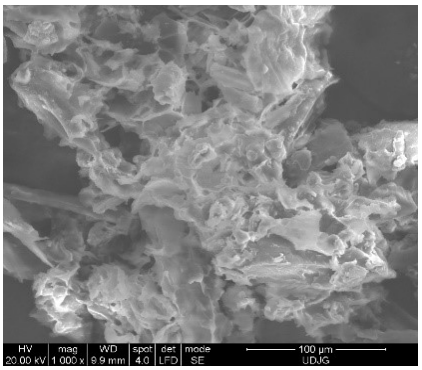

Figure 3. Micrograph of mixture.

It can be concluded that the mixture from cattle manure and sawdust gives macrostructural photography compared to cattle manure which indicated miso porous structure as reported by Ormaechea et al. [39]. Even more, during combustion, oxygen diffuses through the macro pores is more than micropore and can enhance combustion and energy recovered.

EDX:

Figure 4 shows EDX of mixture illustrating that carbon and oxygen are the highest elements followed by nitrogen. This result is in accordance with ultimate

analysis obtained by models and can justified their viability to determine carbon and oxygen. Na, Mg, Al, Rb, Si, Sr, P, S, Cl, K, Ca, Ti, Cr, M, Fe and Ze are trace elements.

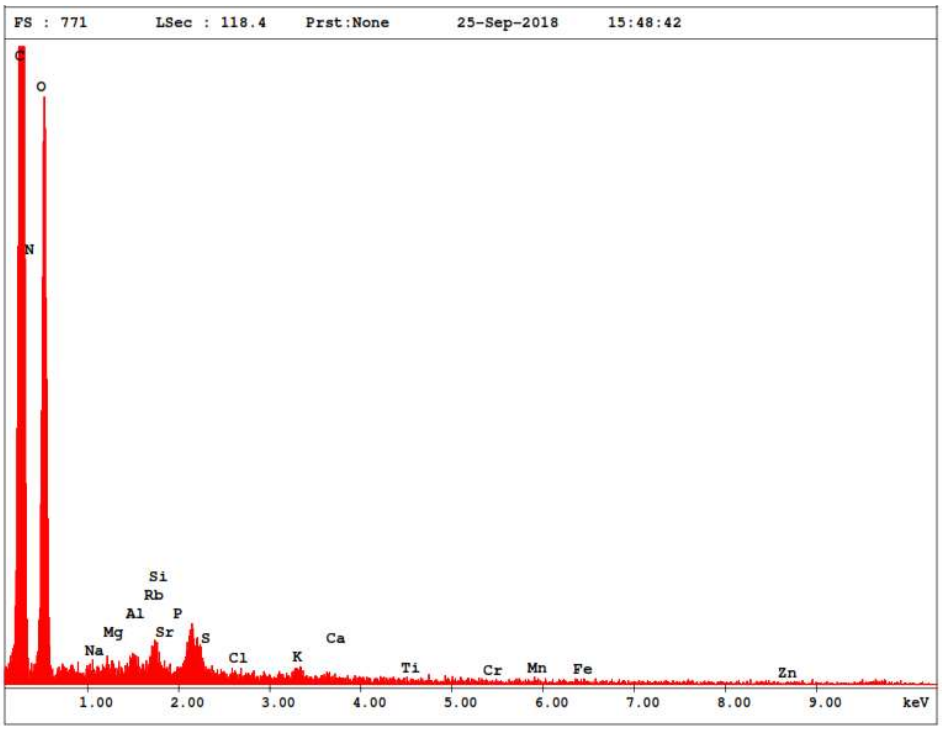

Figure 4. EDX of mixture.

Proximate and ultimate analyses:

Table 4. Proximate and ultimate analyses.

Analyses	Cattle manure	Sawdust	Mixture
Proximate analysis			
Moisture content (MC) %	8.50 ± 0.70	5.75 ± 0.35	6.83 ± 0.62
Ash content (AC) %	21.79 ± 0.81	3.25 ± 0.35	10.38 ± 0.11
Volatile matter (VM) %	64.75 ± 1.40	73.94 ± 0.43	60.67 ± 2.02
Fixed Carbone (FC) %	13.50 ± 0.5	22.81 ± 0.08	28.95 ± 2.10
Ultimate analysis			
Carbon (C) %	31.67	48.16	41.35
Oxygen (O) %	32.12	42.12	38.91
Hydrogen (H) %	4.35	5.76	5.13
Nitrogen (N) %	0.93	0.62	0.73

Table 4 presents proximate and ultimate analyses of cattle manure, sawdust and their mixture. It is appeared from this table that moisture content of the three bio resources is less than 10% and according to Muhammad et al. [41] they can be directly used in combustion without pretreatment. Ash content of cattle manure is higher than mixture while it is lower in sawdust. This is explained by the fact that the incorporation of sawdust in cattle manure decreases ash content thus enhances energy recovered. **Table 4** also shows that volatile matter is lower in mixture predicted that the flue gas

releases is lower during combustion. From **Table 4** fixed carbon is higher in mixture and according to Jiang et al. [42], this result predicted that energy recovered increases during the combustion of mixture than sawdust and cattle manure individually.

In **Table 4**, it is observed that carbon is higher in mixture than cattle manure indicating the fact that the incorporation of sawdust enhances heating value. The same observation hydrogen tends to increase heating value while oxygen and nitrogen decrease heating value. Nitrogen and oxygen predict the quantity of gas emissions during combustion.

Obtained fuel briquettes and characterization:

The picture presented by **Figure 6** illustrated the view of produced fuel briquette and their properties is indicated in **Table 5**. This table presents that, the index resistance impact (IRI) of briquette is 1000 revealing that the obtained fuel briquettes would be handle and transport without breaking. The combustion properties show that the thermal efficiency is 37% and the fire power is 3.9 kW. As presenting in **Table 5**, physico-thermal properties of fuel briquette from cattle manure solely is less than the mixture which indicates that the mixture is better suitable for domestic and industrial application. The degradation rate of fuel mixture briquette is 0.7 cm/min reveals their potential to replace wood energy.

Figure 5. Image of fuel briquette from mixture of cattle manure and sawdust.

Table 5. Fuel briquette properties.

Experiments	Briquette from cattle manure	Briquette from mixture
IRI	1000	500
DRB (cm/min)	0.7	1.0
Thermal efficiency (%)	37.0	30
Fire power (kW)	3.9	2.3

4. Conclusion

The production of energy from biomass has become the points of interest. The main challenge is to put in place the efficient conversion technology and to maximize energy produced. This study presents the effect of cattle manure and sawdust mixture on energy recovered. The result show that ash content ranged between 10.38%–20.00%, indicating that the proportion of each variable influences energy recovered. The optimum is obtained at 51% cattle manure and 49% sawdust for 37% thermal efficiency and 3.9 kW fire power. These values are higher compared to cattle manure individually which gives values of 30% and 2.3 kW respectively for thermal efficiency and fire power. Volatile matter is lower in mixture predicted that the flue gas releases

is lower during combustion. Fixed carbon is higher in mixture predicted that energy recovered increases during the combustion of mixture than cattle manure individually. Carbon is higher in mixture than cattle manure indicating the fact that the incorporation of sawdust enhances heating value.

Author contributions: Conceptualization, SI and KR; methodology, SI and BA; software, BA; validation, SI, KR and BA; formal analysis, SI; investigation, SI; resources, SI; data curation, BA; writing—original draft preparation, SI; writing—review and editing, SI; visualization, KR; supervision, KR; project administration, SI; funding acquisition, SI. All authors have read and agreed to the published version of the manuscript.

Acknowledgments: The authors are thankful to the University of Ngaoundere through laboratory of Materials Sciences and inorganic chemistry for necessary put in our disposal.

Conflict of interest: The authors declare no conflict of interest.

References

1. IEA. Africa energy outlook: A focus on energy prospects in sub-Saharan Africa. World Energy Outlook 2021. International Energy Agency, Paris; 2021. doi: 10.1787/weo-2021-en
2. Ouedraogo NS. Africa energy future: Alternative scenarios and their implications for sustainable development strategies. Energy Policy. 2017; 106: 457-471. doi: 10.1016/j.enpol.2017.03.021
3. Deichmann U, Meisner C, Murray S, Wheeler D. The economics of renewable energy expansion in rural Sub-Saharan Africa. Energy Policy. 2011; 39: 215-227.
4. Brunet C, Savadogo O, Baptiste P, Bouchard MA. Shedding some light on photovoltaic solar energy in Africa—A literature review. Renew Sustain Energy Rev. 2018; 96: 325-342. doi: 10.1016/j.rser.2018.08.004
5. Mohammed YS, Mustafa MW, Bashir N. Status of renewable energy consumption and developmental challenges in Sub-Sahara Africa. Renewable and Sustainable Energy Reviews. 2013; 27: 453-463. doi: 10.1016/j.rser.2013.06.044
6. Samomssa I, Jiokap YN, Kamga R. Energy potential of waste derived from some food crop products in the northern part of Cameroon. Int J Energy Power Eng. 2015; 4: 342-352. doi: 10.11648/j. ijepe.20150406.13
7. IRENA. Africa Power Sector: Planning and Prospects for Renewable Energy. Abu Dhabi/Bonn: IRENA; 2015.
8. Sharma S, Kundu A, Basu S, et al. Sustainable environmental management and related biofuel technologies. Journal of Environmental Management. 2020; 273: 111096. doi: 10.1016/j.jenvman.2020.111096
9. Hoang AT. Experimental study on spray and emission characteristics of a diesel engine fueled with preheated bio-oils and diesel fuel. Energy. 2019; 171: 795-808.
10. Atarod P, Khlaife E, Aghbashlo M, et al. Soft computing-based modeling and emission control/reduction of a diesel engine fueled with carbon nanoparticle-dosed water/diesel emulsion fuel. J. Hazard Mater. 2020; 124369.
11. Cao DN, Hoang AT, Luu HQ, et al. Effects of injection pressure on the NOx and PM emission control of diesel engine: a review under the aspect of PCCI combustion condition. Energy Sources. Part A Recover. Util. Environ. Eff. 2020; 1-18.
12. Stanislav V, Vassilev C, Vassileva G, Vassil SV. Advantages and disadvantages of composition and properties of biomass in comparison with coal: An overview. Fuel. 2015; 158: 330-350. doi: 10.1016/j.fuel.2015.05.050
13. Anh TH, Atabani E, Nizetic S, et al. Acid-based lignocellulosic biomass biorefinery for bioenergy production: Advantages, application constraints, and perspectives. Journal of Environmental Management. 2021; 296: 113194. doi: 10.1016/j.jenvman.2021.113194
14. Jaramillo P, Muller NZ. Air pollution emissions and damages from energy production in the U.S.: 2002–2011. Energy Policy. 2016; 90: 202-211. doi: 10.1016/j.enpol.2015.12.035
15. Hasanbeigi A, Lynn P. A technical review of emerging technologies for energy and water efficiency and pollution reduction in the textile industry. J. Clean. Prod. 2015; 95: 30-44. doi: 10.1016/j.jclepro.2015.02.079

16. Li LL, Lou JL, Tseng ML, et al. A hybrid dynamic economic environmental dispatch model for balancing operating costs and pollutant emissions in renewable energy: A novel improved mayfly algorithm. Expert Systems with Applications. 2022; 203: 117411. doi: 10.1016/j.eswa.2022.117411
17. Chia SR, Ong HC, Chew KW, et al. Sustainable approaches for algae utilisation in bioenergy production. Renewable Energy. 2018; 129: 838-852. doi: 10.1016/j.renene.2017.04.001
18. Mahmood N, Zhaohua W, Nazia Y, et al. How to bend down the environmental Kuznets curve: the significance of biomass energy. Environ. Sci. Pollut. Res. 2019; 26: 21598-21608. doi: 10.1007/s11356-019-05442-1
19. Parthasarathy P, Narayanan SK. Effect of hydrothermal carbonization reaction parameters on. Environ. Prog. Sustain. Energy. 2014; 33(3): 676-680.
20. Samomssa I, Henriette AZ, Boukar H, et al. Compositional characteristics and theoretical energy potential of animal droppings from Adamawa region of Cameroon. Biomass Convers. Biorefin. 2022. doi: 10.1007/s13399-022-03320-4
21. Azevedo A, Franccesca F, Mateus-da S, et al. Life cycle assessment of bioethanol production from cattle manure. J. Clean. Prod. 2017; 162: 1021-1030. doi: 10.1016/j.jclepro.2017.06.141
22. Lee D, Jun HY, Sungyup J, et al. Valorization of animal manure: A case study of bioethanol production from horse manure. Chem. Eng. J. 2021; 403: 126345. doi: 10.1016/j.cej.2020.126343
23. Hafid HS, Rahman NAA, Shah UKM, et al. Feasibility of using kitchen waste as future substrate for bioethanol production: A review. Renewable and Sustainable Energy Reviews. 2017; 74: 671-686. doi: 10.1016/j.rser.2017.02.071
24. Samomssa I, Jiokap YN, Tsamo C, et al. Inluence of physico-chemical parameters on fuel briquettes properties formulated with mixture of biomasses. J Environ Sci Pollut Res. 2019; 5(2): 338-341. doi: 10.30799/jesps.165.19050202
25. Samomssa I, Nono YJ, Cârâc G, et al. Optimization of fuel briquette production from cassava peels, plantain peels and corn cobs. Journal of Material Cycles and Waste Management. 2021; 23(5): 1905-1917. doi: 10.1007/s10163-021-01260-1
26. Leng L, Huang H. An overview of the effect of pyrolysis process parameters on biochar stability. Bioresource Technology. 2018; 270: 627-642. doi: 10.1016/j.biortech.2018.09.030
27. Kenney KL, Smith WA, Gresham GL, et al. Understanding biomass feedstock variability. Biofuels. 2013; 4(1): 111-127. doi: 10.4155/bfs.12.83
28. Li Y, Liu H, Xiao K, et al. Correlations between the physicochemical properties of hydrochar and specific components of waste lettuce: Influence of moisture, carbohydrates, proteins and lipids. Bioresource Technology. 2019; 272: 482-488. doi: 10.1016/j.biortech.2018.10.066
29. Wang T, Si B, Gong Z, et al. Co-hydrothermal carbonization of food waste-woody sawdust blend: Interaction effects on the hydrochar properties and nutrients characteristics. Bioresource Technology. 2020; 316: 123900. doi: 10.1016/j.biortech.2020.123900
30. Bardhan M, Novera TM, Tabassum M, et al. Co-hydrothermal carbonization of different feedstocks to hydrochar as potential energy for the future world: A review. Journal of Cleaner Production. 2021; 298: 126734. doi: 10.1016/j.jclepro.2021.126734
31. Leng L, Yang L, Chen J, et al. A review on pyrolysis of protein-rich biomass: Nitrogen transformation. Bioresource Technology. 2020; 315: 123801. doi: 10.1016/j.biortech.2020.123801
32. Wu Q, Yu S, Hao N, et al. Characterization of products from hydrothermal carbonization of pine. Bioresource Technology. 2017; 244: 78-83. doi: 10.1016/j.biortech.2017.07.138
33. Hassana B, Mbawala A, Ngassoum M, Ibrahima A. Investigation of some biomasses availability for conversion in biochar: Case of Ngaoundere (Cameroonian). Int. J. Sci. Technol. 2019; 6: 597-609.
34. Tchouanti NB, Onguene MP, Ahmed A, Ruben M. Effect of particle size on syngas production using sawdust of Cameroonian Triplochiton scleroxylon. Sci. Afr. 2019; 6: e00182. doi: 10.1016/j.sciaf.2019.e00182
35. ASTM Standards. Standard test method moisture analysis of particulate wood. Fuels. 2006 ; 1871–1882.
36. ASTM Standards. Standard test method for ash in biomass. Fuels. 2007 ; 1755–1761.
37. ASTM Standards. Standard test method for volatile matter in the analysis of particulate wood. Fuels. 2006 872–882.
38. Torgrip RJO, Fernández-Cano V. Rapid X-ray based determination of moisture-, ash content and heating value of three biofuel assortments. Biomass and Bioenergy. 2017; 98: 161-171. doi: 10.1016/j.biombioe.2017.01.005
39. Ormaechea P, Castrillón L, Suárez-Peña B, et al. Enhancement of biogas production from cattle manure pretreated and/or co-digested at pilot-plant scale. Characterization by SEM. Renewable Energy. 2018; 126: 897-904. doi: 10.1016/j.renene.2018.04.022

40. Tsai WT, Liu SC. Thermochemical characterization of cattle manure relevant to its energy conversion and environmental implications. Biomass Conversion and Biorefinery. 2015; 6(1): 71-77. doi: 10.1007/s13399-015-0165-7
41. Muhammad D, Naqvi M, Usman F, Naqvi S. Characterization of South Asian agricultural residues for potential utilization in future energy mix. Energy Procedia. 2015; 75: 2974-2980. doi: 10.1016/j.egypro.2015.07.604
42. Jiang C, Lin Q, Wang C, et al. Experimental study of the ignition and combustion characteristics of cattle manure under diferent environmental conditions. Energy. 2020; 197: 117143. doi: 10.1016/j.energy.2020.177143

Thermal Science and Engineering 2024, 7(2), 8821.
https://doi.org/10.24294/tse.v7i2.8821

Article

Performance and emissions of water-emulsified diesel fuel in an IDI diesel engine under varying engine load

Pedro Oliveira[1,*], Francisco Brójo[2]

[1] Centre for Mechanical and Aerospace Sciences and Technologies (C-MAST), University of Beira Interior, 6200-358 Covilhã, Portugal
[2] Department of Aerospace Sciences, University of Beira Interior, 6200-358 Covilhã, Portugal
*** Corresponding author:** Pedro Oliveira, p.m.penafiel@gmail.com

CITATION

Oliveira P, Brójo F. Performance and emissions of water-emulsified diesel fuel in an IDI diesel engine under varying engine load. Thermal Science and Engineering. 2024; 7(2): 8821. https://doi.org/10.24294/tse.v7i2.8821

ARTICLE INFO

Received: 14 April 2024
Accepted: 3 May 2024
Available online: 12 May 2024

Abstract: This paper aims to verify the possibility of utilising water-in-diesel emulsions (WiDE) as an alternative drop-in fuel for diesel engines. An 8% WiDE was produced to be tested in a four-stroke, indirect injection (IDI) diesel engine and compared to EN590 diesel fuel. An eddy current brake and an exhaust gas analyser were utilised to measure different engine parameters such as torque, fuel consumption, and emissions at different engine loads. The results show that the engine running on emulsified fuel leads to a reduction in torque and power, an increase in the specific fuel consumption, and slightly better thermal efficiency. The highest percentual increment of thermal efficiency for WiDE is obtained at 100% engine load, 5.68% higher compared to diesel. The emissions of nitric oxide (NO) and carbon dioxide (CO_2) are reduced, but carbon monoxide (CO) and hydrocarbons (HC) emissions are increased, compared to traditional diesel fuel. The most substantial decrease in NO and CO_2 levels was achieved at 75% engine load with 33.86% and 25.08% respectively, compared to diesel.

Keywords: water-in-diesel emulsion; IDI diesel engine; performance; emissions; micro-explosion

1. Introduction

For numerous years, governments worldwide have regrettably overlooked pollution and its detrimental impact on the environment, despite its standing as a chief contributor to both health issues and the planet's decline in recent decades. Among the most severe manifestations of pollution is air pollution, a grave concern highlighted by the World Health Organization, attributing over 4.2 million fatalities annually [1]. Fossil fuels are one of the main responsibles for these emissions of pollutants into the air, accounting for over 84.3% of all primary energy sources [2]. The transport sector represents over 15.0% of the fossil fuels emissions, and in Europe, oil represents over 93% of the total energy consumption in the sector, followed by low amounts of biofuels and natural gas [3,4].

Internal combustion engines represent the big share of fossil fuels' consumption, being responsible for the high concentrations of greenhouse gases in the atmosphere [5]. Until now, diesel engines stood out as one of the most efficient and dependable mechanisms for converting energy, boasting superior fuel-to-power conversion efficiency. This inherent efficiency translates into improved fuel economy [6]. Hence, they reign as the predominant category of engines across a diverse spectrum of applications, including power generation, on-road transportation, agriculture, military usage, and marine operations [7]. However, on a less positive note, diesel engines

constitute the primary source of the most concerning exhaust emissions, notably nitrogen oxides [8].

With the upcoming emissions restrictions scheduled for 2025, known in Europe as the European Emission Standards (Euro 7) [9], plentiful technologies have been developed and are available that offer reduced emissions, like alternative and cleaner fuels (electricity, hydrogen, biofuels, natural gas, etc.). All of which have their advantages and disadvantages. WiDE represents a technological advancement and a fuel designed for integration into diesel engines, offering the dual benefits of enhanced combustion efficiency and reduction in exhaust emissions. As a "drop-in" fuel, no modifications to the engine are needed, ensuring its compatibility for immediate utilisation. An emulsion is a dispersion containing two immiscible phases, mixed by mechanical shear and chemical processes and stabilised by surfactants. In an emulsion, droplets of one liquid are dispersed in a continuous flow [10]. WiDE consists of diesel as the continuous phase, water as the dispersed phase, and surfactants. A surfactant is an amphiphilic molecule that has hydrophobic and hydrophilic parts. The primary goal of a surfactant (or surface-active agent) is to lower the interfacial tension between the two surfaces (e.g., diesel and water), reducing the repellent force between the two liquids and diminishing the attraction between the molecules of the same liquid. This results in lower energy required to increase the surface area, leading to a spontaneous dispersion of water droplets and possibly to a thermodynamically stable system. The secondary role is to maintain the stability of the emulsion while reducing the coagulation effect in the water phase [11,12]. Non-ionic surfactants are relatively non-toxic and the main choice for WiDE [13].

The cleaner combustion of emulsified fuels can be attributed to the puffing and micro-explosion phenomena in emulsion droplets. When the emulsion is sprayed into a hot combustion chamber, heat is transferred to the surface of the fuel droplets by convection and radiation. A rapid break-up of the parent droplets due to the different volatility of the fuel and water promotes a secondary atomization that reduces the combustion duration [14], as seen in **Figure 1**.

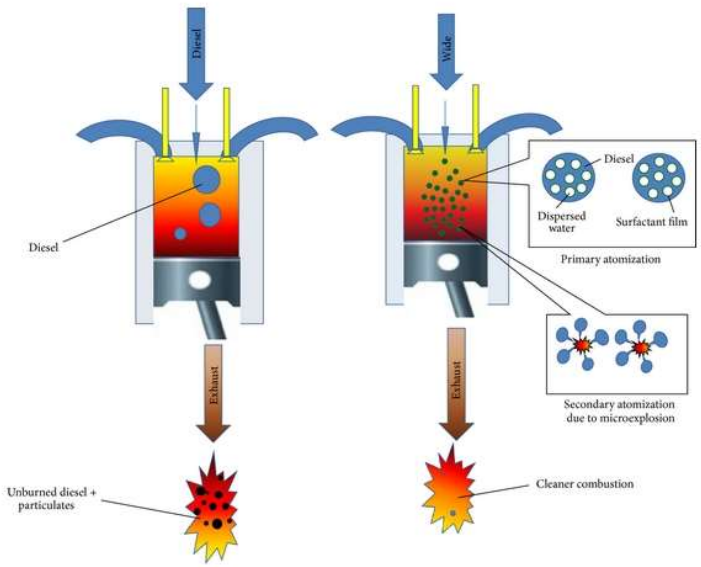

Figure 1. Primary and secondary atomization of WiDE [15].

At this stage, the two phenomena prevail [15,16]. Puffing is the partial ejection of some dispersed water out of an emulsion droplet. Micro-explosion is the complete break-up of the parent droplet. These two occurrences improve the combustion process by enhancing the effective fuel droplet size distribution, leading to better air-fuel mixing and therefore better fuel efficiency and fewer emissions [16]. **Figure 2** shows an example of the micro-explosion phenomenon.

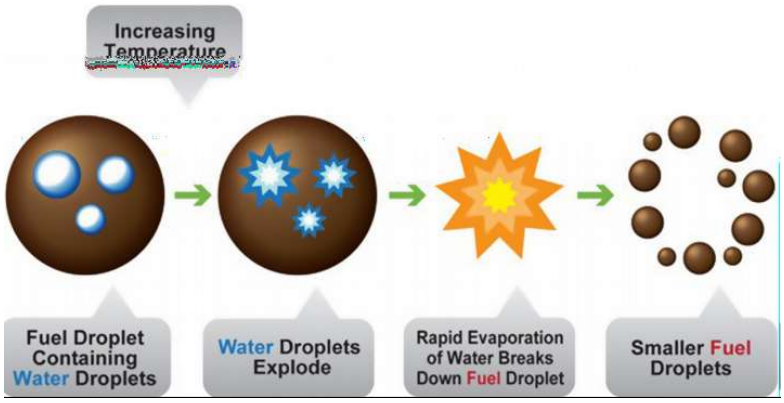

Figure 2. Micro-explosion in WiDE [17].

The evaporation of water present in the emulsion leads to a significant reduction in the combustion chamber temperature (heat sink effect), reducing NOx emissions. The longer ignition delays due to the heat sink effect results in more fuel combustion in premixed mode [14]. The air/fuel ratio becomes higher, ensuring a sufficient amount of oxygen availability, which can help to reduce CO and HC formation [18].

Even though the process is simple to understand, there are still many uncertainties about the ideal properties and composition of the emulsion system [19]. For WiDE, the correct choice of surfactants and the proportional mixture between them is essential to achieve stability and effectiveness. The same happens for the emulsification process and the ideal water content. Different percentages will lead to different results when it comes to performance and emissions parameters. Although most studies are consensus on the reduction of NOx, the results for CO, CO2, and HC differ widely. The same happens for torque, fuel consumption, and thermal efficiency [20–24].

The majority of research concerning performance and emissions pertains to diesel engines featuring direct injection (DI), a more modern technology recognised for its high injection pressures and improved efficiency [25,26]. This prevailing trend is similarly observed in most investigations focused on WiDE [27]. Only a limited number of works regarding emulsions involve engines equipped with indirect fuel injection [28,29]. A most recent study has analysed the effect of DI and IDI on the performance and emissions of WiDE [30]. It has found that even though some of the emissions are reduced, the brake-specific fuel consumption of the IDI case was considerably higher. IDI diesel engines have distinct combustion characteristics, mainly due to the existence of a swirl chamber where combustion begins. The injection pressure is also significantly lower when compared to DI engines. High injection pressures can also be responsible for the reduction in the intensity of micro-explosions due to the evaporation and decrease of dispersed water during the injection spray. By

focusing this study on an IDI diesel engine, which might not experience sufficiently high injection pressures to cause water separation during the spray, more favourable outcomes could potentially be achieved.

Conducting research in this domain can yield a more comprehensive understanding of how emulsions behave across diverse combustion scenarios. It is also possible to find out potential benefits for this engine type that can have broader implications for engine design and performance optimization, especially for industries and operators that rely on existing and older equipment and are unable to transition to newer engine technologies due to the costly replacements.

2. Methodology

2.1. Laboratory testing

In order to achieve the best possible formulation, different trials had to be performed with different percentages (m/m) of water, diesel, and surfactants. The ultimate goal was to produce an emulsion that would be optimised and stable at a temperature close to 40 °C, which is similar to the fuel's tank temperature of the engine during operating conditions. This was verified by pointing a flashlight at one side of the flask and observing if the light would go through the other side. If that is the case, the size of the dispersed water droplets is small enough, and a transparent and stable emulsion was obtained.

EN590 diesel fuel, deionised water, a hydrophilic surfactant, and a lipophilic surfactant were acquired to be used as reagents to produce WiDE. An analytic balance (Radwag AS 310/C/2), a magnetic stirrer (Stuart Scientific SM3), a thermometer (Enviro-Safe), beakers, pipettes, and glass bottles were the materials and equipment used to accurately weigh, measure, and mix the different reagents. **Figure 3** shows the equipment and material used for laboratory testing.

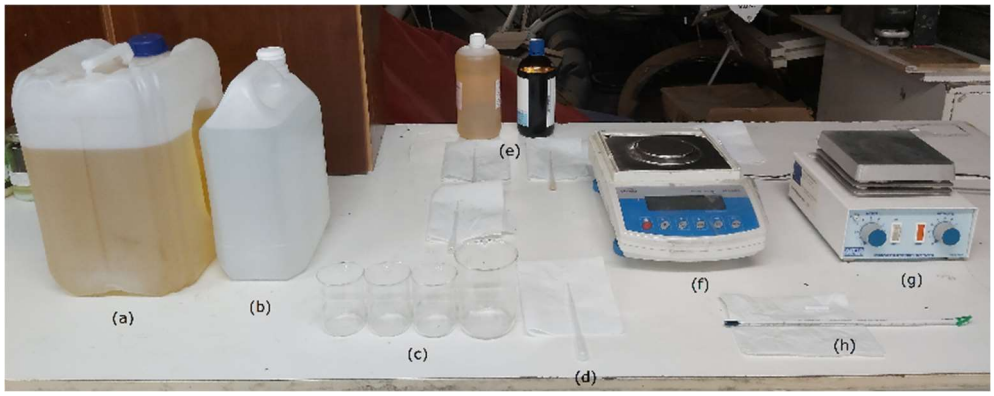

Figure 3. (a) laboratory equipment and material-diesel fuel; **(b)** deionised water; **(c)** beakers; **(d)** pipette; **(e)** surfactants; **(f)** analytic balance; **(g)** magnetic stirrer; and **(h)** thermometer.

The different reagents were weighed and then gradually added to the bottle in the magnetic stirrer in the following order: surfactants-diesel fuel-deionised water. This process was executed at ambient temperature (T = 25 °C). Two surfactants (one hydrophilic and one hydrophobic) were tested at different concentrations (one to

another). Diesel fuel was gradually added to the surfactants and mixed for 5 min. During this period, deionised water was added droplet by droplet. The emulsion was then mixed for 2 more minutes. **Figure 4** shows a common production process of WiDE.

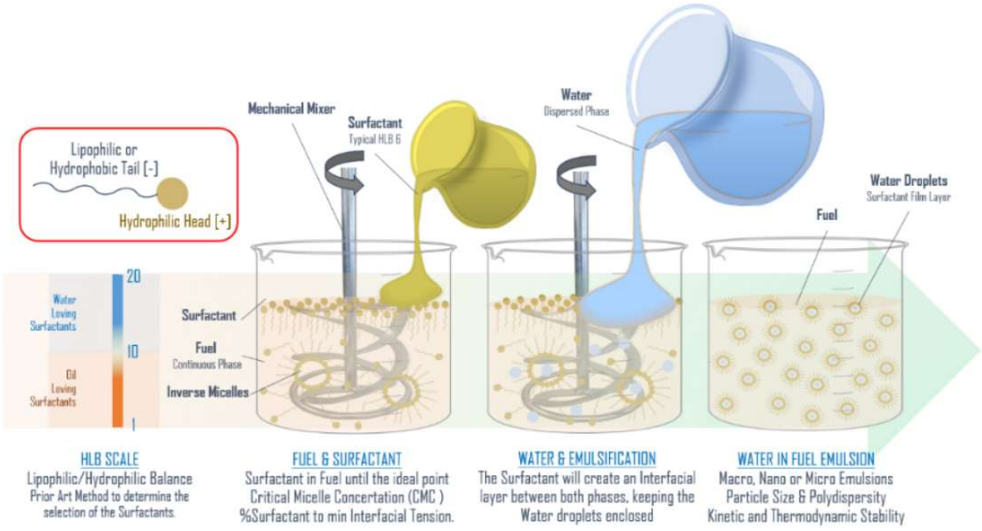

Figure 4. Typical WiDE emulsification process.

For this work, one emulsion was created. It consisted of 89% (m/m) diesel fuel, 8% (m/m) deionised water, and 3% (m/m) surfactant/co-surfactant, as shown in **Figure 5**.

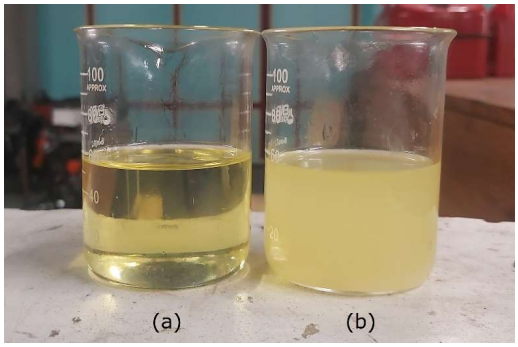

Figure 5. (a) diesel; and **(b)** 8% WiDE at $T = 40$ °C.

This composition of the emulsified fuel was selected based on the work of Fernandes [31], who has a patent on the composition of micro and nanoemulsions, where emulsions with 8% water are included. The only difference was that an alcohol was not utilised as a 3rd reagent and only a surfactant and co-surfactant were utilised. Because the chemical properties of EN590 diesel vary widely, the formulation couldn't be exactly the same. Various combinations of surfactant and co-surfactant percentages were tested, starting at 85% surfactant and 15% co-surfactant with increments of 2% in the hydrophilic surfactant. The goal was to achieve a transparent emulsion at a temperature of 40 °C. After different trials, the formulation that proved most effective for an emulsion containing 8% water content was the one with a 91% hydrophilic surfactant and 9% lipophilic co-surfactant ratio.

2.1.1. Fuel properties

The density, viscosity, and calorific value, among other properties of the fuels, can affect the spray, mixing, and energy release rate during the engine combustion processes. For this reason, different tests were performed in the original fuel and in the emulsions to observe the variation of these properties between them. The density and viscosity of diesel fuel at 60 ℃ were not measured since the temperature of diesel won't exceed 40 ℃ in the fuel tank during engine tests.

Density

The change in density with the increase of temperature for the different fuels was tested and is shown in **Figure 6**.

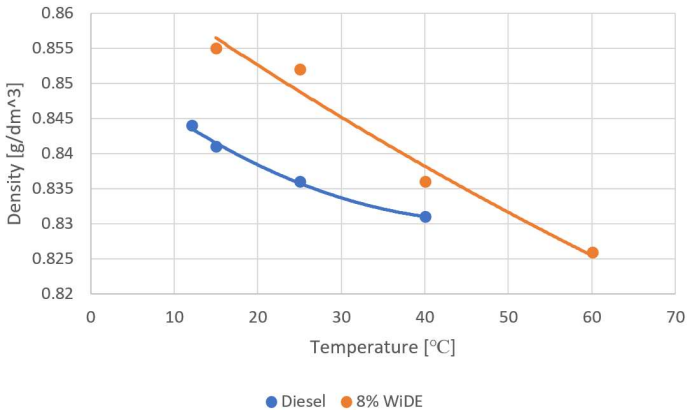

Figure 6. Changes in density with temperature.

Viscosity

The change in the kinematic viscosity with the increase of temperature for the different fuels was tested and is shown in **Figure 7**. The same viscometer was used during all the tests. Ideally, a rheometer should be used for the emulsion (non-Newtonian fluid).

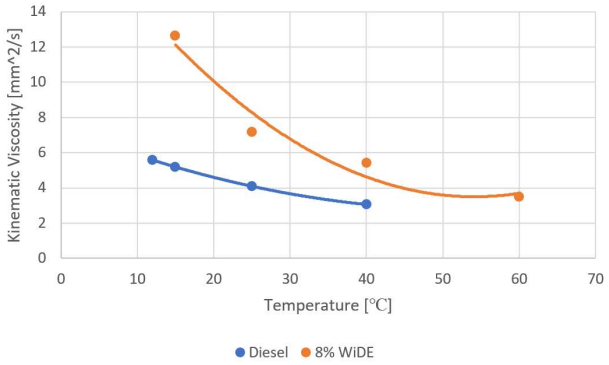

Figure 7. Changes in viscosity with temperature.

As can be seen, a temperature near 60 ℃ will lead to almost similar viscosities between the emulsified fuel and the viscosity of diesel fuel at 40 ℃. Since the mass flow rate of a fuel is heavily correlated with its kinematic viscosity (Poiseuille's law), to achieve similar mass flow rates and similar injection timings, during engine tests the emulsions in the fuel tank were heated to a temperature near 60 ℃ in a thermostatic

bath, while diesel fuel was tested at the temperature reached in the tank during engine operation (~40 °C).

Heating value

The amount of heat released during stoichiometric combustion can be calculated by using a calorimeter. For this case, it was utilised a bomb calorimeter, model 6050 from Parr, as seen in **Figure 8**.

Figure 8. (a) positive electrode; (b) negative electrode; (c) oxygen valve; (d) bomb; (e) water supply; (f) ignition thread; (g) fuel sample; (h) jacket.

After obtaining the higher heating value at constant volume (HHVv) given by the calorimeter, for further calculations, the chemical composition of the different reagents was analysed, as shown in **Table 1**.

Table 1. Chemical composition of the reagents.

	Chemical formula	**Molecular weight [g/mol]**	**Hydrogen [% m/m]**	**Oxygen [% m/m]**
Diesel fuel	$C_{15.18}H_{29.13}$	211.70	13.87	-
Deionised water	H_2O	18.02	11.19	88.81
Hydrophilic surfactant	$CH_3(CH_2)_{10}C(=O)N(CH_2CH_2OH)_2$	299.45	11.11	16.03
Hydrophobic surfactant	$C_{24}H_{44}O_6$	428.61	10.35	22.40

The lower heating value at constant pressure (LHVp), similar to the diesel engine combustion cycle, where water is not condensed and is existing in a vapour form, needs to be calculated. After considering the different weights of the reagents in the fuels and performing the calculations, the different LHVp were obtained. By multiplying the specific energy (MJ/kg) and the fuel's density at 15 °C, we can also obtain the energy density (MJ/L) for each of the fuels, as shown in **Table 2**.

Table 2. Heating values of the fuels.

Fuel	**HHVv (MJ/kg)**	**HHVv (MJ/L]**	**LHVp (MJ/kg)**	**LHVp (MJ/L)**
Diesel	45.49	38.26	42.53	35.77
8% WiDE	41.68	35.64	38.77	33.15

2.2. Engine testing

A Lombardini LDW 502 M3 IDI diesel engine was selected to test the different fuels. Its specifications are shown in **Table 3**. The engine was placed on a test bench

equipped with an eddy current dynamometer. The measured parameters were speed, torque, power, fuel flow, and air flow at different engine loads. An AVL DiTest gas 1000 model 2301 emission gas analyser was used to measure the exhaust gas concentrations. Its specifications are shown in **Table 4**. The test stand is composed of an electromagnetic brake acting as a dynamometer that was dimensioned to dissipate a power of 30 kW at 3000 rpm. It is composed of two coils that produce a magnetic field and a conductive aluminium disk rotating between them. Nunes and Brojo [32] give a detailed explanation of how the dynamometer was designed and the mathematical model utilised. An example of the montage diagram with the equipment, different sensors, and data acquisition devices is shown in **Figure 9**.

Table 3. Engine specifications.

Specifications	LDW 502 M3
Operating cycle	4-stroke
Cylinders	2, in-line
Valves per cylinder	2
Bore [mm]	72
Stroke [mm]	62
Engine displacement [cm^3]	505
Injection system	IDI
Injection pressure [bar]	147
Compression ratio	22.5:1
Maximum torque [Nm]	23
Maximum power [kW]	4

Table 4. Gas analyser specifications.

Gas	Measuring range	Resolution	Accuracy
CO	0–15% vol.	0.01% vol.	±0.03% vol.
CO_2	0–20% vol.	0.01% vol.	±0.5% vol.
HC	0–30,000 ppm vol.	1 ppm vol.	±10 ppm vol.
O_2	0–25% vol.	0.01 % vol.	±5% o.M.
NO	0–5000 ppm vol.	1 ppm vol.	±50 ppm vol.

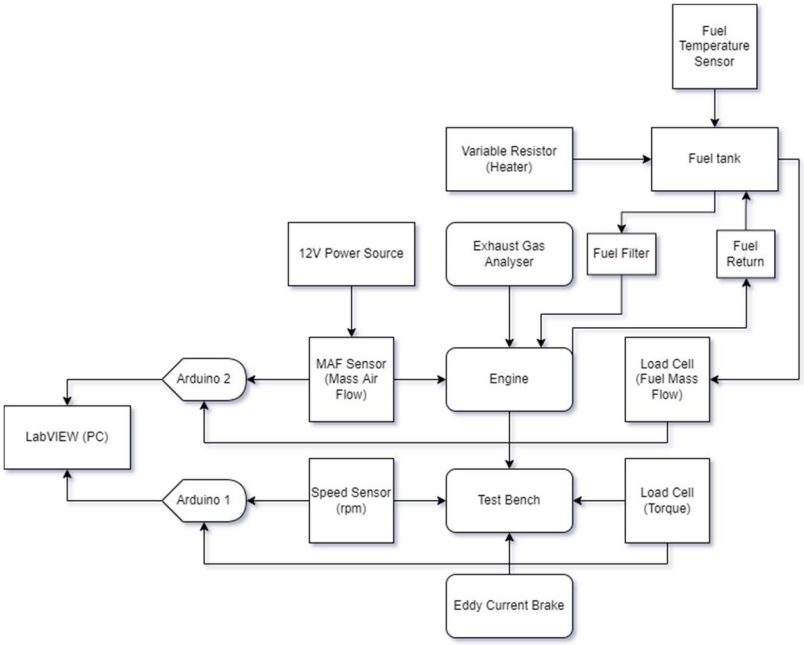

Figure 9. Bench-test montage diagram.

To supply the emulsified fuel to the engine, the previous laboratory emulsion was again reproduced in a sample of 1 kg. A mixing paddle connected to a drill was used as a low-energy mixing method (**Figure 10**).

Figure 10. 8% WiDE mixing at $T = 25$ °C.

As opposed to diesel fuel testing, the flask containing the emulsion was heated in a thermostatic bath and emulsified diesel was supplied to the engine at ~60 °C as shown in **Figure 11**.

Figure 11. Engine bench-test of the emulsion.

Tests were performed for 50%, 75%, and 100% engine loads, defined by the position of the accelerator pedal. For safety purposes, the maximum speed of the engine under no load was limited to around 3000 rpm, leading to a decrease in the maximum torque and power values that the engine could achieve. For each load condition, the engine was left idle for some minutes to warm up, accelerated, and then electromagnetically braked at different speeds until stalling. The tests were performed at ambient temperature ($T = 25$ °C). For each load and speed condition, torque/power, fuel consumption, and emissions results were withdrawn. The LabVIEW interface for data monitoring and acquisition is shown in **Figure 12**.

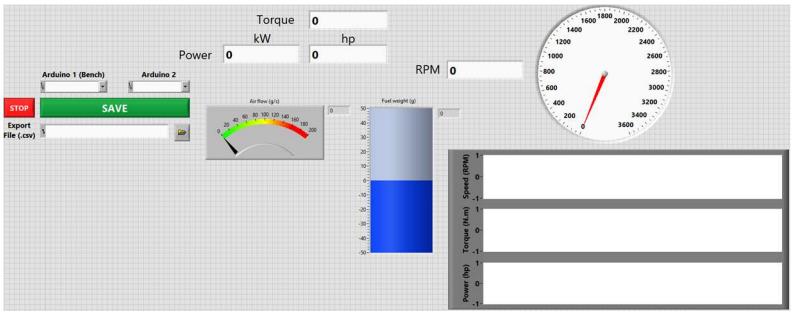

Figure 12. LabVIEW interface.

3. Results and discussion

In this section, the results obtained from the engine performance tests are described. The different parameters in the figures will include the keyword "brake" because an electromagnetic dynamometer (brake) was used to measure them at the engine shaft. This is the usable power or torque delivered by the engine to the load [33].

3.1. Torque and power

As shown in **Figures 13–15**, the overall torque and power values for diesel are higher when compared to WiDE at all engine loads. This can be explained by the higher heating value of diesel fuel which leads to the release of more energy in combustion, surpassing the benefits of the puffing and micro-explosions phenomena happening in WiDE. At full engine load, the peak torque value of the engine for diesel is 18.32 Nm at 976 rpm, and for 8% WiDE, it is 16.79 Nm at 1023 rpm. At this load, the peak power of the engine for diesel is 2.39 kW at 2092 rpm and 2.16 kW at 1621 rpm for 8% WiDE.

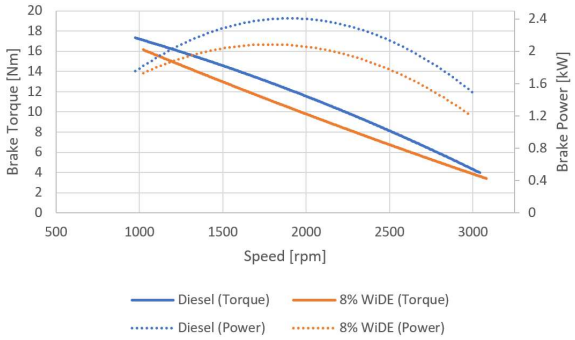

Figure 13. Brake torque and brake power at 100% engine load.

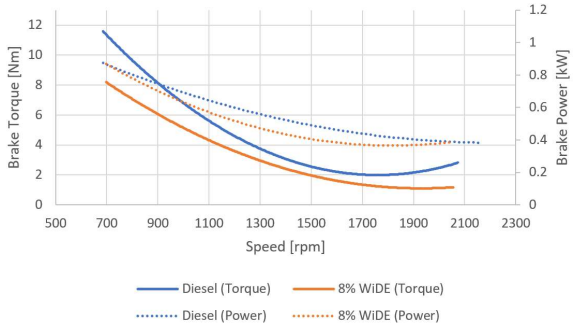

Figure 14. Brake torque and brake power at 75% engine load.

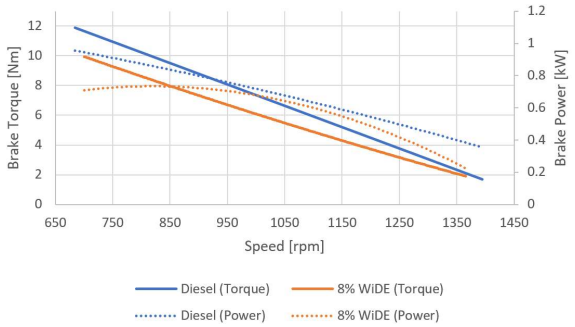

Figure 15. Brake torque and brake power at 50% engine load.

3.2. Fuel consumption and efficiency

Figures 16–18 show that the engine fuelled with diesel has lower overall values of SFC compared to WiDE, which can be explained by the lower energy content of WiDE and slightly higher viscosity (even if heated during tests), leading to a longer injection delay and more fuel injected to overcome the lower LHV of WiDE.

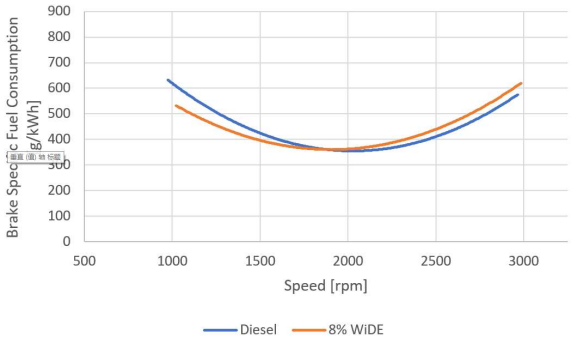

Figure 16. Brake specific fuel consumption at 100% engine load.

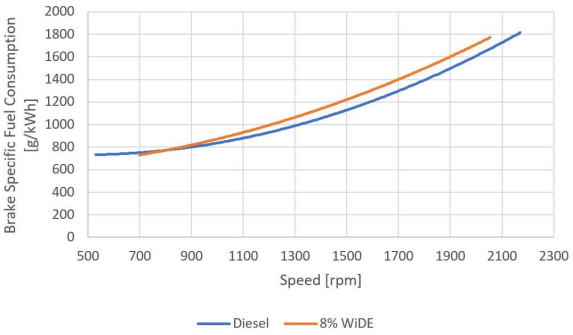

Figure 17. Brake specific fuel consumption at 75% engine load.

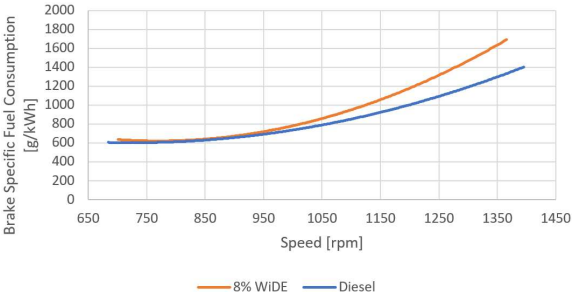

Figure 18. Brake specific fuel consumption at 50% engine load.

Only at 100% engine load, WiDE has similar values of SFC compared to diesel fuel. Even though the power values for diesel were higher, the mass flow rate for WiDE at this condition was low enough to compensate for the loss in power. For other loads (75% and 50%), WiDE has higher SFC values when compared to diesel.

The secondary atomization from the evaporation of water droplets in WiDE can enhance the air/fuel mixing and be responsible for the improved combustion and better fuel efficiency.

As seen before, and because WiDE fuel has less diesel and therefore less energy content in its composition, its LHV will also be lower, improving thermal efficiency as shown in **Figure 19**.

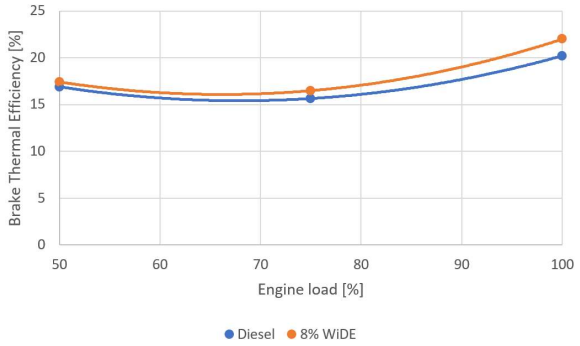

Figure 19. Brake thermal efficiency at different engine loads.

3.3. Emissions

For the different fuels, and at the same conditions where torque, power, and specific fuel consumption curves were obtained, different exhaust gases from the engine were also measured, as shown in **Figures 20–22**. Regarding the hydrocarbon emissions, the gas analyser was calibrated for propane (C_3H_8).

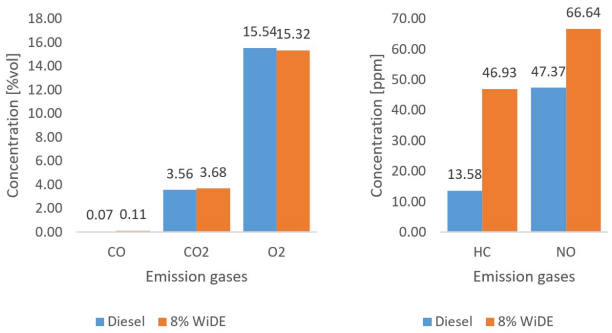

Figure 20. Emission gases at 100% engine load.

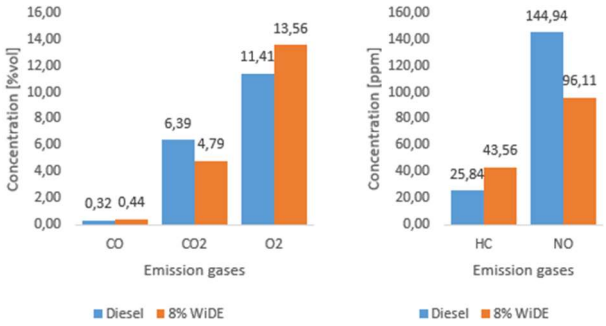

Figure 21. Emission gases at 75% engine load.

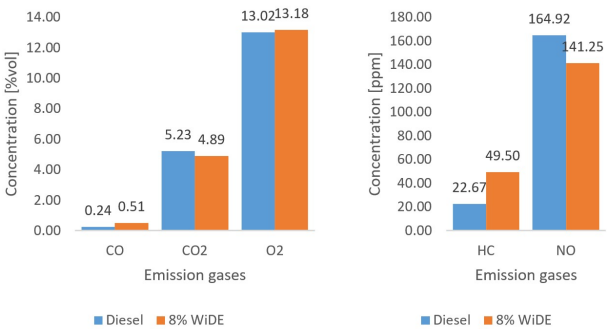

Figure 22. Emission gases at 50% engine load.

As can be seen, at all engine loads, CO and HC emissions of WiDE are higher compared to diesel. The additional carbon and hydrogen atoms of the surfactants used to stabilise the mixture can explain this increase. It is also verified that NO emissions also increase with the decrease in engine load, which was not expected and can be explained by the increase in the combustion temperature at lower accelerator pedal positions, which can be a unique characteristic of the engine and its specific operating conditions.

At 100% engine load, NO emissions of WiDE are higher (due to possibly localised hot spots within the combustion chamber, leading to the dissociation of the water molecules and additional formation of NO). Oxygen (O_2) emissions are similar when compared to diesel. At 75% engine load, NO emissions of WiDE are lower, CO_2 emissions are lower, and O_2 emissions are higher when compared to diesel. At 50% engine load, NO emissions of WiDE are lower, CO_2 emissions are lower, and O_2 emissions are similar when compared to diesel.

The addition of water helps in diminishing the high combustion temperatures responsible for the emissions of NO, the lower carbon content of WiDE helps to reduce the CO_2 emissions, and the higher oxygen content helps to increase the O_2 emissions, even though only verified at 75% engine load.

4. Conclusions

This investigation has concluded that WiDE can have an important role in the future as an alternative drop-in fuel for diesel engines since it is able to improve the thermal efficiency of the engine while simultaneously reducing some of the pollutant emissions.

When compared to diesel fuel, the density and viscosity of the emulsion are higher due to the higher density and viscosity of the surfactants in the mixture. The LHV is lower (approximately 91.6% of pure diesel) due to the lower diesel content in the emulsion, leading to decreased torque and power values, increased specific fuel consumption, and slightly higher thermal efficiency. The overall emissions of NO and CO_2 were lower, but the emissions of CO and HC were higher. The emissions of O_2 were similar. The existence of water as a dispersed phase in the fuel promotes a secondary atomization, enhancing the efficiency of the air/fuel mixing and diminishing the higher combustion temperatures (responsible for the formation of NO), and the lower carbon content can explain the reduced CO_2 emissions. The higher CO and HC emissions can be due to the additional carbon and hydrogen atoms of the surfactants.

These aspects lead to the conclusion that WiDE can improve the combustion process in the engine while reducing some of the hazardous emissions of diesel engines, even though compensated by a slight reduction in torque and power.

Author contributions: Conceptualization, PO and FB; methodology, PO and FB; software, PO; validation, PO and PB; formal analysis, PO and FB; investigation, PO and FB; resources, PO and FB; data curation, PO and FB; writing—original draft preparation, PO and FB; writing—review and editing, PO and FB; visualization, PO

and FB; funding acquisition, PO and FB. All authors have read and agreed to the published version of this manuscript.

Acknowledgments: We would like to thank Santander Totta-UBI (Universidade da Beira Interior) and FCT (Faculdade de Ciências e Tecnologia) 2021.07535.BD for funding this investigation. We would also like to thank C-MAST (Center for Mechanical and Aerospace Technology) UIDB/00151/2020 and University of Castilla-La Mancha, department of Fuels and Engines for providing the space, materials, and equipment needed to develop this research project. Finally, a special thanks to Alexandre Nunes for developing the major portion of the LabVIEW code for data acquisition with the eddy current dynamometer.

Conflict of interest: The authors declare no conflict of interest.

References

1. World Health Organization. Personal interventions and risk communication on air pollution. Available online: https://www.who.int/publications/i/item/9789240000278 (accessed on 18 April 2024).
2. Statistical Review of World Energy. Available online: https://www.bp.com/en/global/corporate/energy-economics/statistical-review-of-world-energy.html#tab_sr-2020 (accessed on 18 April 2024).
3. Bioenergy International. EU transportation sector still overly dependant on fossil fuels. Available online: https://bioenergyinternational.com/markets-finance/eu-transport-still-overly-dependant-on-fossil-fuels (accessed on 18 April 2024).
4. Center for Climate and Energy Solutions. Global emissions. Available online: https://www.c2es.org/content/international-emissions/ (accessed on 18 April 2024).
5. Ağbulut Ü, Sarıdemir S. A general view to converting fossil fuels to cleaner energy source by adding nanoparticles. International Journal of Ambient Energy. 2021; 42(13): 1569-1574. doi: 10.1080/01430750.2018.1563822
6. Mustayen AGMB, Rasul MG, Wange X, et al. Remote areas and islands power generation: A review on diesel engine performance and emission improvement techniques. Energy Conversion and Management. 2022; 260: 115614. doi: 10.1016/j.enconman.2022.115614
7. Kumar MV, Babu AV, Reddy CR, et al. Investigation of the combustion of exhaust gas recirculation in diesel engines with a particulate filter and selective catalytic reactor technologies for environmental gas reduction. Case Studies in Thermal Engineering. 2022; 40(8): 102557. doi: 10.1016/j.csite.2022.102557
8. Tamam MQM, Yahya WJ, Ithnin AM, et al. Performance and emission studies of a common rail turbocharged diesel electric generator fueled with emulsifier free water/diesel emulsion. Energy. 2023; 268: 126704. doi: 10.1016/j.energy.2023.126704
9. ACEA. Position paper—Views on proposals for Euro 7 emission standard. Available online: https://www.acea.auto/publication/position-paper-views-on-proposals-for-potential-euro-7-emission-standard/ (accessed on 18 April 2024).
10. Che Marzuki NH, Wahab RA, Hamid MA. An overview of nanoemulsion: Concepts of development and cosmeceutical applications. Biotechnology & Biotechnological Equipment. 2019; 33(1): 779-797. doi: 10.1080/13102818.2019.1620124
11. Eastoe J. Microemulsions. Available online: https://www.chm.bris.ac.uk/eastoe/Surf_Chem/Surfactant.htm (accessed on 18 April 2024).
12. Kapadia H, Brahmbhatt H, Dabhi Y, Chourasia S. Investigation of emulsion and effect on emission in CI engine by using diesel and bio-diesel fuel: A review. Egyptian Journal of Petroleum. 2019; 28(4): 323-337. doi: 10.1016/j.ejpe.2019.06.004
13. Tadros T. Applied Surfactants: Principles and Applications. Wiley-VCH; 2005. pp. 1-22.
14. Mondal PK, Mandal BK. A comparative study on the performance and emissions from a CI engine fuelled with water emulsified diesel prepared by mechanical homogenization and ultrasonic dispersion method. Energy Reports. 2019; 5: 639-648. doi: 10.1016/j.egyr.2019.05.006
15. Khan MY, Karim ZAA, Hagos FY, et al. Current trends in water-in-diesel emulsion as a fuel. The Scientific World Journal. 2014; 2014: 1-15. doi: 10.1155/2014/527472
16. Sazhin SS, Rybdylova O, Crua C, et al. A simple model for puffing/micro-explosions in water-fuel emulsion droplets.

International Journal of Heat and Mass Transfer. 2019; 131: 815-821. doi: 10.1016/j.ijheatmasstransfer.2018.11.065
17. Park S, Woo S, Kim H, Lee K. The characteristic of spray using diesel water emulsified fuel in a diesel engine. Applied Energy. 2016; 176: 209-220. doi: 10.1016/j.apenergy.2016.05.069
18. Jhalani A, Sharma D, Soni SL, et al. A comprehensive review on water-emulsified diesel fuel: chemistry, engine performance and exhaust emissions. Environmental Science and Pollution Research. 2019; 26(5): 4570-4587. doi: 10.1007/s11356-018-3958-y
19. Abbott S. Surfactant Science: Principles and Practice. Destech Pubns Inc; 2017. p.13.
20. Khathri AM, Ismail MY, Abdullah AA, et al. Performance, exhaust emissions and optimization using response surface methodology of a water in diesel emulsion on diesel engine. Journal of Advanced Research in Fluid Mechanics and Thermal Sciences. 2022; 93(1): 1-12. doi: 10.37934/arfmts.93.1.112
21. Ramalingam K, Venkatesan EP, Aabid A, Baig M. Assessment of CI engine performance and exhaust air quality outfitted with real-time emulsion fuel injection system. Sustainability. 2022; 14(9): 5313. doi: 10.3390/su14095313
22. Gautam PS, Vishnoi PK, Gupta VK. The effect of water emulsified diesel on combustion, performance and emission characteristics of diesel engine. Materialstoday: Proceedings. 2022; 52: 1041-1047. doi: 10.1016/j.matpr.2021.10.485
23. Gowrishankar S, Krishnasamy A. Emulsification—A promising approach to improve performance and reduce exhaust emissions of a biodiesel fuelled light-duty diesel engine. Energy. 2023; 263: 125782. doi: 10.1016/j.energy.2022.125782
24. Okumuş F, Kaya C, Kökkülünk G. NO_x based comparative analysis of a CI engine fueled with water in diesel emulsion. Energy Sources, Part A: Recovery, Utilization, and Environmental Effects. 2023; 45(3): 6710-6729. doi: 10.1080/15567036.2020.1839147
25. Gül MZ, Köten H, Yılmaz M, Savci IH. Advanced numerical and experimental studies on CI engine emissions. Journal of Thermal Engineering. 2018; 4(8): 2234-2247. doi: 10.18186/journal-of-thermal-engineering.434044
26. Köten H. Investigation of diesel engine performance and emissions by multi-dimensional modelling. International Journal of Automotive Engineering and Technologies. 2018; 7(2): 76-87. doi: 10.18245/ijaet.458898
27. El-Adawy M, Ismael MA, Dalha IB, et al. Unveiling the status of emulsified water-in-diesel and nanoparticles on diesel engine attributes. Case Studies in Thermal Engineering. 2023; 44: 102824. doi: 10.1016/j.csite.2023.102824
28. Armas O, Ballesteros R, Martos FJ, Agudelo JR. Characterization of light duty diesel engine pollutant emissions using water-emulsified fuel. Fuel. 2005; 84(7-8): 1011-1018. doi: 10.1016/j.fuel.2004.11.015
29. Selim MYE, Ghannam MT. Combustion study of stabilised water-in-diesel fuel emulsion. Energy Sources, Part A: Recovery, Utilization, and Environmental Effects. 2009; 32(3): 256-274. doi: 10.1080/15567030802467621
30. Oo YM, Thawornprasert J, Intaprom N, Somnuk K. Diesel-biodiesel-water fuel nanoemulsions for direct injection and indirect injection diesel engines: Performance and emissions characteristics. ACS Omega. 2022; 7(39): 34951-34965. doi: 10.1021/acsomega.2c03553
31. Fernandes SJC. Method, System, Apparatus and Formulations for Producing Oil-based Blends and Microemulsions and Nanoemulsions. U.S. Patent EP4055127A1, 14 September 2022.
32. Nunes AJR, Brojo FMRP. Designing an eddy current brake for engine testing. Knowledge Engineering. 2020; 5(6): 743-756. doi: 10.18502/keg.v5i6.7094
33. Heywood JB. Internal Combustion Engine Fundamentals, 1st ed. New York: McGraw-Hill Education; 1988. p. 46.

Thermal Science and Engineering 2024, 7(2), 8050.
https://doi.org/10.24294/tse.v7i2.8050

Article

Modified Cattaneo-Vernotte equation for heat transfer in solids

Victor L. Mironov

Institute for Physics of Microstructures, Russian Academy of Sciences, GSP-105, Nizhny Novgorod 603950, Russia; mironov@ipmras.ru

CITATION

Mironov VL. Modified Cattaneo-Vernotte equation for heat transfer in solids. Thermal Science and Engineering. 2024; 7(2): 8050. https://doi.org/10.24294/tse.v7i2.8050

ARTICLE INFO

Received: 18 April 2024
Accepted: 30 May 2024
Available online: 15 June 2024

Abstract: We propose a modified relation between heat flux and temperature gradient, which leads to a second-order equation describing the evolution of temperature in solids with finite rate of propagation. A comparison of the temperature field spreading in the framework of Fourier, Cattaneo-Vernotte (CV), and modified Cattaneo-Vernotte (MCV) equations is discussed. The comparative analysis of MCV and Fourier solutions is carried out on the example of a simple one-dimensional problem of plate cooling.

Keywords: Non-Fourier thermal conductivity; modified Cattaneo-Vernotte equation; microscale heat transfer

1. Introduction

In classical consideration, the process of heat transfer in solids is described by a phenomenological equation based on two assumptions [1]. The first is the continuity of heat propagation:

$$c\rho\frac{\partial\theta}{\partial t}+\nabla\cdot\mathbf{q}=0 \tag{1}$$

where c is the specific heat capacity, ρ is the mass density, θ is the temperature, q is the vector of heat flux. The second assumption is Fourier's law, which establishes the relationship between heat flux and gradient of temperature

$$\mathbf{q}=-\kappa\nabla\theta \tag{2}$$

where κ is the thermal conductivity. Substitution (2) into Equation (1) gives the classical equation for the temperature evolution

$$\frac{\partial\theta}{\partial t}-\beta_q\Delta\theta=0 \tag{3}$$

where $\beta_q=\kappa/c\rho$ is the thermal diffusivity, Δ is the Laplace operator.

The disadvantage of relation (2) is that it leads us to the equation of parabolic type (3), which describes the instantaneous propagation of heat [2–4]. However, this contradicts the physical nature of the heat transfer process.

To overcome the drawback in classical heat conduction, the different modifications of Fourier's law were proposed [3,4]. Among them, we can highlight "inertial" theories [4,5], nonlinear models [6,7], the dual-phase-lag approach [8], and more complicated models based on Oldroyd's upper-convected derivative [9,10] (which are used for the description of non-Fourier heat transfer in fluids [11–13]). Some historical considerations on the various hyperbolic heat equations can be found in [3,4,14,15].

In particular, the simple Fourier's law modification taking into account "inertia" of the heat transfer is formulated as follows [3–6]:

$$\tau_q \frac{\partial \mathbf{q}}{\partial t} + \mathbf{q} = -\kappa \nabla \theta \tag{4}$$

where τ_q is a relaxation time depending on material properties. When $\tau_q = 0$ the expression (4) is transformed to the Fourier's law (2). The relation (4) in combination with continuity condition (1) leads us to the wave equation of hyperbolic type

$$\tau_q \frac{\partial^2 \theta}{\partial t^2} + \frac{\partial \theta}{\partial t} - \beta_q \Delta\theta = 0 \tag{5}$$

which is widely discussed as Cattaneo-Vernotte (CV) equation [16–31].

Note that in the limiting case $\tau_q \to \infty$, $\kappa \to \infty$, β_q finite the equation (5) turns into a wave equation

$$\frac{\partial^2 \theta}{\partial t^2} - a^2 \Delta\theta = 0 \tag{6}$$

describing purely wave propagation of heat at a constant speed

$$a = \sqrt{\frac{\kappa}{c\rho\tau_q}} \tag{7}$$

The parabolic Fourier equation (3) and hyperbolic CV equation (5) describe the same stationary states, which are determined by the Laplace operator, but the dynamics of relaxation to these stationary states is different. However, eliminating the paradox of instantaneous heat propagation [4,20,21], the CV heat equation leads to other paradoxical results associated with interference of temperature waves, their reflection from the boundaries of the body, and the formation of shock heat waves [22–31]. Therefore, discussions about the applicability of the Fourier and CV equations continue [32,33].

Note also that the processes of diffusion and heat transfer have a similar nature [1,34], 34]. Therefore, the telegraph equations of hyperbolic type for diffusion are also discussed in the literature [35,36].

In this paper, we propose a modification of the CV approach to the description of heat transfer, which leads to the alternative equation and describes a different dynamics of heat transfer.

2. Comparison of Fourier equation and Cattaneo-Vernotte equation

Let us compare Fourier and CV equations in detail. The Equation (4) introduces a very important parameter τ_q that describes the time scale of heat relaxation and allows one to determine the characteristic rate of heat propagation as

$$s_q^2 = \frac{\beta_q}{\tau_q} \tag{8}$$

and the characteristic spatial scale of heat diffusion as

$$l_q = \sqrt{\beta_q \tau_q} = s_q \tau_q \tag{9}$$

This allows one to rewrite Fourier and CV equations in the similar form

$$\frac{1}{\tau_q}\frac{\partial\theta}{\partial t}-s_q^2\Delta\theta=0 \tag{10}$$

$$\frac{\partial^2\theta}{\partial t^2}+\frac{1}{\tau_q}\frac{\partial\theta}{\partial t}-s_q^2\Delta\theta=0 \tag{11}$$

The Equations (10) and (11) admit the solutions in the form of plane waves

$$\theta=A\exp\left(i\omega t+i\left(\boldsymbol{k}\cdot\boldsymbol{r}\right)\right) \tag{12}$$

where ω is the frequency, $k$is the wave vector. The dispersion relation for parabolic Fourier Equation (10) is

$$\omega=i\tau_q s_q^2 k^2 \tag{13}$$

where k is the wave number ($k=|\boldsymbol{k}|$). In this relation, the frequency is an imaginary quantity. Thus, the solutions of the Fourier equation are spatial harmonics decaying with time. The damping factor is

$$i\omega=-\tau_q s_q^2 k^2 \tag{14}$$

The dependence of the decrement (14) on the wave number is shown in **Figure 1**.

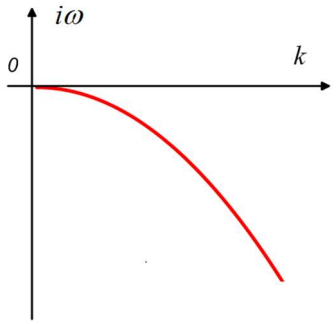

Figure 1. The schematic plot of dispersion dependence for parabolic Fourier equation.

Also, we can introduce the analog of group speed, which is the imaginary value

$$iv_F=i\frac{d\omega}{dk}=-2\tau_q s_q^2 k. \tag{15}$$

This value tends to infinity ($iv_F\to-\infty$) when $k\to\infty$, that is the reason of the infinitely fast scattering of shortwave harmonics.

On the other hand, the dispersion relation for hyperbolic CV Equation (11) is

$$\omega^2+\frac{i\omega}{\tau_q}-s_q^2k^2=0 \tag{16}$$

From (16) we obtain

$$\omega=i\,\frac{1\pm\sqrt{1-4l_q^2k^2}}{2\tau_q} \tag{17}$$

The behavior of spatial harmonics essentially depends on their wave number. In the region of wave numbers $k<k^*$ (where $k^*=\frac{1}{2l_q}$), solutions of CV equation also represent damped spatial harmonics. The damping factor is

$$i\omega = -\frac{1 \pm \sqrt{1 - 4l_q^2 k^2}}{2\tau_q} \tag{18}$$

Dispersion dependence (18) is shown in **Figure 2**.

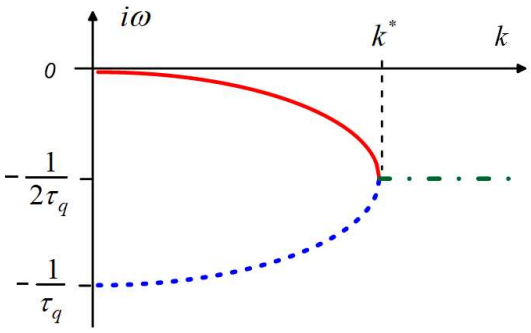

Figure 2. The schematic plot of decrement for hyperbolic CV equation. The solid curve corresponds to the "–" sign in expression (18), the dotted curve corresponds to the "+" sign. The dash-dotted line in the region $k > k^*$ represents the decrement in expression (19).

In the region $k < k^*$, the decrement has two branches (shown by solid and dotted lines in **Figure 2**) in accordance with the signs in expression (18). At small k on the upper branch of the dispersion curve, the decrement is $i\omega \approx -\tau_q s_q^2 k^2$, that coincides with the decrement of the Fourier Equation (14).

In the region $k > k^*$, the dispersion dependence (18) has both imaginary and real parts

$$\omega = i\,\frac{1}{2\tau_q} \pm \frac{\sqrt{4l_q^2 k^2 - 1}}{2\tau_q}. \tag{19}$$

The damping factor in this region of wave numbers is equal to

$$i\omega = -\frac{1}{2\tau_q} \tag{20}$$

It is shown by the dot-dashed line in **Figure 2**. The real part of the dispersion relation (19) is shown in **Figure 3**.

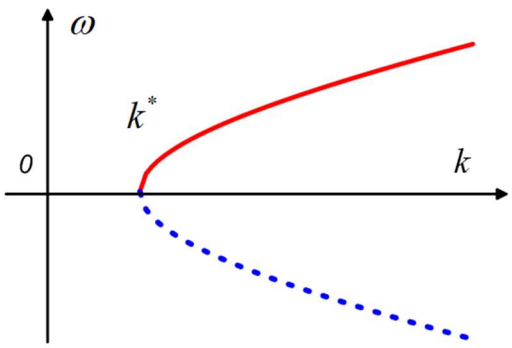

Figure 3. The schematic plot of the real part of dispersion curves for CV equation.

The region of wave numbers $k > k^*$ corresponds to the spatial harmonics propagating in the form of traveling waves. In this region CV equation has the real group velocity.

$$v_{CV} = \frac{d\omega}{dk} = \frac{2l_q^2}{\tau_q} \frac{k}{\sqrt{4l_q^2k^2 - 1}} \tag{21}$$

This value tends to be constant s_q ($v_{CV} \to s_q$) when $k \to \infty$. However, the group velocity of harmonics with k near k^* still tends to an infinite value. A more extended spectral analysis of the CV equation can be found in [37].

3. Modified Cattaneo-Vernotte equation of heat transfer

Evidently, the hyperbolic heat equation is a consequence of the concept of "inertia" for heat flow. However, this concept raises doubts since the macroscopic transfer of heat is associated not with their directed motion but with chaotic vibrations of atoms in the crystal lattice. Here we propose the modification of CV condition (4) that leads to an alternative equation describing different dynamics of heat propagation.

Let us first analyze the CV modification of Fourier's law. It assumes the lagging response in time between the heat flux vector and the temperature gradient. Mathematically, this can be expressed as:

$$\mathbf{q}(\boldsymbol{r}, t + \tau_q) = -\kappa \nabla \theta(\boldsymbol{r}, t) \tag{22}$$

where τ_q is the phase-lag in time. Expression (22) shows that the temperature gradient established at time t is defined by heat flux vector at a later time $t + \tau_q$. Assuming the smallness of the parameter τ_q, we can expand the left side of equation (22) into a Taylor series:

$$\mathbf{q}(\boldsymbol{r}, t + \tau_q) = \mathbf{q}(\boldsymbol{r}, t) + \tau_q \frac{\partial \mathbf{q}(\boldsymbol{r}, t)}{\partial t} + O(\tau_q^2) \tag{23}$$

Then, keeping only the first-order term in τ_q and substituted into (22), we arrive at the expression (4), where the term $\tau_q \partial \mathbf{q}/\partial t$ describes the acceleration of heat propagation.

However, it is natural to assume that the temperature gradient at a given point depends not on the heat flow in the future $t + \tau_q$, but on the flow at the previous moment in time $t - \tau_q$. This is expressed by the following condition:

$$\mathbf{q}(\boldsymbol{r}, t - \tau_q) = -\kappa \nabla \theta(\boldsymbol{r}, t) \tag{24}$$

Expanding the left side (24) into a Taylor series we get:

$$\mathbf{q}(\boldsymbol{r}, t - \tau_q) = \mathbf{q}(\boldsymbol{r}, t) - \tau_q \frac{\partial \mathbf{q}(\boldsymbol{r}, t)}{\partial t} + O(\tau_q^2) \tag{25}$$

Here the term $-\tau_q \partial \mathbf{q}/\partial t$ describes the slowing down of heat propagation. Thus, in combination with the continuity Equation (1), we arrive at the following modified system describing heat transfer:

$$c\rho \frac{\partial \theta}{\partial t} + \nabla \cdot \mathbf{q} = 0 \tag{26}$$

$$-\tau_q \frac{\partial \mathbf{q}}{\partial t} + \mathbf{q} + \kappa \nabla \theta = 0 \tag{27}$$

The system (26) – (27) is equivalent to the following MCV equation for the temperature field:

$$\frac{\partial^2\theta}{\partial t^2}-\frac{1}{\tau_q}\frac{\partial\theta}{\partial t}+s_q^2\Delta\theta=0 \tag{28}$$

Note that the stationary state of MCV Equation (28) is the same as for the Fourier (3) and CV (5) equations, but the time evolution of temperature is different.

Let us analyze the consequences of the proposed modification. Assuming harmonic solutions (12), we have the following dispersion relation for the MCV equation:

$$\omega^2+i\frac{1}{\tau_q}\omega+s_q^2k^2=0 \tag{29}$$

From (29) we have two roots:

$$i\omega=\frac{1\pm\sqrt{1+4\tau_q^2s_q^2k^2}}{2\tau_q} \tag{30}$$

The schematic plots of dispersion curves (30) are represented in **Figure 4**.

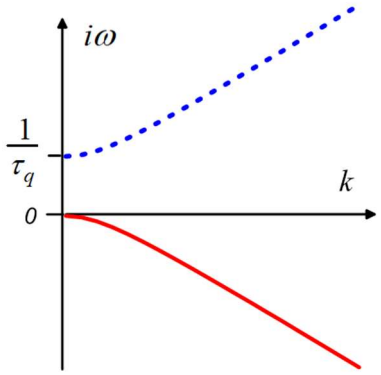

Figure 4. The schematic plots of dispersion curves for MCV equation.

The upper branch of dispersion curve corresponds to:

$$i\omega=\frac{1+\sqrt{1+4\tau_q^2s_q^2k^2}}{2\tau_q} \tag{31}$$

and describes the solutions growing in time that contradict the physical picture of the heat transfer process and are a consequence of the violation of the causality principle [38]. However, on the other hand, the solutions corresponding to the lower branch of the dispersion characteristic with describe damped in time spatial harmonics and can be used to describe the process of heat propagation.

$$i\omega=\frac{1-\sqrt{1+4\tau_q^2s_q^2k^2}}{2\tau_q} \tag{32}$$

4. Comparison of Fourier equation and modified Cattaneo-Vernotte equation

Let us compare Fourier and MCV equations. We write these equations in the similar form:

$$\frac{1}{\tau_q}\frac{\partial\theta}{\partial t} - s_q^2\Delta\theta = 0 \tag{33}$$

$$-\frac{\partial^2\theta}{\partial t^2} + \frac{1}{\tau_q}\frac{\partial\theta}{\partial t} - s_q^2\Delta\theta = 0 \tag{34}$$

The dispersion relation for Fourier Equation (33) is

$$i\omega = -\tau_q s_q^2 k^2 \tag{35}$$

The dispersion relation for MCV Equation (34) is

$$i\omega = \frac{1 - \sqrt{1 + 4\tau_q^2 s_q^2 k^2}}{2\tau_q}. \tag{36}$$

The schematic plots of (35) and (36) are represented in **Figure 5**.

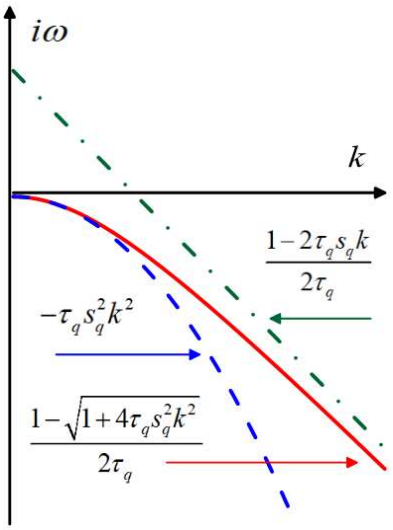

Figure 5. The schematic plot of dispersion curves for Fourier (dashed blue line) and MCV (solid red line) equations. The asymptote (37) is shown by dot-dashed line.

In the region of small k the dependence (36) coincides with dependence (35), while at $k \to \infty$it tends to the asymptote

$$i\omega = \frac{1 - 2\tau_q s_q k}{2\tau_q} \tag{37}$$

The analog of group speed for MCV equation is

$$i v_{MCV} = i\frac{d\omega}{dk} = -\frac{2\tau_q s_q^2 k}{\sqrt{1 + 4\tau_q^2 s_q^2 k^2}}. \tag{38}$$

This quantity tends to be constant $-s_q$at $k \to \infty$. On the other hand, taking into account (12) the analog of group speed for Fourier equation is

$$i v_F = i\frac{d\omega}{dk} = -2\tau_q s_q^2 k. \tag{39}$$

This quantity tends to infinity at $k \to \infty$.

4.1. The plate cooling

As an example, let us consider the one-dimensional problem of cooling a plate with thickness $2l$ uniformly heated to a temperature θ_0 and with zero temperature at the boundaries $x = \pm l$. In this case we have natural spatial scale l and we introduce new dimensionless variables $\tilde{t} = t/\tau_q$ and $\tilde{x} = x/l$. Then the Fourier equation is represented as

$$\frac{\partial \theta}{\partial \tilde{t}} - \lambda^2 \frac{\partial^2 \theta}{\partial \tilde{x}^2} = 0 \tag{40}$$

while MCV equation is

$$\frac{\partial^2 \theta}{\partial \tilde{t}^2} - \frac{\partial \theta}{\partial \tilde{t}} + \lambda^2 \frac{\partial^2 \theta}{\partial \tilde{x}^2} = 0 \tag{41}$$

where $\lambda = l_q/l$ is the ratio of the diffusion length to half of the plate thickness. Corresponding dispersion relations are

$$i\omega = -\lambda^2 k^2 \tag{42}$$

and

$$i\omega = \frac{1 - \sqrt{1 + 4\lambda^2 k^2}}{2}. \tag{43}$$

The solution to this problem in the frame of Fourier equation (40) is expressed by the following Fourier series [1]:

$$\theta_F = \frac{4\theta_0}{\pi} \sum_{m=0}^{\infty} \frac{(-1)^m}{(2m+1)} \cos\left[\frac{(2m+1)\pi}{2} \tilde{x}\right] \exp\left[-\frac{\lambda^2 (2m+1)^2 \pi^2}{4} \tilde{t}\right] \tag{44}$$

with decrement of temperature damping

$$d_{Fm} = \frac{\lambda^2 (2m+1)^2 \pi^2}{4}. \tag{45}$$

On the other hand, the solution to this problem in the case of MCV equation (41) is expressed by the following series:

$$\theta_M = \frac{4\theta_0}{\pi} \sum_{m=0}^{\infty} \frac{(-1)^m}{(2m+1)} \cos\left[\frac{(2m+1)\pi}{2} \tilde{x}\right] \exp\left[\frac{1 - \sqrt{1 + \lambda^2 (2m+1)^2 \pi^2}}{2} \tilde{t}\right] \tag{46}$$

with damping parameter

$$d_{Mm} = \frac{1 - \sqrt{1 + \lambda^2 (2m+1)^2 \pi^2}}{2}. \tag{47}$$

Thus, comparing damping parameters in (45) and (47) one can see that in case of MCV equation the higher harmonics decay more slowly than in case of Fourier equation in accordance with dispersion dependences (42) and (43).

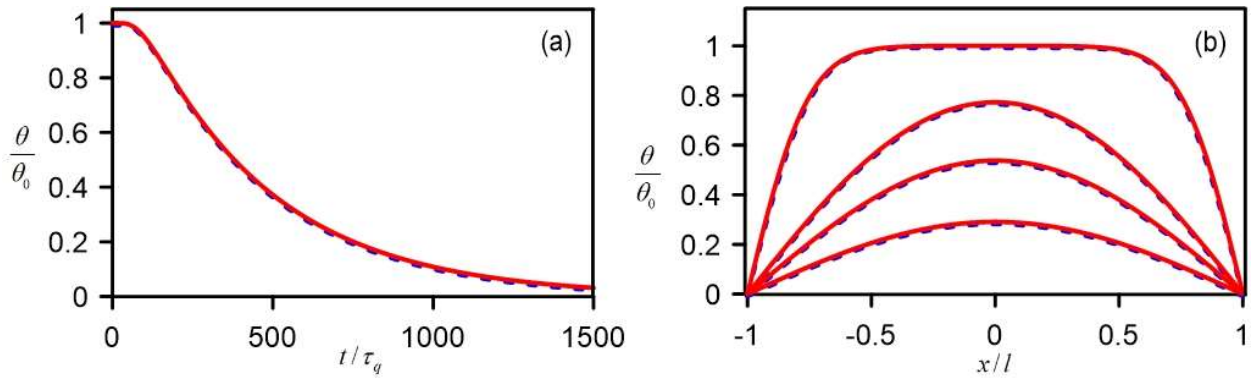

Figure 6. The process of cooling the thick plate with $l > l_q$ ($\lambda^2 = 0.01$). **(a)** Time dependences of temperature at the point $\tilde{x} = 0$; **(b)** Temperature profiles at different time ($\tilde{t} = 20, 200, 350, 600$). The solutions of Fourier equation are indicated by dashed blue lines. Solutions of MCV equation are shown by solid red lines.

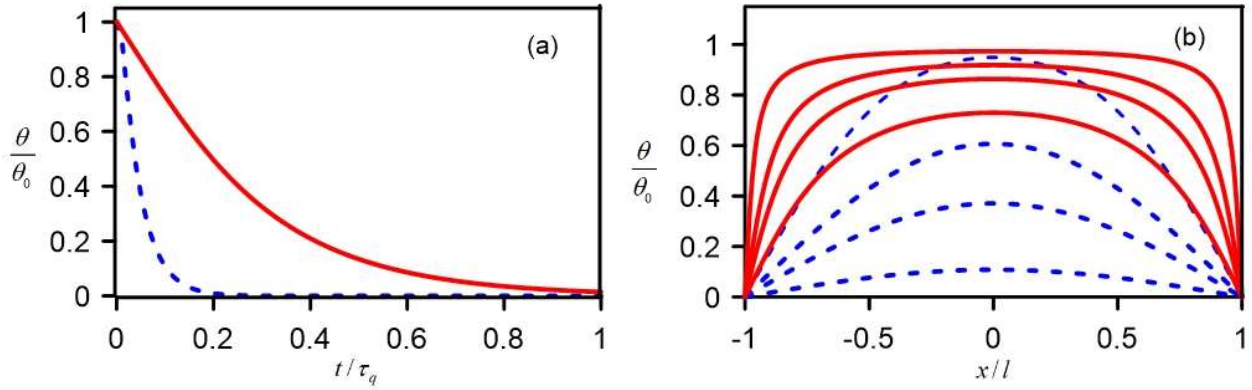

Figure 7. The process of cooling the thin plate with $l < l_q$ ($\lambda^2 = 10$). **(a)** Time dependences of temperature at the point $\tilde{x} = 0$; **(b)** Temperature distributions at different time ($\tilde{t} = 0.01, 0.03, 0.05, 0.1$). The solutions of Fourier equation are indicated by dashed blue lines. Solutions of MCV equation are shown by solid red lines.

The results of numerical calculations for the plates with different thicknesses are represented in **Figures 6** and **7**. It is seen that in the case of thick plates ($l > l_q$) the solution of the MCV equation (red solid curves in **Figure 6a,b**) coincides with the solution of the Fourier equation (blue dashed curves in **Figure 6a,b**). However, for thin plates ($l < l_q$) the solution to the Fourier equation demonstrates a rapid decrease in temperature gradients and faster cooling of the plate (blue dashed curves in **Figure 7a,b**) than in the case of the solution described by the MCV equation (red solid curves in **Figure 7a,b**).

To clarify the time evolution of Fourier and MCV solutions, we analyze the behavior of zero harmonics. Let us consider the cooling a plate (thickness $2l$) with $\theta_0 \cos(\pi x/2l)$ initial temperature and with zero temperature at the boundaries $x = \pm l$. In this case,

$$\theta_F = \theta_0 \cos\left(\frac{\pi}{2}\tilde{x}\right)\exp\left(-\frac{\lambda^2\pi^2}{4}\tilde{t}\right), \tag{48}$$

and

$$\theta_M = \theta_0 \cos\left(\frac{\pi}{2}\tilde{x}\right)\exp\left(\frac{1-\sqrt{1+\lambda^2\pi^2}}{2}\tilde{t}\right). \tag{49}$$

The dependence of the ratio of damping parameters d_M/d_Fas the function of λ is represented in **Figure 8**.

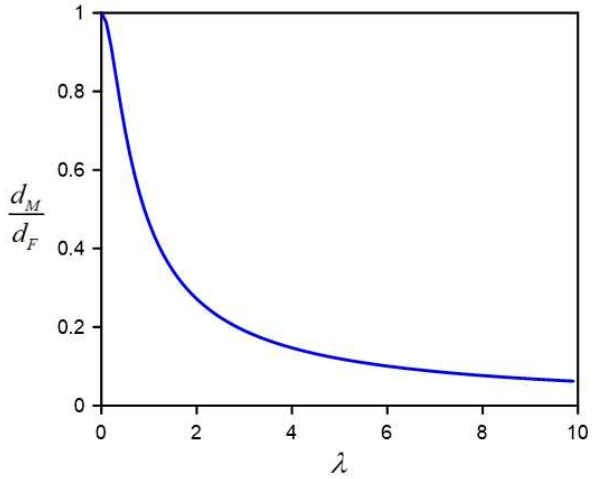

Figure 8. The dependence of damping parameters ratio d_M/d_F on the parameter λ.

For thick plates when $\lambda^2\pi^2 \ll 1$ we have

$$d_M \approx -\frac{\lambda^2\pi^2}{4} = d_F \tag{50}$$

and time behavior of Fourier and MCV solutions is practically the same. The temperature profiles at different times and the dependence of temperature at the central point of the plate on time are shown in **Figure 9**.

In opposite case of thin plate when $\lambda^2\pi^2 \gg 1$ we have

$$d_M \approx -\frac{\lambda\pi}{2} < d_F \tag{51}$$

and MCV equation predicts slower cooling than Fourier equation. The corresponding temperature profiles and time dependences are shown in **Figure 10**.

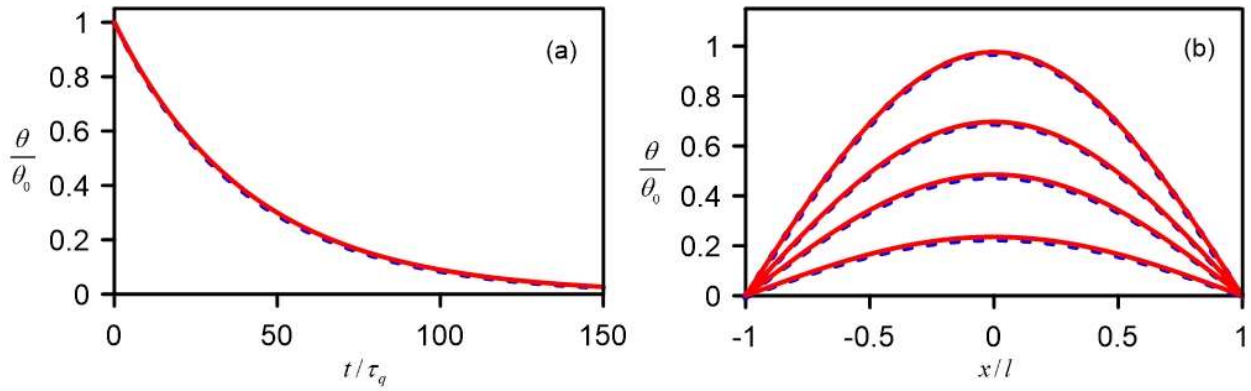

Figure 9. The process of cooling the thick plate with $l > l_q$ ($\lambda^2 = 0.01$). **(a)** Time dependences of temperature at the point $\tilde{x} = 0$; **(b)** Temperature distributions at different time ($\tilde{t} = 1, 15, 30, 60$). The solutions of Fourier equation are indicated by dashed blue lines. Solutions of MCV equation are shown by solid red lines.

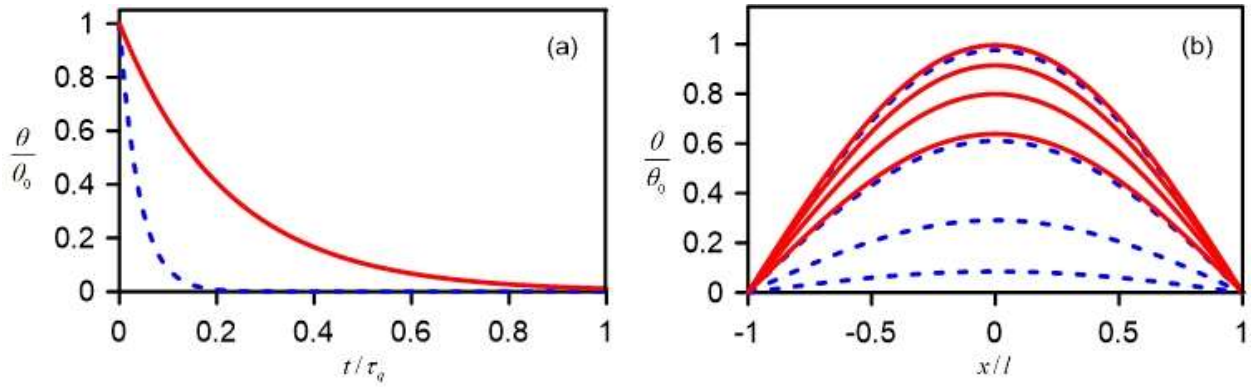

Figure 10. The process of cooling the thick plate with $l > l_q$ ($\lambda^2 = 0.01$). **(a)** Time dependences of temperature at the point $\tilde{x} = 0$; **(b)** Temperature distributions at different time ($\tilde{t} = 0.001, 0.02, 0.05, 0.1$). The solutions of Fourier equation are indicated by dashed blue lines. Solutions of MCV equation are shown by solid red lines.

Thus, it is seen that the differences between solutions of Fourier and MCV equations are noticeable only at small spatial scales, when the plate thickness is less than the diffusion length. This approach can be applied to describe the non-Fourier thermal effects at micro scales [8].

5. Conclusion

We propose an alternative relationship between heat flux and temperature gradient, which leads us to the MCV equation describing the evolution of temperature with a finite rate. Solutions of MCV equations have the same spatial temperature distributions as in the case of Fourier and CV equations but describe a different dynamics of heat transfer process. The peculiarities of MCV solutions and their comparison with Fourier solutions have been analyzed on the example of the simple problem of plate cooling. It was shown that on large spatial scales, when the plate thickness is greater than the thermal diffusion length, the differences between the solutions of MCV and Fourier equations are insignificant. However, in the case when the plate thickness is less than the diffusion length, the MCV equation predicts a slower cooling in accordance with a finite heat transfer rate.

Thus, it has been shown that the MCV equation provides the finite rate of transfer processes, but it does not have the disadvantages of a CV equation, which predicts many paradoxical results associated with the possible propagation of heat in the form of real harmonic waves. The same approach can be applied to describe the diffusion processes in solids.

Acknowledgments: The author is grateful to the reviewers for their very useful and stimulating comments and suggestions.

Conflict of interest: The author declares no conflict of interest.

References

1. Carslow HS, Jaeger JC. Conduction of heat in solids. Oxford University Press, Oxford, UK, 1959.
2. Christov CI, Jordan PM. Heat Conduction Paradox Involving Second-Sound Propagation in Moving Media. Physical Review Letters. 2005; 94(15). doi: 10.1103/physrevlett.94.154301

3. Chandrasekharaiah DS. Hyperbolic Thermoelasticity: A Review of Recent Literature. Applied Mechanics Reviews. 1998; 51(12): 705-729. doi: 10.1115/1.3098984
4. Joseph DD, Preziosi L. Heat waves. Reviews of Modern Physics. 1989; 61(1): 41-73. doi: 10.1103/revmodphys.61.41
5. Green AE, Naghdi PM. A re-examination of the basic postulates of thermomechanics. In: Proceedings of the Royal Society of London Series A: Mathematical and Physical Sciences. 1991; 432(1885): 171-194. doi: 10.1098/rspa.1991.0012
6. Cimmelli VA, Kosinski W, Saxton K. Modified Fourier law: Comparison of two approaches, Archives of Mechanics. 1992; 44, 409-415.
7. Ignaczak J. Soliton-like solutions in a nonlinear dynamic coupled thermoelasticity. Journal of Thermal Stresses. 1990; 13(1): 73-98. doi: 10.1080/01495739008927025
8. Tzou DY. A Unified Field Approach for Heat Conduction From Macro- to Micro-Scales. Journal of Heat Transfer. 1995; 117(1): 8-16. doi: 10.1115/1.2822329
9. Christov CI. On frame indifferent formulation of the Maxwell–Cattaneo model of finite-speed heat conduction. Mechanics Research Communications. 2009; 36(4): 481-486. doi: 10.1016/j.mechrescom.2008.11.003
10. Oldroyd JG. On the formulation of rheological equations of state. In: Proceedings of the Royal Society of London Series A Mathematical and Physical Sciences. 1950; 200(1063): 523-541. doi: 10.1098/rspa.1950.0035
11. Khan U, Ahmad S, Hayyat A, et al. On the Cattaneo–Christov Heat Flux Model and OHAM Analysis for Three Different Types of Nanofluids. Applied Sciences. 2020; 10(3): 886. doi: 10.3390/app10030886
12. Jafarimoghaddam A, Turkyilmazoglu M, Pop I. Threshold for the generalized Non-Fourier heat flux model: Universal closed form analytic solution. International Communications in Heat and Mass Transfer. 2021; 123: 105204. doi: 10.1016/j.icheatmasstransfer.2021.105204
13. Turkyilmazoglu M. Heat Transfer Enhancement Feature of the Non-Fourier Cattaneo–Christov Heat Flux Model. Journal of Heat Transfer. 2021; 143(9). doi: 10.1115/1.4051671
14. Joseph DD, Preziosi L. Addendum to the paper “Heat waves” [Rev. Mod. Phys. 61, 41 (1989)]. Reviews of Modern Physics. 1990; 62(2): 375-391. doi: 10.1103/revmodphys.62.375
15. Sobolev SL. On hyperbolic heat-mass transfer equation. International Journal of Heat and Mass Transfer. 2018; 122: 629-630. doi: 10.1016/j.ijheatmasstransfer.2018.02.022
16. Cattaneo C.On the Calculation of Certain Potentials and Their Intervention in the Solving of Particular Harmonic Problems (Italian). In: Proceedings of the Mathematical and Physical Seminar of the University of Modena and Reggio Emilia, 1948; 3, 29-45.
17. Cattaneo C. A form of heat equation which eliminates the paradox of instantaneous propagation. Comptes Rendus de l'Academie des Sciences. 1958; 247, 431-433.
18. Vernotte P. Paradoxes in the continuous theory of the heat equation. Comptes Rendus de l'Academie des Sciences. 1958; 246, 3154-3155.
19. Vernotte P. The true heat equation. Comptes Rendus de l'Academie des Sciences. 1958; 247, 2103.
20. O¨zis¸ik MN, Tzou DY. On the Wave Theory in Heat Conduction. Journal of Heat Transfer. 1994; 116(3): 526-535. doi: 10.1115/1.2910903
21. Mandrusiak GD. Analysis of Non-Fourier Conduction Waves from a Reciprocating Heat Source. Journal of Thermophysics and Heat Transfer. 1997; 11(1): 82-89. doi: 10.2514/2.6204
22. Xu M, Wang L. Thermal oscillation and resonance in dual-phase-lagging heat conduction, International Journal of Heat and Mass Transfer. 2002; 45(5), 1055-1061.
23. Barletta A, Zanchini E. Hyperbolic heat conduction and thermal resonances in a cylindrical solid carrying a steady periodic electric field, International Journal of Heat and Mass Transfer. 1996; 39 (6), 1307-1315.
24. Özisik MN, Vick B. Propagation and reflection of thermal waves in a finite medium, International Journal of Heat and Mass Transfer. 1984; 27 (10), 1845-1854.
25. Tzou DY. Shock wave formation around a moving heat source in a solid with finite speed of heat propagation, International Journal of Heat and Mass Transfer. 1989; 32 (10), 1979-1987.
26. Carey GF, Tsai M. Hyperbolic heat transfer with reflection. Numerical Heat Transfer. 1982; 5(3): 309-327. doi: 10.1080/10407788208913451
27. Kheibari AK, Jafari M, Nazari MB. Propagation of heat wave in composite cylinder using Cattaneo- Vernotte theory. International Journal of Heat and Mass Transfer. 2020; 160: 120208. doi: 10.1016/j.ijheatmasstransfer.2020.120208

28. van der Merwe AJ, van Rensburg NFJ, Sieberhagen RH. Comparing the dual phase lag, Cattaneo-Vernotte and Fourier heat conduction models using modal analysis. Applied Mathematics and Computation. 2021; 396: 125934. doi: 10.1016/j.amc.2020.125934
29. Nosko O. Perfect thermal contact of hyperbolic conduction semispaces with an interfacial heat source. International Journal of Heat and Mass Transfer. 2021; 164: 120541. doi: 10.1016/j.ijheatmasstransfer.2020.120541
30. Yuvaraj R, Senthil Kumar D. Numerical simulation of thermal wave propagation and collision in thin film using finite element solution. Journal of Thermal Analysis and Calorimetry. 2020; 142(6): 2351-2369. doi: 10.1007/s10973-020-09346-y
31. Kovács R, Rogolino P. Numerical treatment of nonlinear Fourier and Maxwell-Cattaneo-Vernotte heat transport equations. International Journal of Heat and Mass Transfer. 2020; 150: 119281. doi: 10.1016/j.ijheatmasstransfer.2019.119281
32. Auriault JL. The paradox of fourier heat equation: A theoretical refutation. International Journal of Engineering Science. 2017; 118: 82-88. doi: 10.1016/j.ijengsci.2017.06.006
33. Maillet D. A review of the models using the Cattaneo and Vernotte hyperbolic heat equation and their experimental validation. International Journal of Thermal Sciences. 2019; 139: 424-432. doi: 10.1016/j.ijthermalsci.2019.02.021
34. Mehrer H. Diffusion in Solids. Springer Berlin Heidelberg; 2007. doi: 10.1007/978-3-540-71488-0
35. Litvinenko YE, Schlickeiser R. The telegraph equation for cosmic-ray transport with weak adiabatic focusing. Astronomy & Astrophysics. 2013; 554: A59. doi: 10.1051/0004-6361/201321327
36. Tautz RC, Lerche I. Application of the three-dimensional telegraph equation to cosmic-ray transport. Research in Astronomy and Astrophysics. 2016; 16(10): 162. doi: 10.1088/1674-4527/16/10/162
37. Zhang D, Ostoja-Starzewski M. Telegraph equation: two types of harmonic waves, a discontinuity wave, and a spectral finite element. Acta Mechanica. 2019; 230(5): 1725-1743. doi: 10.1007/s00707-018-2356-3
38. Sommerfeld A. Introduction to Partial Differential Equations. Partial Differential Equations in Physics. 1949; 32-62. doi: 10.1016/b978-0-12-654658-3.50006-9

Thermal Science and Engineering 2024, 7(2), 8207.
https://doi.org/10.24294/tse.v7i2.8207

Review

A 7th Law of Thermodynamics and its climate implications

Jim Baird

Thermodynamic Geoengineering, 3217 Jingle Pot Road, Nanaimo, BC V9R 7C6, Canada; jim.baird@gwmitigation.com

CITATION

Baird J. A 7th Law of Thermodynamics and its climate implications. Thermal Science and Engineering. 2024; 7(2): 8207. https://doi.org/10.24294/tse.v7i2.8207

ARTICLE INFO

Received: 2 March 2024
Accepted: 15 April 2024
Available online: 20 June 2024

Abstract: Conversion of the ocean's vertical thermal energy gradient to electricity via OTEC has been demonstrated at small scales over the past century. It represents one of the planet's most significant (and growing) potential energy sources. As described here, all living organisms need to derive energy from their environment, which heretofore has been given scant serious consideration. A 7th Law of Thermodynamics would complete the suite of thermodynamic laws, unifying them into a universal solution for climate change. 90% of the warming heat going into the oceans is a reasonably recoverable reserve accessible with existing technology and existing economic circumstances. The stratified heat of the ocean's tropical surface invites work production in accordance with the second law of thermodynamics with minimal environmental disruption. TG is the OTEC improvement that allows for producing two and a half times more energy. It is an endothermic energy reserve that obtains energy from the environment, thereby negating the production of waste heat. This likewise reduces the cost of energy and everything that relies on its consumption. The oceans have a wealth of dissolved minerals and metals that can be sourced for a renewable energy transition and for energy carriers that can deliver ocean-derived power to the land. At scale, 31,000 one-gigawatt (1-GW) TG plants are estimated to displace about 0.9 W/m^2 of average global surface heat into deep water, from where, at a depth of 1000 m, unconverted heat diffuses back to the surface and is available for recycling.

Keywords: marine energy; global warming; heat to work; heat engine; waste heat; ocean thermal stratification; global energy supply

1. Introduction

In 1922, Alfred J. Lotka, building on principles from statistical physics and the second law of thermodynamics, particularly the work of Ludwig Boltzmann, articulated the MPP that living organisms need "available energy" from their environment to survive and thrive and that organisms that best harvest energy from their environment will be more successful, leading to larger populations and greater biomass. In his 1950 Ph.D. dissertation, H. T. Odum proposed, based on Lotka's work and Charles Darwin's theory of natural selection, a 4th Law of Thermodynamics that proposes maximization of power for valuable purposes is the criterion for natural selection [1]. In his 1996 book "Environmental Accounting: Emergy and Environmental Decision Making," Odum proposed a 5th law suggesting energy flows through the universe are organized in a self-organizing hierarchy for maximum empowerment [2]. And in 2001, Odum proposed the coupling of biogeochemical cycles to energy transformation hierarchies in a 6th law that proposes energy must be degraded to concentrate materials and that the quantity of material flow also decreases in each successive step in a series of energy transformations [1].

The purpose of this paper is to propose a 7th Law of Thermodynamics that is an amalgam of the MPP and the law of supply and demand, which states that if a product,

including energy, that is a product of an exothermic reaction thereby releases heat into the environment is in high demand and low supply, the price will increase. Conversely, if there is low demand, as is the case of an endothermic reaction that imports energy from its surrounding environment, the energy is a reactant and is in plentiful supply, and the price of the energy will decrease.

Energy is vital to living organisms, but an economic imperative drives a large swath of humanity. The lower the energy cost, the more society can consume and the more successful it will be as a species. The most plentiful and cheapest available energy source is impeded by its perceived high capital cost. A 7th Law of Thermodynamics incorporating the MPP and the Law of Supply and Demand can break this embargo and complete the suite of thermodynamic laws, making them a unifying law of energy and economics plus a blueprint for a holistic solution to one of the century's most significant challenges.

2. Energy sources

Reasonably recoverable reserves are the quantity of a resource reliably determined to exist and that can be recovered under current technological and economic conditions [3]. To be reasonably assured, there must be a high level of confidence in the existence and recoverability of the resource based on geological evidence and engineering data, which is often obtained through drilling and sampling of an area. Furthermore, to be recoverable, there must be enough of the resource that it can be extracted with existing technology and under current economic conditions in view of the cost of extraction, market prices, and regulatory or environmental constraints.

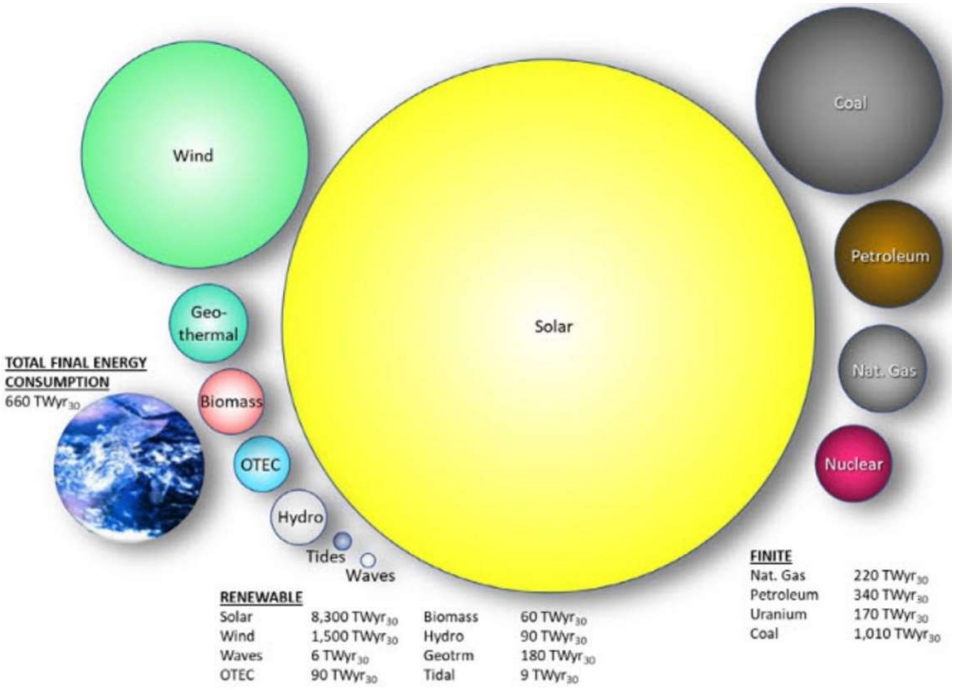

Figure 1. Estimated finite and renewable planetary energy reserves.

Annual yield is shown for the renewable resources. Total recoverable reserves are shown for the finite resources. Yearly potential is shown for the renewables (the volume of each sphere is proportional to the corresponding reserve).

Per **Figure 1**, Perez and Perez, for renewable resources, extended the definition of 'reasonably recoverable reserves' to a 30-year lifecycle to be consistent with the long-term reserve numbers for conventional finite resources (the 30 years commonly used for economic assessments and planning purposes). All reserves in **Figure 1** graphic are reported in TWyr and given the 30-year time frame considered for renewables and consumption, as $TWyr_{30}$ [4].

3. Global warming as an energy problem

EEI is a fundamental measure of climate change that encompasses changes in climate patterns, including global warming, but also changes in precipitation, extreme weather events, and impacts on natural and human systems [5]. Global warming is the persistent rise in Earth's average surface temperature due to human activities that increase greenhouse gas concentrations in the atmosphere, leading to environmental and societal impacts, including heatwaves, melting ice, rising sea levels, and disrupted ecosystems. EEI is the difference between the amount of solar energy absorbed by the Earth and the amount of energy the Earth radiates back into space. It is estimated to be 0.9 W/m^2 of the Earth's total surface of 5.1×10^{14} m^{-2} or about 460 TWyr or 13,800 $TWyr_{30}$ [6], which is 115% more than the total of all the energy sources shown in **Figure 1**. Moreover, the rate of the EEI is rising. Satellite data from the Clouds and the Earth's Radiant Energy System have shown that the EEI doubled between 2005 and 2019 [7]. Ocean heat content data shows about 90% of the EEI has been absorbed by the ocean, and the World Meteorological Organization has reported that the upper 2000 m of the ocean continues to warm at a significant rate [8]. Per **Figure 2**.

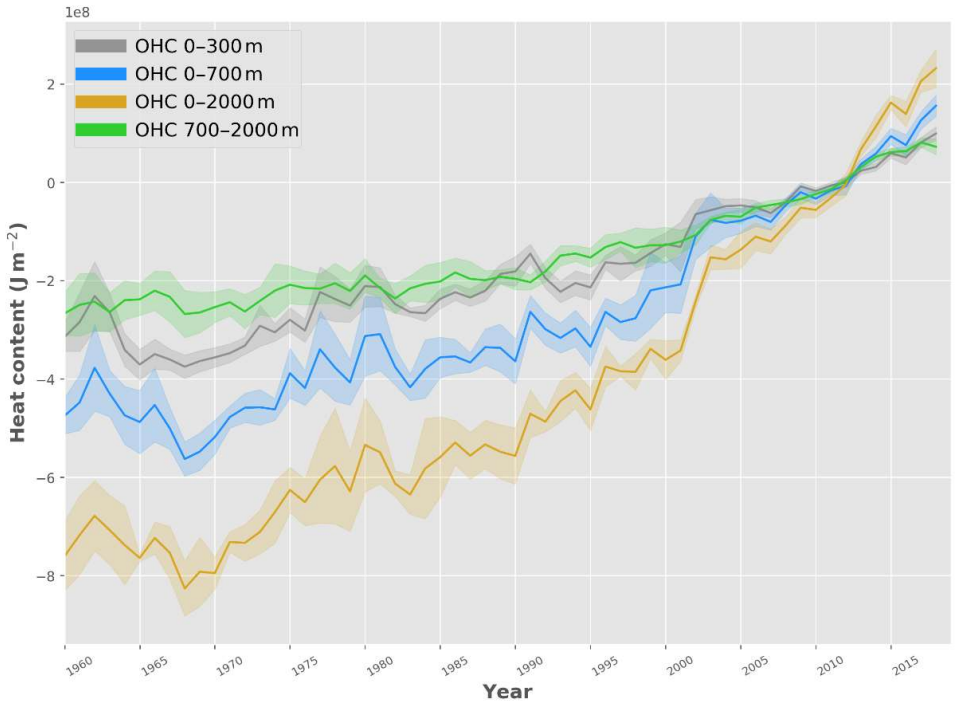

Figure 2. Ensemble mean time series and ensemble standard deviation (2σ, shaded) of global ocean heat content anomalies relative to the 2005–2017 climatology for the 0–300 m (gray), 0–700 m (blue), 0–2000 m (yellow) and 700–2000 m depth layer (green) [9].

Global warming is an outcome of energy use. The burning of fossil fuels is the primary source of GHG emissions, particularly CO_2, that trap heat in the atmosphere. Natural gas, primarily composed of methane, is a potent GHG that leaks during its extraction and transportation and is another major contributor to global warming. As are other gases like nitrous oxide released by the burning of fossil fuels and fluorinated gases from industrial processes. Rising global energy demand driven by population growth, industrialization, and economic development exacerbates global warming, as does the waste heat of energy consumption and inefficient energy usage [10]. Transitioning to renewable energy is vital to mitigating global warming. However, solar and wind are intermittent, and the other baseload renewable energy sources listed in **Figure 1** total only about 66% of current energy consumption. With the proviso, the 90 $TWyr_{30}$ for OTEC shown in **Figure 1** is a gross underestimation of the technology's potential, as is discussed below. Furthermore, fusion energy, touted by some as energy's Holy Grail and not shown in **Figure 1**, is advanced as a proxy for all exothermic energy sources [11].

The UNFCCC secretariat is the United Nations entity tasked with supporting the global response to the threat of climate change [12]. Its 1992 objective was to stabilize greenhouse gas concentrations in the atmosphere at a level that would prevent dangerous human interference with the climate system in a time frame that allows ecosystems to adapt naturally and enables sustainable development [13]. If the use of fossil fuels had ceased in 1992, a safe Holocene climate could have been maintained. However, fossil fuel usage has increased because atmospheric CO_2 levels are now 40% higher than human civilization has ever witnessed, increasing by 0.6% annually (2.57/421 ppm) [14].

There is significant inertia to a voluntary reduction of fossil fuel consumption despite the environmental and climate imperatives to do so [15]. Many economies are heavily dependent on fossil fuels, and shifting away from that energy source will require significant changes in infrastructure and technology, which can be costly and disruptive. Fossil fuels have been relatively cheap and abundant, providing a stable and reliable energy source, and the alternatives will require substantial upfront investments and technological development to become cost-competitive. The fossil fuel industry provides jobs and supports various sectors such as mining, transportation, refining, and petrochemicals, so transitioning away from fossil fuels will lead to job losses and economic downturns in regions reliant on these industries. Significant capital investments in existing fossil fuel infrastructure could be lost if those assets are abandoned before the end of their useful lives and the industry wields considerable political power and influence that can impede the policy changes necessary for transitioning to cleaner energy sources. Many countries prioritize energy security, ensuring they have a stable and independent energy supply, which fossil fuels have historically provided. Global markets are deeply intertwined with fossil fuels, and a shift away from fossil fuels could destabilize them, leading to economic uncertainty and fluctuations. While renewable energy technologies have advanced, they still face challenges in terms of efficiency, storage, and scalability; therefore, fossil fuels will, at best, and for decades, continue to be a bridge to a renewable energy future [16].

Fossil fuel drawbacks, such as GHGs, lead to significant global warming and climate change impacts, including more frequent and severe weather events, increased

sea-level rise, and disruptions to ecosystems and agriculture. Extracting, transporting, and burning fossil fuels can cause significant environmental damage, including oil spills, habitat destruction, air and water pollution, and soil contamination. These activities harm biodiversity and degrade natural ecosystems. Fossil fuel burning releases pollutants like sulfur dioxide and nitrogen oxides that can cause respiratory and cardiovascular diseases, cancer, and premature deaths, which can be avoided with the improved air quality and public health that renewable energy can deliver [17]. Renewable energy sources are local and inexhaustible, enhancing energy security while reducing vulnerability to geopolitical conflicts and market fluctuations that fossil fuels have historically produced [18]. Transitioning to renewable energy can drive economic growth by creating new industries and job opportunities that can lead to more resilient and diversified economies [19]. Although there are upfront costs associated with transitioning to renewable energy, the enduring savings can be substantial. Renewable energy sources have lower operating and maintenance costs compared to fossil fuel infrastructure, and the cost of renewable energy technologies has been steadily decreasing. Fossil fuels are non-renewable resources, and their extraction becomes more difficult and expensive over time as reserves are depleted; therefore, transitioning to renewable energy affords a more sustainable and long-term energy future.

Addressing climate change and environmental degradation is a moral imperative for ensuring a livable planet [20]. Nevertheless, governments and businesses focus on short-term economic growth and profits, whereas the benefits of transitioning to renewables are more persistent. As the following demonstrates, both short- and long-standing economic growth, profits, and "available energy", as well as resources that all living organisms need to survive and thrive in their environment, are available in the oceans and are the wages of ocean thermal energy conversion.

4. OTEC as a sustainable source of energy for mankind

Perez and Perez qualified their estimate of 90 $TWyr_{30}$ (3 TWyr) for OTEC in **Figure 1**, cautioning, "OTEC's economic potential is unknown as it is still an immature technology with no commercial plant operating" [4]. And the UN's GESAMP has sanctioned this position by pointing out, "After more than four decades of research and development, OTEC has still not been deployed at scale" [21].

In 1998, a team led by physicist Martin Hoffert from New York University determined that stabilizing the Earth's atmospheric CO_2 levels would require a tenfold increase in carbon-emission-free power generation over the following 50 years [22]. At that time, only 1.5 TWyr of carbon-emission-free power was being produced. So, to achieve the stabilization the team was seeking, Hoffert's team concluded that non-fossil-fuel energy sources would need to deliver at least 50% of the projected 30 TWyr global power demand by 2050. Therefore, carbon-emission-free power generation will need to reach 15 TWyr by the middle of the century.

Seven years later, Richard Smalley offered his 60 TWyr challenge, which noted in a list of the top 10 issues facing humankind, at the top of which was energy, that it was also the solution to the remaining nine concerns [23].

In 2005, it was determined the worldwide power resource that could be extracted

from the steady-state operation of OTEC was estimated at 3 TWyr [24]. Since this was only a fifth of the energy Hoffert's team was seeking, OTEC was and subsequently has remained, until recently relegated to the list of potential renewable energy also-rans.

At this formative stage of the carbon divestment and renewable investment era, OTEC was handicapped by a lowballed potential that its proponents have never recovered from.

Subsequently, OTEC's maximum annual net power production has been reassessed upward to at least 31 TW [25]. And it is the contention of this paper that for the next 3000 years, TG can deliver 31 TWyr of energy by converting the heat of global warming to work, which in turn mitigates every consequence of global warming while returning atmospheric CO_2 levels to their preindustrial level, and it can produce 25 TWyr in perpetuity thereafter (Jia et al. estimated the lower steady-state OTEC power maxima was 8 to 10.2 TWyr, but TG has 2.5 times the efficiency of conventional OTEC, thus as much as 25 TWyr can be supplied in perpetuity) [26].

In 2018, the Jia et al. paper also rebutted the 2015 paper of Kwiatkoski et al. that used a model that boosted the background diffusivity of the top 1000 m of the ocean by a factor of 600 and then regarded this as a proxy for the large-scale effects of technologies like OTEC that rely on seawater properties from different vertical layers [27]. To this day, the GESAMP continues relying on the Kwiatkoski paper by claiming "that large-scale deployment of OTEC heat pipes for purposes of thermodynamic geoengineering would be potentially disruptive to the marine environment considering that, by definition, it would significantly reduce sea surface temperatures on a regional scale while having all the same localized environmental outcomes as conventional OTEC [21].

The paper "Addressing the Urgent Need for Direct Climate Cooling: Rationale and Options", on the other hand, argues that direct climate cooling approaches, like OTEC, have the potential to reduce local to global portions of human-induced warming [28]. What's more, of the 14 cooling methods listed in this paper, only two, MEER and OTEC, generate the energy species need to survive, while the other thirteen radiate energy away from the surface. In the case of MEER, reflection is the technology's primary function and is degraded when its mirrors are focused on a point source for the purpose of producing energy from a concentrated solar system. Whereas solar energy is intermittent, OTEC is baseload [29].

The technical and economic feasibility, long-term impact and efficiency, environmental impact, potential risks, and ethical considerations associated with large-scale ocean-based energy conversions are beyond the scope of this paper but are addressed in the papers "Global Warming, a Global Energy Resource, Negative-CO_2-Emissions Ocean Thermal Energy Conversion, and the book Thermodynamic Geoengineering: The solution to global warming!" [25,29,30]. In summary, these documents reveal that no showstoppers impede the testing of this technology. At least in the eyes of the most populous nations, the ones at most risk of the impacts of climate change, the energy price takers, those bereft of their own natural resources, or internal energy sources. Should any problems arise during the scaling of this solution, the research of Rajagopalan and Nihous in the paper "An Assessment of Global Ocean Thermal Energy Conversion Resources with a High-Resolution Ocean General

Circulation Model" indicate, "When turning off the prescribed OTEC sources and sinks in the model, the environment is shown to relax to its pre-OTEC condition. The time scales for both reverse and direct processes are similar" [31]. At a scale of 100 MW or greater, TG becomes economically viable and profitable, allowing for the plowing of profits into R&D scaling and the buildout of the fleet of platforms necessary to reverse surface heating and global warming.

Three thousand years is 100 times the 30-year economic assessments and planning period shown in **Figure 1** for "finite" energy sources. Times 31 would be 93,000 TW, or 53 times the finite sources shown in **Figure 1**. Over the course of these 3000 years utilizing TG technology, the EEI would be depleted to zero. With TG, surface temperatures would be returned to the preindustrial level in 226 years, at about the same rate of decline as it increased, and would be maintained by recycling the heat trapped in the ocean 12 more times [25].

The approximate linear rate of global warming between 1970 and 2008 was around 0.18 ℃ per decade, based on analyses of global temperature data [32]. However, in recent years, the rise in global surface temperatures has exceeded this long-term trend, with eight of the past nine years recording higher temperatures than the historical average. In 2023, former NASA scientist Dr. James Hansen and his colleagues published a paper titled "Global Warming in the Pipeline", which argues that the rate of warming is expected to increase to between 0.27 ℃ and 0.36 ℃ per decade over the next 30 years, which represents a 50% to 100% increase in the rate of warming since 1970 [33].

The heat of global warming is potential energy that can be converted to work at an efficiency of 7.6%, with the remainder being transferred to 1000 m from where it returns to the surface in about 226 years [34]. The diffusion rate of heat from deep water is one cm/d below the mixed layer (four meters a year) and one meter/d through that layer; therefore, the 226-year period. After which 92.4% of the initial heat can be recycled [35]. Through repeated recycling, virtually all the warming heat can be converted to work, and the waste heat of those conversions can be dissipated to space, effectively managing the excess heat while mitigating rising global temperatures.

The 7.6% efficiency rate of conversion of surface heat to work was calculated by Los Alamos Labs experimental physicist Melvin Prueitt in his 2007 patent filing, "Heat transfer for ocean thermal energy conversion" [34].

Global warming generates more energy than can be consumed in a single tranche; therefore, the low, in engineering terms, thermal efficiency of converting warming heat to work does not limit the amount of work that can be produced from the heat of global warming. Converting the heat of warming heat, which is a surface effect, to work and to sequester the balance mitigates every consequence of global warming, including the decline of Arctic Sea ice, melting glaciers, decreasing snow cover, rising sea levels, the frequency and strength of storms, increasing humidity, and the rising heat content of the oceans [31,36]. The conversion of ocean heat to work that is undertaken on land is an extraction of heat from the ocean.

The fundamental measure of global warming is the heat uptake of the ocean, which is incontrovertible evidence that the Earth is warming [37].

Resplandy et al. used the measurement of atmospheric O_2 and CO_2 levels as the oceans warm and release these gases as a proxy for global warming. They calculated

that between 1991 and 2016, the average warming amounted to about 1.29 ± 0.79 × 10^{22} joules of heat (409 TW/year), equivalent to a planetary energy imbalance of 0.80 ± 0.49 W/m^2 of the Earth's surface [38]. They determined that about 1.11 ± 0.68 per meg (parts per million (ppm)) of these gases were going into the atmosphere on account of the warming of the tropical surface annually, with the concentrations of these gases being 1 part O_2 to 1.05 parts CO_2. So, about 0.56 ppm of CO_2 was added to the atmosphere each year of the study.

The mean date for the Resplandy paper was 2004, and the mean rate of warming was 409 TW, so it can be assumed there will be about three more doublings of this amount of heat to at least 3300 TWyr by 2053, the earliest we are likely to be able to start bringing temperatures under control by doubling the current installed capacity of 100 kW/yr of OTEC power every year. Since it is assumed that it will take 226 more years to bring the surface temperature down to the preindustrial level, the conversion of about 409 TWyr to work each year going forward from 2053 would accomplish that goal.

Figure 3 is a depiction of a perceived route to scaling TG plants.

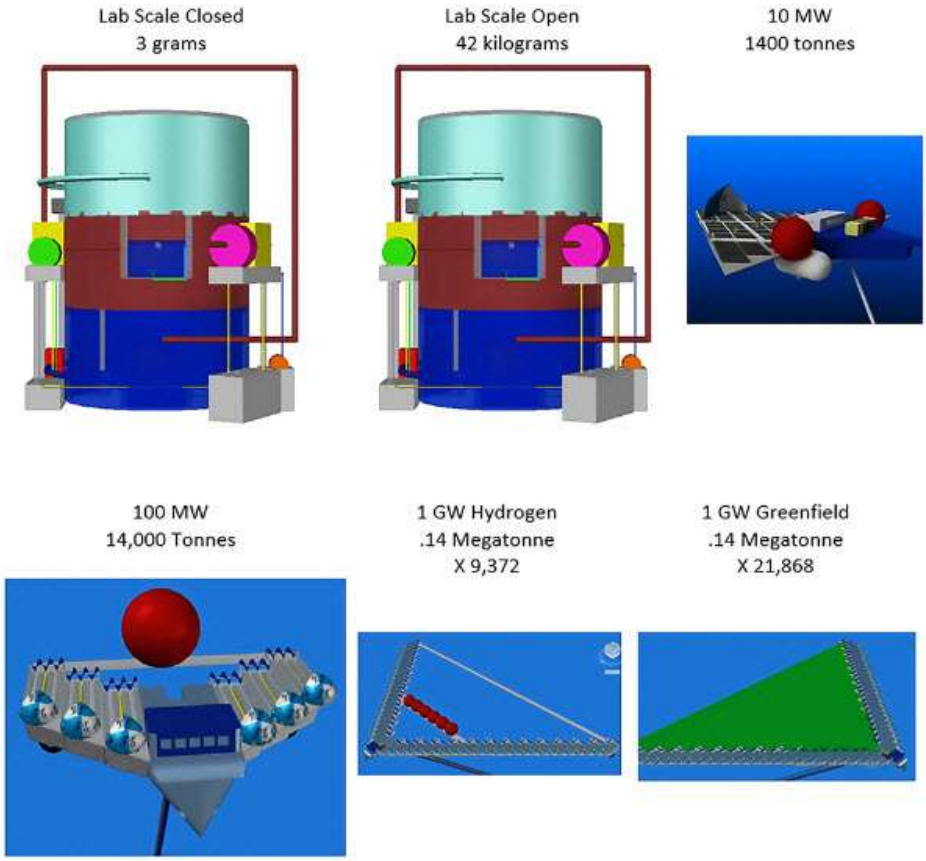

Figure 3. A depiction of a perceived route to scaling TG plants from a closed lab scale model to 1 GW capacity and beyond. The lab scale model was one of the qualified entries in the $100M XPRIZE for carbon removal and the figure shows the quantities of CO_2 that would be sequestered by the various-sized systems and the number of plants that would be required to produce 31 TWyr of power.

5. The ocean thermal dam

Between 1844 and 1854, the English scientist J. P. Joule worked on the problem of the relation between the amount of work spent to bring about the liberation of heat and the amount of heat that was liberated by that work [39]. He used a paddlewheel device submerged in a heat-insulated vessel attached by a series of pulleys to a weight. As the weight fell, it imparted rotation to the paddle that, in turn, produced heat inside the vessel. The work done was determined to be equal to the decrease in the potential energy of the weight (gravity times the distance the weight fell). Through multiple experiments, Joule discovered the direct proportionality relationship between spent work and the quantity of heat obtained (his mechanical equivalent to heat) is 0.002345 kcal/kgf-m. A "Joule," therefore, equals 427 kgf·m/kcal, which is the equivalent of 4.19 watts. It is equivalent to a 1-kilogram mass (m) of water raised to a height (h) of 427 m times gravity (g) (equal to 9.8 m/s²), producing a PE equal to m × g × h, as expressed in the International System of Units joules per kilogram.

A ΔT of 26 ℃ between a tropical surface and water at a depth of 1000 is equivalent to a PE of 11,102 m times the Carnot efficiency, which is 7.6% for TG × 0.5 (because this potential is considered to be reversible) = 421 m. Or just under twice the height of the Hoover Dam. Moreover, this untapped PE can be found throughout the tropics, where the average surface temperature ranges between 25 ℃ and 28 ℃, and at a depth of 1000 m, it is 4 ℃, so the average Δ ranges between 21 ℃ and 24 ℃.

6. The physics

The law of conservation of energy dictates that energy can be transformed from one form to another but can be neither created nor destroyed.

The second law of thermodynamics governs heat engines that conduct heat from hot regions to cold to produce work. Since they cannot do this thoroughly, some of the input heat is dissipated into the environment.

The first law of heat engines is expressed as: $W = Q_H - Q_L$

where:

W is the work output by the engine expressed in Joules (J);

Q_H is heat input from a hot reservoir expressed in Joules (J);

Q_L is heat released into the cold reservoir expressed in Joules (J).

Figure 4 is a schematic representation of the first and second laws of thermodynamics.

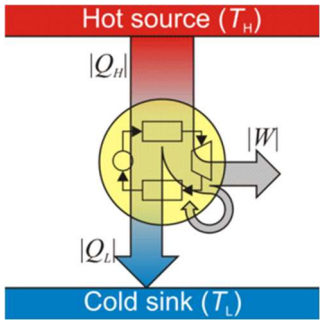

Figure 4. A schematic representation of the first and second laws of thermodynamics.

Heat (Q_H) from a hot source like the tropical ocean surface, moved through a heat engine (in yellow) consisting of an evaporator, a turbine, a condenser, and a pump, produces work (W) and waste heat (Q_L) that is released as the latent heat of condensation of the working fluid from the condenser to the cold ocean at a depth of 1000 m. Some of the work is circulated back into the system to power the pump required to force the condensed working fluid back into the evaporator.

The thermal efficiency of a heat engine is defined as the ratio of the work output to the heat input, expressed by the formula: $W = Q_H - Q_L/Q_H$

The French engineer, Sadi Carnot, showed that the ratio of Q_H to Q_L is the same as the ratio between the high temperature (T_H) and the lower temperature (T_L) of a heat engine. Therefore, Carnot efficiency is expressed as: $1 - (T_H - T_L)/T_H$.

Since the Carnot cycle is an ideal, the Rankine cycle represents the actual processes of a power plant using a vaporized working fluid and is less efficient than the Carnot cycle because it includes entropy and heat losses.

For the prime energy-producing OTEC region of the ocean shown in **Figure 5**, the theoretical Carnot efficiency is assumed to be about 1 − ((301 − 277)/301) or 8%.

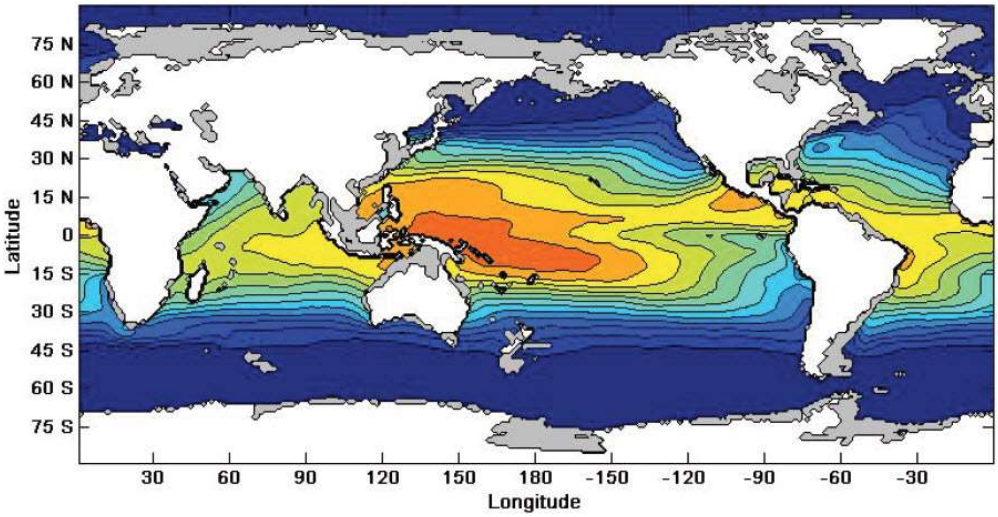

Figure 5. A schematic of the prime OTEC-producing regions.

Shaded from red to yellow, where red represents the region of the ocean where the surface temperature is at least 28 ℃, and each gradation down to yellow represents a 2 ℃ decrease in surface temperature [40]. The blue regions have surface temperatures of 18 ℃ or less, which is anergy, meaning they are incapable of producing work.

Conventional OTEC uses a CWP in blue to bring cold water to service a condenser near the surface per **Figure 6**.

A CWP plant transfers heat irreversibly and supplies entropy at various points in the cycle. As modeled by Nihous, the thermal efficiency of such a cycle is typically half the turbogenerator efficiency of about 85% times the Carnot efficiency, or about 3.4% [41]. The Carnot efficiency is halved because Nihous introduced the concept of a heat ladder, where about a quarter of the surface heat is lost to the evaporator and its pinch point, another quarter is lost to the condenser and its pinch point, and only about half of the heat is converted to work in the turbogenerator.

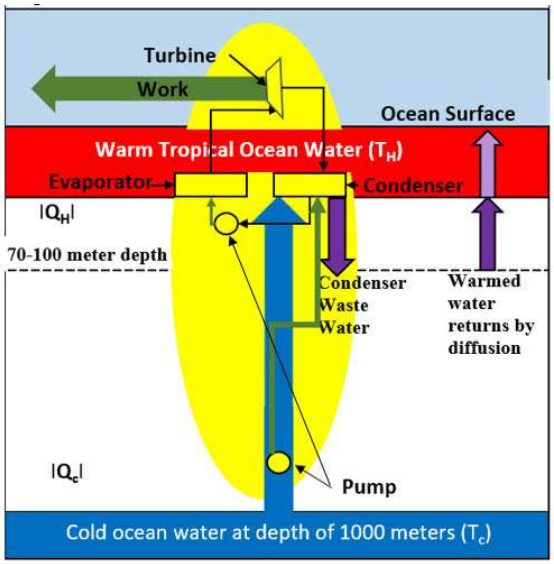

Figure 6. A schematic (not to scale) of conventional OTEC.

Figure 7 shows the functioning of TG, which uses a heat pipe, also referred to as a deep-water condenser or a heat channel, which is the most effective passive method of transferring heat available today [34].

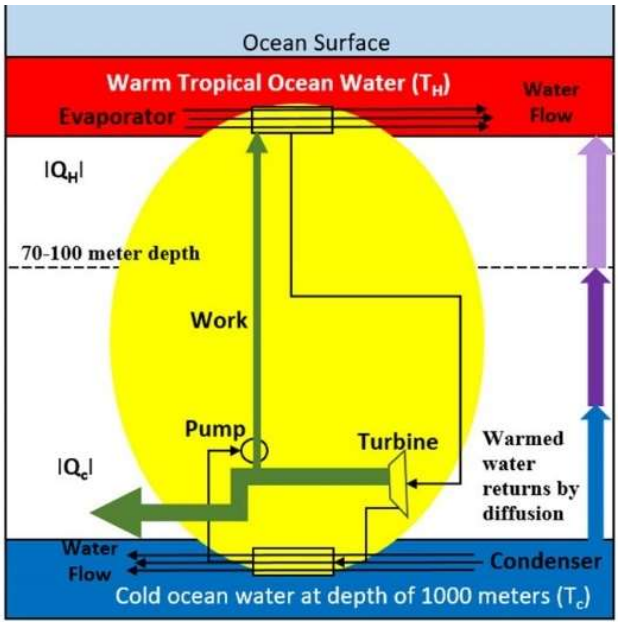

Figure 7. A schematic (not to scale) of the thermodynamics of TG and in yellow is the configuration of its heat engine.

Water passes through an evaporator at the tropical ocean surface to boil a working fluid to supply a vapor that drives a turbine, either at the surface or in deep water, to produce work. A condenser, which is contiguous to the cold-water source at a depth of 1000 m, converts the spent working fluid vapor from the turbine back to a fluid that is then pumped up to the evaporator to complete the work cycle. Wastewater from the condenser returns to the surface by diffusion, where it can be recycled. The work produced by the turbine and the losses incurred by the pumps are indicated in green.

An obvious departure from the design shown in **Figure 6** is the fact that the warm

water remains on the ocean surface and the cold water remains in the deep.

With Nihous' heat ladder, half of the heat of the CWP design is lost to the condenser and the evaporator, which for an OTEC ΔT of 24 would be a loss of 12 ℃. But Melvin Prueitt concluded that with a heat channel (heat pipe), the heat losses through the evaporator and condenser would be limited to 4 ℃, 2 ℃ respectively [34]. Due to the fact that hot surface water is contiguous to the evaporator and cold water is contiguous to the condenser, both can be used to boil the working fluid and to condense the vapor that has passed through the turbine. He also determined that a vertical column of ammonia vapor 1000 m long would warm by 5.3 ℃ as it was compressed by the weight of the vapor above it, increasing its temperature and pressure. As a result, the system efficiency of his design was calculated to be 7.6%, or about 2.5 times the efficiency of conventional OTEC. Other benefits of his and other deep-water condenser OTEC propositions like TG are decreased movements of both warm and cold water, lessened ecological damage when cold water remains in deep water, smaller pipe diameters, and more minor pumping losses with the movement of 2 orders of magnitude less working fluid.

Prueitt assumed that for a heat channel with an inside diameter of 1.128 m (a cross-sectional area of 1 m^2), a vapor velocity of 75 m/s would transfer surface heat into the deep. Whereas the diameter of an equivalent capacity conventional OTEC plant is 10 m, and Rong-Hua Yeh et al. assumed the velocity flow of cold water in CWP of such a plant was about one m/s [42].

CWP heat transfer is achieved through the sensible heat of water compared to the conveyance of the latent heat of a working fluid in a heat pipe. This conveyance is at a speed approaching that of sound owing to the pressure produced by the boiling of the working fluid and then the vacuum produced when the working fluid vapor is condensed by the deepwater heat sink. The size differential (about one order less for the heat pipe) between the two pipe designs results in a 33% cost savings for the heat pipe [43].

OTEC's ΔT, its efficiency, is increasing annually since global warming is primarily a surface effect, and the temperature increase occasioned by global warming in deep water is almost imperceptible.

7. The TG engineering

Paul Curto, former chief technologist with NASA, described OTEC as "by far the most balanced means to face the challenge of global warming. It is also the one that requires the greatest investment to meet its potential. It is a most intriguing answer that can save us from Armageddon" [43].

With recent technical advancements, this investment can be halved. Heat exchangers represent between about 30% and 50% of the total capital cost of an OTEC system [44]. A US Navy report for a brazed aluminum evaporator with fins on the ammonia passage side of 13,905 m^2 of heat transfer area and a titanium shell and tube condenser with twisted tubes and 13,225 m^2 of total heat transfer area are \$561/m^2 and \$770/m^2, respectively [45]. Whereas the TFHX of Makai Ocean Engineering is projected to cost < \$300/m^2, and power can be produced in 1/10th the heat exchanger volume, leading to significantly reduced labor and overhead costs, plus increased

speed of fabrication.

Beyond cost, conventional OTEC is plagued by several issues. First, as **Figure 6** demonstrates, the heat from condenser wastewater is released within the ocean's mixed layer, so it is statistically back at the surface within about three months. Therefore, heat conversion to work provides little climate respite. More importantly, at the energy capacity of TG's potential, OTEC cools the tropical surface to the detriment of an equivalent warming of the poles and the fertile fishing grounds off the west coast of South America, per **Figure 8**.

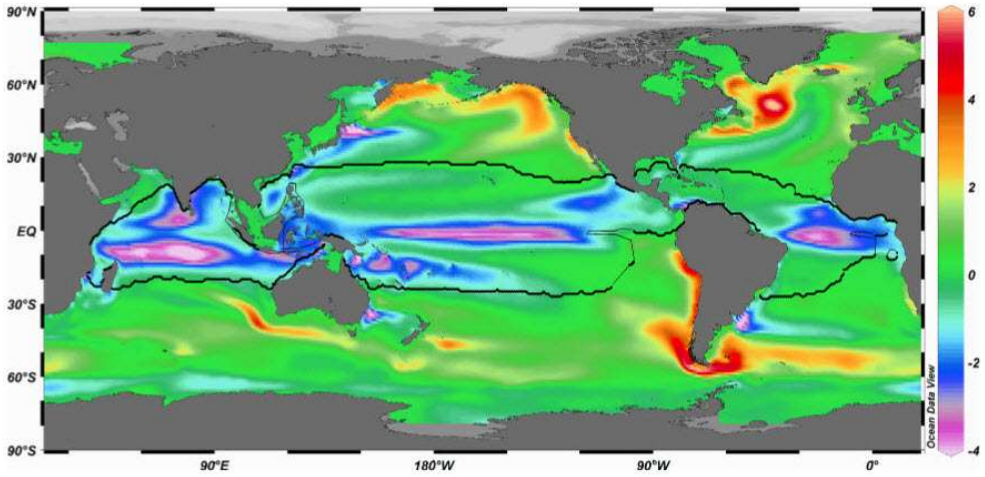

Figure 8. The long-term (1000-year averaged temperature change (°C) in the surface layers (55 m) within the OTEC region outlined by the black line) [31].

The upwelled cold water in **Figure 6** is a dilution of the warm surface, which is only 2.5% of the total ocean volume. To deliver 31 TWyr of power with conventional OTEC, about 62,000,000 m^3/s of cold water would have to be transferred from 1000 m to near the surface, which is 62 Sv. Meanwhile, the thermohaline circulation, the global conveyor belt, which is essential to the rate of sea ice formation near the poles and, in turn, affects other aspects of the climate system, such as albedo, circulates only 15 Sv [46]. The consequence of shifting the volume of water conventional OTEC requires is not only the dilution of the OTEC resource, but upwelled water also pushes surface heat out of the OTEC zone towards the poles, where it becomes both energy and an even more significant environmental hazard, considering surface area declines from the equator poleward. As a result, the Arctic is warming 3 to 4 times faster than at the equator [47]. With conventional OTEC, cold water must be cycled about 3300 times from the depths to the surface over 1000 years. Whereas with TG, heated water would diffuse water from a depth of 1000 m 4.4 times (1000 years/226 years) at a rate of 62,000,000 m^3/(226 years × 365 days × 24 h × 60 min × 60 s)) or about 0.0008 Sv.

The British architect and inventor Dominic Michaelis invented the low-level condenser for OTEC and Energy Island [48]. The latter is a hybrid approach to producing energy from the ocean. His hexagonal platforms were designed to combine wind turbines, solar collectors, wave energy converters, and sea current turbines to produce 250 MW of energy from the water and wind flowing beneath and around the islands.

The 250 MW hexagons are interlockable to scale to higher capacities.

Each hexagon has sides of 291 m, creating a surface area of 220,000 m^2 that is segmented into six equilateral triangles. 19% of the power produced by these hexagons comes from ancillary sources, with the bulk of the energy derived from OTEC (**Table 1**).

Table 1. Energy sources derived from a 250 MW energy island.

Energy source	Megawatts	% of total
Wind	18	7%
Wave	6	2%
Sea current	10	4%
Solar	13.5	5%
OTEC	202.25	81%
Total	250	100%

The islands are stationary, whereas grazing the oceans in search of the highest sea surface temperatures (SST) requires mobility, which is facilitated by a triangular shape, as shown in **Figure 9**, that enables a TG platform to cut through the water. A frontal area is obligatory for collecting the heat of warming, but drag impedes the locomotion needed to locate the highest SSTs. The chevron-shaped leading edge shown in **Figure 9** reduces drag while providing twice the frontal area of the base of the TG triangle.

Legend
1. Command center
2. Spinnakers for downwind motivation
3. Solar panels
4. Wave accumulators (in yellow)
5. Horizontal windmills (blue)
6. Hydrogen tanks
7. Evaporators (not shown beneath solar panels)
8. Heat pipe
9. Return fluid and gas lines

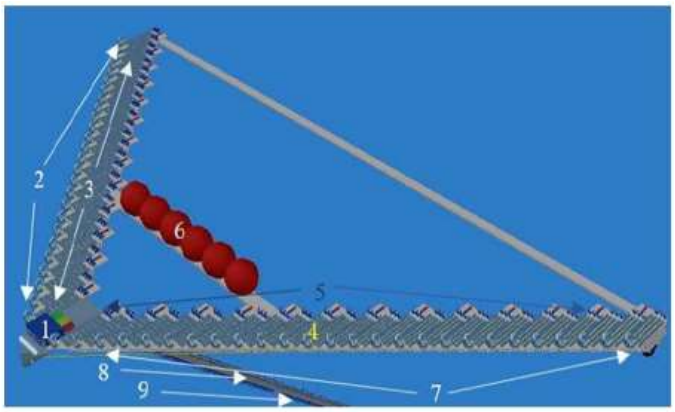

Figure 9. A 1 GW hydrogen-producing TG plant [25].

The real estate behind the leading edge of the TG triangle becomes superfluous unless it can generate more revenue than a void. For example, the National Renewable Energy Laboratory found the total functional wind farm is about 250,000 m^2/MW, and the total land required for 1 MW for generating 200 MW of solar PV power is approximately 4 acres, which is equivalent to 16,000 m^2 [49,50].

An equilateral triangle with sides of 884 m has an area of 338,000 m^3, which, prorated at the ratio of **Table 1**, theoretically could generate 28 MW of wind, 9 MW of wave, and 21 MW of solar power for a total of 58 MW. Whereas a 1 GW TG plant uses only 28,214 m^2 of the ocean's surface and uses 368,082 m^3 of water for its evaporators. With 8.5 m of front and back overhangs of the evaporators, it produces 1 GW, including a combined 5 MW of wind, solar, and wave power from the 42,900 m^2

area of the TG chevron. This is about 70% of the impetus required to move the platform at a speed of about 2 knots as is required to force water through the evaporators and the condensers, which are dragged at 45° below the surface at a depth of 1000 m. The remaining 30% of the propulsive energy can be produced from solar, wind, and wave apparatus situated along the base of the triangle. So, any real estate over and above 42,900 m^2 is precious oceanfront property that is better used for something more productive than producing energy from wind or solar.

If it typically takes 16,000 m^2 to produce 1 MW with PV panels, then TG, at only 42,900 m^2 and 1 GW, is 373 times the solar concentrator of PV panels and is about 5800 times more efficient at using ocean real estate as wind power.

It is estimated that the production of 1 MW of electricity requires four m^3/s of warm water flowing through the evaporators and two m^3/s of cold water flowing through the condensers of an OTEC system [51]. With conventional OTEC, the impetus for this flow is provided by pumps, but for TG heat exchangers, water flow must be provided by the kinetic energy of thrusters situated at each corner of the base of the TG triangle.

The formula for KE is: $KE = 1/2 \times m \times v^2$.

For 1 GW of TG power, 4000 m^3 of water (1000 kg × 4000 m^3) has to flow through the evaporator at a speed of 2 knots (about 1 meter/second), so the requisite KE requirement is 2,000,000 kg × 1 m/s × 1 m/s = 2,000,000 $kg \cdot m^2/s^2$, which is a force of 2,000,000 Joules (J).

Since the condensers need half as much KE flowing through them as the evaporators, the total kinetic energy requirement is 3,000,000 J. Since 1 J is equivalent to 2.7778×10^{-10} MWh, and 3,000,000 J is equivalent to 7.3 MW, then that is the energy requirement (8.33×10^{-4} MWh × 365 days × 24 h) to move a 1 GW plant through the water at a speed of 2 knots. This represents a less than 1% parasitic loss to the TG system and a demonstration of the parsimonious usage of the necessary ocean real estate required to produce 1 GW with a robust, triangular-shaped nautical structure.

This 7.6 MW is the maximum power produced by the ancillary energy sources and is sufficient to move the TG system under its own power from a non-OTEC-producing region into one of the OTEC-producing regions shown in **Figure 3**.

Much of the subsurface TG infrastructure will be filled with working fluid vapor that makes them buoyant, which must be overcome by heavy structures like electrolyzers, generators, ballast, or dive planes that keep the subsurface at the operational depth of 1000 m.

8. Fusion energy

Proponents of fusion energy promote it as energy's Holy Grail [52]. For the purposes of this paper, however, it is a proxy for all exothermic energy sources that are ultimately an impediment to the survival prospects of all living organisms.

Fusion is the source of the Sun's energy and, by extension, is the source of most of the energy found on Earth. It is the combination of lighter atomic nuclei that forms a heavier nucleus, thereby releasing energy. The total mass of the new atom is less than that of the two that formed it, and the "missing" mass is given off as energy, as

described by Albert Einstein in his $E = mc^2$ equation, where "c" is the speed of light. Fusion can be an abundant energy source on Earth because it releases significantly more energy per unit of fuel than fission or chemical reactions. It produces no GHGs during operations and less radioactive waste than fission. The waste products are generally less hazardous and have shorter half-lives than the byproducts of fission. It is inherently safe because if containment of the high temperatures and pressures required to sustain the fusion reaction is breached, the reaction immediately stops.

The primary international effort researching fusion power is ITER, which is a collaboration of 35 countries with contrasting political philosophies that bridge the North/South, otherwise seldom spanned, divide between the developed and developing nations [53]. It is, therefore, an exemplar of how global warming could be tackled, but for the problem of waste heat. It is a large-scale scientific collaboration aimed at demonstrating the feasibility of fusion energy for peaceful purposes and a peaceful demonstration of how the dual problems of emissions and global warming can be addressed.

Fusion energy, however, is a highly exothermic method of producing energy, a thermodynamic dead end, and an accelerant of species extinction. It is confronted by significant technological challenges and complexity, including high initial research, development, and construction costs, a lengthy and uncertain timeline to commercialization, the difficulty in achieving net positive energy gain, and a limited supply of tritium, which every fusion reactor will require on the order of 100 to 200 kg per year. Between a gram and a couple of kilograms of tritium are produced each year in the upper atmosphere when cosmic rays strike nitrogen molecules in the air [53]. A few dozen kilograms are also dissolved in oceans as a result of atmospheric nuclear testing carried out between 1945 and 1980. CANDU-type nuclear reactors, of which 31 are currently in operation, supply about 20 kg of tritium a year [54]. Tritium was produced in large quantities by nuclear weapons programs in the US and Russia, which have been heavily curtailed since 1991, but the half-life of the radioactive isotope tritium is 12.33 years, so this supply is rapidly depleting. ITER has about 15 years of tritium for its deuterium-tritium campaign. However, tritium can be produced (bred) during the fusion reaction through contact with lithium, so its supply could be ensured if the technology's other problems, including waste heat, which confront all exothermic energy sources, could be addressed.

However, the problem of waste heat cannot be wished away. An AI analysis of the efficiency of converting fusion energy into electricity suggests that it is generally lower than that of conventional fission reactors, primarily due to the additional complexities of maintaining and controlling the plasma, which entails efficiency losses of around 30%–50%. Although the Carnot efficiency of a high-temperature fusion reactor is around 40%–50%, the real-world efficiency" is closer to 30%–40%, leaving a combined efficiency of between about 20%–30%. So, at least three times more heat is added to the Earth's system for each TWyr of fusion energy produced.

Thomas Murphy estimates that the waste heat of current energy consumption is about four orders of magnitude smaller than the incident radiation of the Sun, but at a growth factor of ten per century (a modest growth rate of 2.3% per year), waste heat would reach parity with the intensity of the Sun in roughly 400 years [55]. The current EEI associated with climate change is ~1 W m^{-2}, but at a 2.3% energy growth rate, the

waste heat of exothermic energy sources would equal the current EEI in 100 years, after which waste heat would become the dominant forcing.

Like all species, humans will soon be at thermodynamic risk of extinction, deriving our energy from exothermic reactions like fusion.

9. Intermittence

Figure 10 shows the share of Great Britain's electricity derived from fossil fuels between 2009–2024.

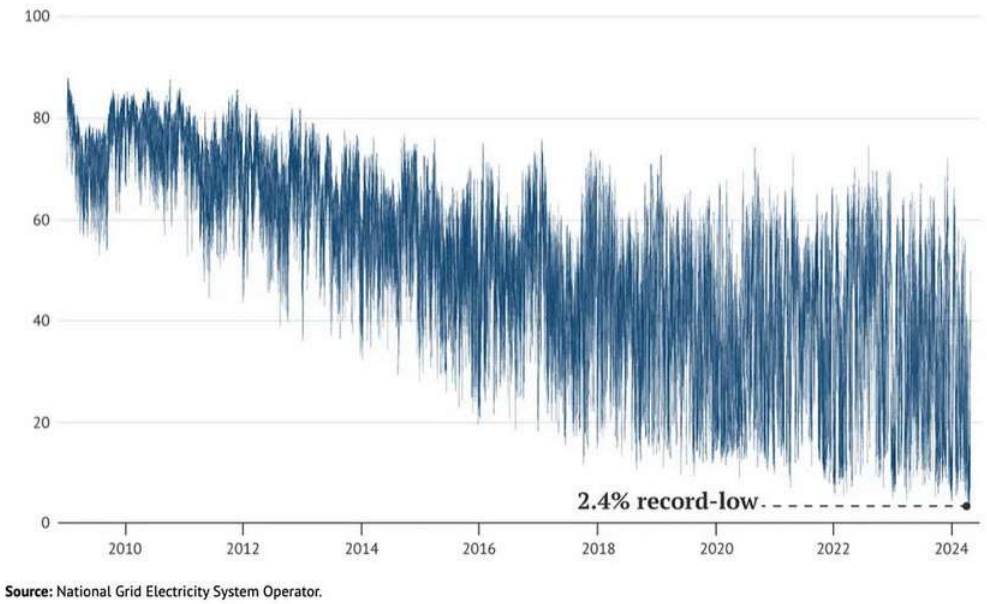

Figure 10. The percentage share of Great Britain's share of electricity derived from fossil fuels in each half-hour period between 2009–2024 [56].

Not only does this graphic show that in April of 2024, the country temporarily derived only 2.4% of its electricity from fossil fuels, it demonstrates that the nation's fossil fuel phase-out has been accompanied by a massive increase in the fluctuation of its energy supply. Ten years ago, these fluctuations were in the range of 20%, but they are now closer to 60%, which is a significant strain on the country's electrical grid. Moreover, Great Britain is not alone in this respect. Europe, South Australia, Texas, and California have similar problems integrating renewables into their grids due to an insufficiency of backup and flexibility of energy sources that can lead to blackouts or brownouts and add costs to grid operators that are then passed on to the consumers of their energy [57–60].

These costs include energy storage, grid management and upgrades, backup generation, curtailment (when excess energy cannot be used or stored), market and regulatory costs, reactive power compensation, and spinning reserve costs that arise due to the fluctuation of weather, time of day, or seasonal variation. Costs that stem from the need to manage the variability and ensure a reliable and stable power grid.

Approximately 40% of global CO_2 emissions are emitted from electricity generation through the combustion of fossil fuels to generate heat to power steam turbines [61]. Replacing fossil fuels with solar and wind generation for the purpose of

producing electricity will require either "overbuilding" (i.e., excess annual generation), the introduction of large-scale energy storage, and/or aggregating resources across multinational regions [62]. So even if we had a better electric sector tomorrow, within decades, emissions would be back to where they are today owing to the emissions associated with the overbuilding and the energy storage infrastructure.

10. Energy and the law of supply and demand

As above, there is no shortage of energy to supply the current 22 TWyr of annual consumption. At least for the next 60 years, as the finite energy sources are consumed. Nevertheless, increasingly existing energy consumption is impacting human civilization and other living organisms.

The law of supply and demand is a fundamental economic principle describing the relationship between the availability of a product (its supply) and the desire for that product (its demand) and the effect of that relationship on price, which in the case of this paper relates to the price of energy. When there is excess supply, prices tend to fall until the surplus is eliminated and equilibrium is reached. Conversely, when there is excess demand, prices rise until the shortage is eliminated and equilibrium is reached.

Global warming is a case of a massive oversupply of energy that can be addressed by reducing the excess energy by converting part of it to work and removing the balance from the surface.

In accordance with the law of supply and demand, the consumption of this excess energy will reduce its cost and everything that relies on its consumption.

11. Resources

One of the weighty obstacles to the fulfillment of maximized sustainable energy consumption is material supply, which is another problem the oceans can address. The Energy Transition Commission estimates that between 2022–2050, an energy transition predicated on a 15-fold increase in wind and a 25-fold increase in solar energy to 15 and 34 TW, respectively (which they perplexingly estimate would be 110,000 TWh—about 1/4th of 49 TW), could require the production of 6.5 billion tonnes of end-use materials, 95% of which would be steel, copper, and aluminum, and smaller quantities of critical minerals/materials like lithium, cobalt, graphite, or rare earths [63]. And would require a significant reliance on recycling, innovation, and efficiency improvements.

There are sufficient resources to meet the current demand for 22 TWyr of energy, but 31 TW, as would be required to change the heat of global warming into work, would impose a 40% greater material burden. Furthermore, 49 TWyr would be 158% more than that.

Recycling can reduce the need for mining of materials, but, as the 6th law of thermodynamics proposes, energy, which is always consumed in recycling, degrades the concentration of materials, the quantity of which is also decreased in each successive step in a series of energy transformations.

Advances in technology and efficiency have been offered as a means of reducing the material intensity of renewable energy systems, but as Heun and Brockway in their

paper “Meeting 2030 primary energy and economic growth goals: Mission impossible?” suggest, energy efficiency is not an effective means of reducing primary energy consumption [64].

IRENA lists the necessary materials for an energy transition as: lithium, cobalt, nickel, graphite, manganese, iron, phosphorus, aluminum, copper, silver, and gold [65]. Although they are not listed in IRENA’s list, magnesium and calcium are the second and third most abundant minerals in the ocean and are ideal for the manufacture of a significant portion of TG infrastructure.

Phosphorous is not found in abundance in the oceans, nor is graphite, except for that which is produced near thermal vents associated with tectonic plate boundaries, and iron and aluminum are less abundant in the ocean than on land, but otherwise the oceans are a cornucopia of minerals and metals that could provide many centuries worth of supply of the materials needed to deliver centuries worth of renewable energy with TG per **Table 2**.

Table 2. Elements etc.

a	b	c	d	e	f	g	h	i	j
Element	**Conc in SW**	**Vol of ocean**	**Ocean**	**Land**	**Yrs supply**	**Mined/yr**	**Yrs land**	**Yrs ocean**	**Multiple**
	(ppm)	**liters**	**MM (tonnes)**	**MM (tonnes)**	**Oceans**	**MM (tonnes)**	**reserves**	**reserves**	**Ocean/Land**
Mg	1290	1.332×10^{21}	1,718,280,000,000	64,541,000,000,000	4,909,371,428.6	0.950	67,937,894,736,842	1,808,715,789,474	0.0266231
Ca	411	1.332×10^{21}	547,452,000,000	114,955,000,000,000	1,564,148,571.4	0.035	3,284,428,571,428,570	15,641,485,714,286	0.0047623
K	392	1.332×10^{21}	522,144,000,000	57,893,000,000,000	1,491,840,000.0	72.000	804,069,444,444	7,252,000,000	0.0090191
Li	0.178	1.332×10^{21}	237,096,000	55,400,000,000	677,417.1	0.106	522,641,509,434	2,236,754,717	0.0042797
Ni	0.0066	1.332×10^{21}	8,791,200	232,680,000,000	25,117.7	2.700	86,177,777,778	3,256,000	0.0000378
Fe	0.034	1.332×10^{21}	45,288,000	155,951,000,000,000	129,394.3	2600.000	59,981,153,846	17,418	0.0000003
Al	0.001	1.332×10^{21}	1,332,000	229,910,000,000,000	3805.7	68.000	3,381,029,411,765	19.58	0.0000000
Cu	0.0009	1.332×10^{21}	1,198,800	166,200,000,000	3425.1	21.000	7,914,285,714	57,086	0.0000072
Mn	0.0004	1.332×10^{21}	532,800	2,631,500,000,000	1522.3	20.000	131,575,000,000	26,640	0.0000002
Co	0.00039	1.332×10^{21}	519,480	69,250,000,000	1484.2	0.170	407,352,941,176	3,055,765	0.0000075
Ag	0.0003	1.332×10^{21}	399,600	20,775,000,000	1141.7	0.026	799,038,461,538	15,369,231	0.0000192
Au	0.000011	1.332×10^{21}	14,652	11,080,000	41.9	0.003	3,574,193,548	4,726,452	0.0013224

(a) Elements, (b) Concentration of elements in seawater (ppm), (c) Volume of the ocean (liters), (d) Concentration of elements in the ocean in million tonnes = b × c/1000/1000000), (e) Land abundance of elements (million tons) = the weight of crust (27 trillion tonnes/1,000,000) × the percentage of the element in the crust, (f) Yrs supply of elements in the ocean (million tons) = d/350 (1-GW TG plant moves 4000 tonnes/sec of water through its heat exchangers, TGs energy potential is 31 TW, and the ocean's mass is 1.4 quintillion short tons of water; therefore 31,000 1-GW plants could move the ocean's total mass through it heat exchangers in about 350 years), (g) Mined each year in million tonnes, (h) Current yearly consumption of elements (tons) = e/g, (i) Yrs ocean reserves = d/g, and (j) Multiple of Ocean/Land = i/h [66–70].

Although **Table 2** indicates there are about 192 times more of the elements in the earth's crust than in the ocean, it is physically impossible to mine and process all the minerals in the crust. Meanwhile, 31,000 TG plants would pass the total volume of the oceans through their heat exchangers in about 350 years. As an example of the recoverability of a vital mineral like copper, the United States Geological Survey estimates there are about 870 million tonnes of recoverable reserves [71]. Whereas **Table 2** shows there are 1,198,800 million tonnes of copper dissolved in the ocean, which is about 1400 times the recoverable reserves of the crust. So, if only 1% of the dissolved copper in the ocean could be recovered, it would still be about ten times more than the recoverable land reserves.

Magnesium hydroxide and calcium carbonate are the main components of Biorock, which could be widely used in the manufacture of TG platforms [72]. These compounds are derived from an electrochemical reaction with seawater in which Mg and/or Ca are crystallized at a cathode. Under low electrical current conditions, extremely hard calcium carbonate limestone deposits, made up of crystals of the mineral aragonite, are formed, and higher currents cause the growth of the mineral brucite, or magnesium hydroxide, which is soft.

On a steel, aluminum, or titanium frame, calcium carbonate accretes at a rate of between 1–2 cm per year and has a load-bearing strength about three times ordinary Portland cement. Magnesium hydroxide is soft and flaky and accretes at a similar rate with little load-bearing strength, but it can be cast in molds to form bricks, blocks, or other shapes. However, magnesium hydroxide is readily converted into magnesium carbonate cement by absorbing CO_2, and this cement is even harder than calcium carbonate. Whereas conventional cement manufacturing combusts limestone to make quicklime and releases CO_2 into the atmosphere and is a primary global source of greenhouse gas, biorock cements can be produced on a large scale with energy produced from the conversion of the heat of global warming to work. And these are harder than contemporary cements and reduce global warming by removing CO_2 from the atmosphere and the oceans.

The price of resources is inexorably rising, as are surface temperatures due to fossil fuel burning, and with every degree of warming, the risk of species extinction increases, and massive environmental damage is being done. Humans and other species are migrating to forestall these outcomes, and society is absorbing the environmental costs, all of which can be mitigated with the resources available in the oceans.

The Office of Energy Efficiency & Renewable Energy of the US Department of Energy lists the various methods whereby dissolved seawater minerals and metals can be mined and produced [73].

The heat of global warming is 15 times the energy necessary for a total energy transition that would mitigate every consequence of climate change at 1/6th of the existing cost of energy, which is a rebuttal to the argument that the decoupling of global GDP from resource use is a physical impossibility on a finite planet [25].

12. Energy carriers

Trade in ocean-based goods and services represents about 3% of the global GDP

[74]. To service the other 97%, ocean-derived energy must be conveyed to the land [73].

OTEC converts heat to work, which is initially converted to electricity. Most proposed conventional OTEC operations will be on stationary platforms from which electricity could be conveyed worldwide through an HVDC grid. According to the European Commission, HVDC transmission losses are less than 3% per 1000 km, which is 30 to 40% less than alternating current lines at the same voltage [75]. A 1000-square-kilometer grid of the planet could service every site on the planet.

However, experimental and emerging technologies can also convey power without wires through microwave or laser transmission. These eliminate the need to locate physical infrastructure in remote or difficult-to-access areas and have been offered for space-based solar power applications. As with HVDC transmission, however, converting electricity to microwaves and laser beams and back again involves energy losses, and microwaves and lasers pose safety risks to living organisms.

TG plants cannot be tethered to a grid because they need to be mobile in order to seek out the highest SSTs, so an energy carrier is required. However, producing goods on ocean-going green fields by the conversion of raw materials using ocean-derived electricity or providing services on these green fields is a unique way of energy carrying that TG can provide. As is the recycling of worn-out goods and materials into new materials on ocean-going green fields using ocean-derived electricity.

To reduce the dependence on fossil fuels, particularly in the transportation sector, for electricity generation, heating, or cooling, a more conventional energy carrier is required.

As the use of fossil fuels declines and is replaced with energy supplies from non-fossil sources, the world could eventually become oversaturated with electricity and deficient in chemical fuels [76]. Hydrogen is the most elemental chemical and can be derived by the electrolysis of seawater. As the DOE has pointed out, HPE can contribute to the enabling and acceptance of technologies where H_2 is the energy carrier [77]. TG electrolyzers would operate at a depth of 1000 m where the pressure is 100 bar. HPE requires pressures of 120–200 bar at 70 ℃, whereas the temperature at 1000 is 4 ℃. These temperatures and pressures are conducive to HPE and would eliminate the need for external compression that would otherwise consume about 3% of the energy required for HPE. H_2 produced at 1000 m arrives at the surface 70% of the way, logarithmically, to the 700-bar pressure needed for transportation applications.

Green or renewable H_2 is indispensable to climate neutrality [78]. In theory, it can store excess renewable energy generated during periods of low demand, which can then be converted back into electricity when needed for decarbonizing sectors that are difficult to electrify, such as long-distance transportation and heavy industries like steel and cement production. H_2 can serve as a zero-carbon feedstock in the production of chemicals and synthetic fuels, replacing fossil fuels in the processes.

Ammonia is another energy carrier offered as a chemical replacement for fossil fuels, but ammonia production requires an H_2 precursor plus a costly additional manufacturing step. And the Haber-Bosch process, which accounts for more than 90% of the world's ammonia production, accounts for 1.4% of global carbon dioxide

emissions and consumes 1% of the world's total energy production [79].

Magnesium and calcium, as shown in **Table 2**, are plentiful in the oceans and have massive energy-carrying potential. Magnesium hydride has a high energy density and can store H_2 that can be released as needed. It is a candidate for H_2 storage in renewable energy systems. Magnesium-ion batteries are being researched as a potential alternative to lithium-ion batteries due to magnesium's abundance, safety, and energy density [80]. These batteries use magnesium as the anode and oxygen from the air as the cathode. They have high theoretical energy densities and are being explored for long-term energy storage and electric vehicles.

Magnesium in a high-oxygen environment can be combusted to produce heat, light, electricity, and magnesium oxide that can be recycled back into magnesium, forming a closed system loop.

Calcium can also serve as an energy carrier in the context of calcium-ion batteries and other chemical energy storage systems. Calcium-ion batteries are also being researched as an alternative to lithium-ion batteries given their potential to offer high voltage and energy density [81]. Calcium hydride reacts with water to produce H_2 gas that can then be used as a fuel or stored for later use. Calcium can also be used in thermochemical energy storage processes, where it undergoes reversible chemical reactions to store and release energy. For example, calcium oxide reacts with water to form calcium hydroxide while releasing heat that can be used for various applications, such as power generation. Calcium-based systems are generally considered safe and non-toxic, and calcium-based compounds can offer high energy densities, making them efficient for storing and transporting energy.

The development of magnesium and calcium-based energies and their storage are in their early stages of development and face significant challenges, but in view of the abundance of these metals in the ocean, such development is worth pursuing, considering the vital role energy carriers can provide, conveying ocean-derived energy to land-based consumers.

13. Conclusions

As reviewed, TG presents a large, continuous, renewable energy resource that can contribute to the reduction of global warming by converting a portion of that heat to work and relocating the balance into deepwater from where it will return and can be recycled. Energy is vital to all living organisms, but beyond the human species' need for energy is an economic imperative. Both of which are melded into a proposed 7th Law of Thermodynamics that combines the MPP with the Law of Supply and Demand completing the suite of thermodynamic laws. Thereby unifying them into a general solution to one of humanity's greatest concerns. Over 90% of the heat of warming is going into the oceans, which is a reasonably recoverable reserve that can be recovered under current technological and economic conditions. OTEC is the technology whereby this reserve can be harvested. It is the embodiment of ocean thermal dams that converts the stratified heat of the tropical surface into work in accordance with the second law of thermodynamics. TG is the improvement that increases conventional OTEC's thermodynamic efficiency, thereby allowing it to produce about two and a half times more energy. It is a dissection of the global heat

engine into manageable tranches. And is an endothermic resource that derives heat from its environment, thereby negating the thermodynamic consequence of waste heat while reducing the cost of energy production and of everything that relies on energy inputs. The oceans contain a wealth of dissolved minerals and metals that can supply a renewable energy transition and produce energy carriers that can convey ocean-derived power to land-based consumers. TG "is a true triple threat against global warming. It is the only technology that acts to reduce the temperature of the ocean directly, eliminates carbon emissions, and increases carbon dioxide absorption while generating portable and efficient fuel. It can create millions of jobs and is a serious contender for the future multi-trillion-dollar energy economy. It is baseload negative emission technology that would yield the lowest social costs and should be prioritized for investment." [43] It is the maximum utilization of the ocean's stored thermal energy and can maximize the utilization of its mineral resources. Whereas artificial intelligence is being offered as a tool for fighting climate change by predicting weather, tracking icebergs, and identifying pollution, OTEC is anthropogenic intelligence that can ensure the survival of our species with direct climate cooling and the intelligent use of the ocean's resources and is the only near-term option available for limiting global warming and moderating its devastating consequences [28].

Acknowledgments: The author acknowledges and salutes the two anonymous reviewers whose input helped to improve this paper and the OTEC pioneers who preceded the author in the field.

Conflict of interest: The author declares no conflict of interest.

Nomenclature

CO_2	carbon dioxide
CWP	cold-water pipe
EEI	Earth's energy imbalance
PE	gravitational potential
GHGs	greenhouse gases
GDP	Gross domestic product
HPE	high-pressure electrolysis
HVDC	high-voltage direct current
H_2	Hydrogen gas
ITER	International Thermonuclear Experimental Reactor
kcal	kilocalories
kgf-m	kilogram-force meter
KE	kinetic energy
m	mass in kilograms
MPP	maximum power principle
MEER	Mirrors for Earth's Energy Rebalancing
OTEC	ocean thermal energy conversion
O_2	Oxygen gas
Sv	Sverdrup - unit of volumetric flow rate equal to 1 million cubic meters per second

$Twyr_{30}$	terawatts-years in the 30-year time frame considered for renewables and consumption
Twyr	terawatts -years
TG	thermodynamic geoengineering
TFHX	thin film heat exchangers
GESAMP	UN's Joint Group of Experts on the Scientific Aspects of Marine Environmental Protection
UNFCCC	United Nations Framework Convention on Climate Change
DOE	US Department of Energy
v	velocity in meters/sec
W/m^2	watts per meter squared

References

1. Tilley DR. Howard T. Odum's contribution to the laws of energy. Ecological Modelling. 2004; 178(1-2): 121-125. doi: 10.1016/j.ecolmodel.2003.12.032
2. Odum HT. Scales of Ecological Engineering. Ecological Engineering. 1996; 6 (1–3): 7–19.
3. Demirmen F. Reserves Estimation: The Challenge for the Industry. Journal of Petroleum Technology. 2007; 59(05): 80-89. doi: 10.2118/103434-jpt
4. Perez M, Perez R. Update 2022—A fundamental look at supply side energy reserves for the planet. Solar Energy Advances. 2022; 2: 100014. doi: 10.1016/j.seja.2022.100014
5. von Schuckmann K, Minière A, Gues F, et al. Heat stored in the Earth system 1960–2020: where does the energy go? Earth System Science Data. 2023; 15(4): 1675-1709. doi: 10.5194/essd-15-1675-2023
6. Forster PM, Smith C, Walsh T, et al. Indicators of Global Climate Change 2023: annual update of key indicators of the state of the climate system and human influence. Earth System Science Data. 2024; 16(6): 2625-2658. doi: 10.5194/essd-16-2625-2024
7. Loeb NG, Johnson GC, Thorsen TJ, et al. Satellite and Ocean Data Reveal Marked Increase in Earth's Heating Rate. Geophysical Research Letters. 2021; 48(13). doi: 10.1029/2021gl093047
8. Rate and impact of climate change surges dramatically in 2011-2020. Available online: https://wmo.int/news/media-centre/rate-and-impact-of-climate-change-surges-dramatically-2011-2020 (accessed on 16 April 2024).
9. von Schuckmann K, Cheng L, Palmer MD, et al. Heat stored in the Earth system: where does the energy go? Earth System Science Data. 2020; 12(3): 2013-2041. doi: 10.5194/essd-12-2013-2020
10. Forman C, Muritala IK, Pardemann R, et al. Estimating the global waste heat potential. Renewable and Sustainable Energy Reviews. 2016; 57: 1568-1579. doi: 10.1016/j.rser.2015.12.192
11. Haider Q. Nuclear Fusion: Holy Grail of Energy. In: Nuclear Fusion—One Noble Goal and a Variety of Scientific and Technological Challenges. IntechOpen; 2019. doi: 10.5772/intechopen.82335
12. About the secretariat. Available online: https://unfccc.int/about-us/about-the-secretariat#:~:text=The%20ultimate%20objective%20of%20all,naturally%20and%20enables%20sustainable%20development (accessed on 16 April 2024).
13. Status of Ratification of the Convention. Available online: https://unfccc.int/process-and-meetings/the-convention/status-of-ratification-of-the-convention (accessed on 16 April 2024).
14. Carbon Dioxide and Climate. National Academies Press; 1979. doi: 10.17226/12181
15. Marechal K, Lazaric N. Overcoming inertia: insights from evolutionary economics into improved energy and climate policies. Climate Policy. 2010; 10(1): 103-119. doi: 10.3763/cpol.2008.0601
16. Hajer MA, Pelzer P. 2050—An Energetic Odyssey: Understanding 'Techniques of Futuring' in the transition towards renewable energy. Energy Research & Social Science. 2018; 44: 222-231. doi: 10.1016/j.erss.2018.01.013
17. Lelieveld J, Haines A, Burnett R, et al. Air pollution deaths attributable to fossil fuels: observational and modelling study. BMJ. Published online November 29, 2023: e077784. doi: 10.1136/bmj-2023-077784
18. Renewable Energy to Support Energy Security. Available online: https://www.nrel.gov/docs/fy20osti/74617.pdf (accessed on 16 April 2024).
19. World Energy Transitions Outlook 2023. Available online: https://www.irena.org/Digital-Report/World-Energy-Transitions-

Outlook-2023 (accessed on 16 April 2024).
20. Holden E, Linnerud K, Banister D. The Imperatives of Sustainable Development. Sustainable Development. 2016; 25(3): 213-226. doi: 10.1002/sd.1647
21. GESAMP. High level review of a wide range of proposed marine geoengineering techniques. Available online: http://www.gesamp.org/site/assets/files/1723/rs98e.pdf (accessed on 16 April 2024).
22. Hoffert MI, Caldeira K, Benford G, et al. Advanced Technology Paths to Global Climate Stability: Energy for a Greenhouse Planet. Science. 2002; 298(5595): 981-987. doi: 10.1126/science.1072357
23. Smalley RE. Future Global Energy Prosperity: The Terawatt Challenge. MRS Bulletin. 2005; 30(6): 412-417. doi: 10.1557/mrs2005.124
24. Nihous GC. An Order-of-Magnitude Estimate of Ocean Thermal Energy Conversion Resources. Journal of Energy Resources Technology. 2005; 127(4): 328-333. doi: 10.1115/1.1949624
25. Baird J. Global warming, a global energy resource. Thermal Science and Engineering. 2024; 6(2): 5268. doi: 10.24294/tse.v6i2.5268
26. Jia Y, Nihous G, Rajagopalan K. An Evaluation of the Large-Scale Implementation of Ocean Thermal Energy Conversion (OTEC) Using an Ocean General Circulation Model with Low-Complexity Atmospheric Feedback Effects. Journal of Marine Science and Engineering. 2018; 6(1): 12. doi: 10.3390/jmse6010012
27. Kwiatkowski L, Ricke KL, Caldeira K. Atmospheric consequences of disruption of the ocean thermocline. Environmental Research Letters. 2015; 10(3): 034016. doi: 10.1088/1748-9326/10/3/034016
28. Baiman R, Clarke S, Elsworth C, et al. Addressing the Urgent Need for Direct Climate Cooling: Rationale and Options. Oxford Open Climate Change. Published online August 12, 2024. doi: 10.1093/oxfclm/kgae014
29. Rau GH, Baird JR. Negative-CO_2-emissions ocean thermal energy conversion. Renewable and Sustainable Energy Reviews. 2018; 95: 265-272. doi: 10.1016/j.rser.2018.07.027
30. Baird J. Thermodynamic Geoengineering: The Solution to Global Warming! Available online: https://www.amazon.ca/Thermodynamic-Geoengineering-solution-global-warming/dp/1777079608 (accessed on 16 April 2024).
31. Rajagopalan K, Nihous GC. An Assessment of Global Ocean Thermal Energy Conversion Resources with a High-Resolution Ocean General Circulation Model. Journal of Energy Resources Technology. 2013; 135(4). doi: 10.1115/1.4023868
32. Hausfather Z. Factcheck: Why the recent 'acceleration' in global warming is what scientists expect. Available online: https://www.carbonbrief.org/factcheck-why-the-recent-acceleration-in-global-warming-is-what-scientists-expect/ (accessed on 16 April 2024).
33. Hansen JE, Sato M, Simons L, et al. Global warming in the pipeline. Oxford Open Climate Change. 2023; 3(1). doi: 10.1093/oxfclm/kgad008
34. Prueitt ML. Heat Transfer for Ocean Thermal Energy Conversion; US 200702893 03A1, 20 December 2007.
35. Liang X, Spall M, Wunsch C. Global Ocean Vertical Velocity from a Dynamically Consistent Ocean State Estimate. Journal of Geophysical Research: Oceans. 2017; 122(10): 8208-8224. doi: 10.1002/2017jc012985
36. UCSUSA. Ten Signs of Global Warming. Available online: https://www.ucsusa.org/resources/ten-signs-global-warming (accessed on 16 April 2024).
37. Cheng L, Zhu J, Abraham J, et al. 2018 Continues Record Global Ocean Warming. Advances in Atmospheric Sciences. 2019; 36(3): 249-252. doi: 10.1007/s00376-019-8276-x
38. Resplandy L, Keeling RF, Eddebbar Y, et al. Quantification of ocean heat uptake from changes in atmospheric O_2 and CO_2 composition. Scientific Reports. 2019; 9(1). doi: 10.1038/s41598-019-56490-z
39. December 1840: Joule's Abstract on Converting Mechanical Power Into Heat. Available online: https://www.aps.org/publications/apsnews/200912/physicshistory.cfm (accessed on 16 April 2024).
40. An Evaluation of the U.S. Department of Energy's Marine and Hydrokinetic Resource Assessments. National Academies Press; 2013. doi: 10.17226/18278
41. Nihous GC. A Preliminary Assessment of Ocean Thermal Energy Conversion Resources. Journal of Energy Resources Technology. 2006; 129(1): 10-17. doi: 10.1115/1.2424965
42. Yeh RH, Su TZ, Yang MS. Maximum output of an OTEC power plant. Ocean Engineering. 2005; 32(5-6): 685-700. doi: 10.1016/j.oceaneng.2004.08.011
43. Curto P. American Energy Policy V—Ocean Thermal Energy Conversion. Available online:

https://www.opednews.com/populum/page.php?p=1&f=American-Energy-Policy-V--by-Paul-from-Potomac-101214-315.html (accessed on 16 April 2024).
44. Dhanak MR, Xiros NI. Springer Handbook of Ocean Engineering. Springer International Publishing; 2016. doi: 10.1007/978-3-319-16649-0
45. Rocheleau R. Ocean Thermal Energy Conversion (OTEC) Heat Exchanger Development. Available online: https://www.hnei.hawaii.edu/wp-content/uploads/OTEC-Heat-Exchanger-Development-2018-2020.pdf (accessed on 16 April 2024).
46. Toggweiler JR, Key RM. Thermohaline Circulation. In: Encyclopedia of Ocean Sciences. Academic Press; 2001. pp. 2941-2947. doi: 10.1006/rwos.2001.0111
47. Rantanen M, Karpechko AYu, Lipponen A, et al. The Arctic has warmed nearly four times faster than the globe since 1979. Communications Earth & Environment. 2022; 3(1). doi: 10.1038/s43247-022-00498-3
48. Michaelis D. Energy Island. In: Proceedings of the Oceans 2003. Celebrating the Past ... Teaming Toward the Future (IEEE Cat. No.03CH37492); 22-26 September 2003; San Diego, CA, USA. pp. 2294-2302. doi: 10.1109/OCEANS.2003.178267
49. Denholm P, Hand M, Jackson M, et al. Land Use Requirements of Modern Wind Power Plants in the United States. Office of Scientific and Technical Information (OSTI); 2009. doi: 10.2172/964608
50. Imhan N. Area Required for Solar PV Power Plants - Suncyclopedia. Available online: http://www.suncyclopedia.com/en/area-required-for-solar-pv-power-plants/ (accessed on 16 April 2024).
51. Herrera J, Sierra S, Ibeas A. Ocean Thermal Energy Conversion and Other Uses of Deep Sea Water: A Review. Journal of Marine Science and Engineering. 2021; 9(4): 356. doi: 10.3390/jmse9040356
52. Sanderson C. The 80 trillion-watt shot: “Holy Grail” fusion energy pioneer claims record at world’s most powerful machine. Available online: https://www.rechargenews.com/energy-transition/the-80-trillion-watt-shot-holy-grail-fusion-energy-pioneer-claims-record-at-world-s-most-powerful-machine/2-1-1609341 (accessed on 16 April 2024).
53. What is ITER? Available online: http://www.iter.org/proj/inafewlines (accessed on 16 April 2024).
54. Arnoux R. Tritium: Changing lead into gold. Available online: http://www.iter.org/mag/8/56 (accessed on 16 April 2024).
55. Murphy TW. Energy and Human Ambitions on a Finite Planet. eScholarship, University of California; 2021. doi: 10.21221/S2978-0-578-86717-5
56. Staff CB. Analysis: Fossil fuels fall to record-low 2.4% of British electricity. Available online: https://www.carbonbrief.org/analysis-fossil-fuels-fall-to-record-low-2-4-of-british-electricity/ (accessed on 16 April 2024).
57. Verzijlbergh RA, De Vries LJ, Dijkema GPJ, et al. Institutional challenges caused by the integration of renewable energy sources in the European electricity sector. Renewable and Sustainable Energy Reviews. 2017; 75: 660-667. doi: 10.1016/j.rser.2016.11.039
58. Abdullah MA, Agalgaonkar AP, Muttaqi KM. Climate change mitigation with integration of renewable energy resources in the electricity grid of New South Wales, Australia. Renewable Energy. 2014; 66: 305-313. doi: 10.1016/j.renene.2013.12.014
59. Hao C. Texas Power Company Warns of Catastrophic Failure if Storage Issues Go Unresolved. Available online: https://www.governing.com/infrastructure/texas-power-company-warns-of-catastrophic-failure-if-storage-issues-go-unresolved (accessed on 16 April 2024).
60. California Power Outage Map. Available online: https://www.bloomenergy.com/bloom-energy-outage-map/ (accessed on 16 April 2024).
61. Abdallah L, El-Shennawy T. Reducing Carbon Dioxide Emissions from Electricity Sector Using Smart Electric Grid Applications. Journal of Engineering. 2013; 2013: 1-8. doi: 10.1155/2013/845051
62. Tong D, Farnham DJ, Duan L, et al. Geophysical constraints on the reliability of solar and wind power worldwide. Nature Communications. 2021; 12(1). doi: 10.1038/s41467-021-26355-z
63. Materials and Resource Requirements for the Energy Transition. Available online: https://www.energy-transitions.org/wp-content/uploads/2023/08/ETC-Materials-Report_highres-1.pdf (accessed on 16 April 2024).
64. Heun MK, Brockway PE. Meeting 2030 primary energy and economic growth goals: Mission impossible? Applied Energy. 2019; 251: 112697. doi: 10.1016/j.apenergy.2019.01.255
65. Gielen D, Papa C. Materials for the Energy Transition. Available online: https://en.wikipedia.org/wiki/Abundance_of_elements_in_Earth%27s_crust (accessed on 16 April 2024).
66. Concentrations and estimated amounts of dissolved metal ions in the sea, compared with the estimated land resources.

Available online: https://www.researchgate.net/figure/Concentrations-and-estimated-amounts-of-dissolved-metal-ions-in-the-sea-compared-with_tbl1_43336400 (accessed on 16 April 2024).
67. Bhutada G. All the Metals We Mined in 2021: Visualized. Available online: https://www.visualcapitalist.com/all-the-metals-we-mined-in-2021-visualized/ (accessed on 16 April 2024).
68. How many liters of water are there in the ocean? Available online: https://www.quora.com/How-many-liters-of-water-are-there-in-the-ocean (accessed on 16 April 2024).
69. What is the total mass of the Earth's crust? Available online: https://www.quora.com/What-is-the-total-mass-of-the-Earths-crust (accessed on 16 April 2024).
70. Abundance of Elements in Earth's Crust. Available online: https://en.wikipedia.org/wiki/Abundance_of_elements_in_Earth%27s_crust (accessed on 16 April 2024).
71. International Copper Association. Copper Demand and Long-Term Availability. Available online: https://internationalcopper.org/sustainable-copper/about-copper/cu-demand-long-term-availability/ (accessed on 16 April 2024).
72. Goreau TJ. Marine Electrolysis for Building Materials and Environmental Restoration. In: Electrolysis. Intechopen; 2012. doi: 10.5772/48783
73. U. S. Department of Energy. Powering the Blue Economy: Exploring Opportunities for Marine Renewable Energy in Maritime Markets. Available online: https://www.energy.gov/sites/prod/files/2019/03/f61/73355.pdf (accessed on 16 April 2024).
74. United Nations. 5 global actions needed to build a sustainable ocean economy. Available online: https://unctad.org/news/5-global-actions-needed-build-sustainable-ocean-economy (accessed on 16 April 2024).
75. Ardelean M, Minnebo P. HVDC Submarine Power Cables in the World. Available online: https://op.europa.eu/en/publication-detail/-/publication/78682e63-9fd2-11e5-8781-01aa75ed71a1/language-en (accessed on 16 April 2024).
76. Nikolaidis P. Sustainable routes for renewable energy carriers in modern energy systems. Bioenergy research: commercial opportunities & challenges. 2021. doi: 10.1007/978-981-16-1190-2_8
77. U.S. Department of Energy Hydrogen Program Plan. Available online: https://www.hydrogen.energy.gov/docs/hydrogenprogramlibraries/pdfs/hydrogen-program-plan-2020.pdf?Status=Master (accessed on 16 April 2024)
78. van Renssen S. The hydrogen solution? Nature Climate Change. 2020; 10(9): 799-801. doi: 10.1038/s41558-020-0891-0
79. Ammonia: Zero-Carbon Fertiliser, Fuel and Energy Store. Available online: https://royalsociety.org/-/media/policy/projects/green-ammonia/green-ammonia-policy-briefing.pdf (accessed on 16 April 2024).
80. Huie MM, Bock DC, Takeuchi ES, et al. Cathode materials for magnesium and magnesium-ion based batteries. Coordination Chemistry Reviews. 2015; 287: 15-27. doi: 10.1016/j.ccr.2014.11.005
81. Gummow RJ, Vamvounis G, Kannan MB, et al. Calcium-Ion Batteries: Current State-of-the-Art and Future Perspectives. Advanced Materials. 2018; 30(39). doi: 10.1002/adma.201801702

Thermal Science and Engineering 2024, 7(2), 5268.
https://doi.org/10.24294/tse.v7i2.5268

Review

Global warming, a global energy resource

Jim Baird

Thermodynamic Geoengineering, 3217 Jingle Pot Road, Nanaimo, BC, V9R 7C6, Canada; jim.baird@gwmitigation.com

CITATION

Baird J. Global warming, a global energy resource. Thermal Science and Engineering. 2024; 7(2): 5268. https://doi.org/10.24294/tse.v7i2.5268

ARTICLE INFO

Received: 18 March 2024
Accepted: 7 April 2024
Available online: 23 April 2024

Abstract: Global warming is a thermodynamic problem. When excess heat is added to the climate system, the land warms more quickly than the oceans due to the land's reduced heat capacity. The oceans have a greater heat capacity because of their higher specific heat and the heat mixing in the upper layer of the ocean. Thermodynamic Geoengineering (TG) is a global cooling method that, when deployed at scale, would generate 1.6 times the world's current supply of primary energy and remove carbon dioxide (CO_2) from the atmosphere. The cooling would mirror the ostensible 2008–2013 global warming hiatus. At scale, 31,000 1-gigawatt (GW) ocean thermal energy conversion (OTEC) plants are estimated to be able to: a) displace about 0.8 watts per square meter (W/m^2) of average global surface heat from the surface of the ocean to deep water that could be recycled in 226-year cycles, b) produce 31 terawatts (TW) (relative to 2019 global use of 19.2 TW); c) absorb about 4.3 Gt CO_2 per year from the atmosphere by cooling the surface. The estimated cost of these plants is $2.1 trillion per year, or 30 years to ramp up to 31,000 plants, which are replaced as needed thereafter. For example, the cost of world oil consumption in 2019 was $2.3 trillion for 11.6 TW. The cost of the energy generated is estimated at $0.008/KWh.

Keywords: global warming; energy types; conversion of heat to work; heat engine; waste heat; ocean thermal stratification; carbon dioxide offgassing from the ocean to the atmosphere

1. Introduction

Energy and climate change are inextricably linked [1]. From the first principle, the heat of global warming is an energy source like any other that can be converted from one form to another. As with all heat it always flows spontaneously from a warm reservoir to a colder one and when transferred through a heat engine, it produces work and waste heat.

The heat of global warming represents about 7% of the hemispherically antisymmetric poleward heat transport that in the northern hemisphere peaks at about 5.5 petawatts [2,3].

Since the mean solar input is 340 W/m^2, and relative to the pre-industrial benchmark the atmosphere has absorbed an extra 0.8 W/m^2 due to warming, the heat of global warming represents about 0.2% of the total solar input [2,4].

Ocean heat uptake is an essential measure of the Earth's climate. About 90% of the heat from global warming has gone into the oceans, which are becoming increasingly thermally stratified with lighter waters near the surface [5,6]. This configuration acts as a barrier to the efficient mixing of heat, carbon, oxygen, and nutrients vital to aquatic life. However, the efficient mixing of these ingredients would eliminate all risks of climate change and have the potential to produce over twice the energy currently derived from fossil fuels.

The thermally stratified ocean lends itself to the conversion of a portion of the heat of global warming to work in accordance with the First and Second Laws of

Thermodynamics. However, a thermally stratified ocean resists the movement of surface heat into deep water due to buoyancy.

To induce vertical movement through a heat engine, heat pipes, which are highly effective thermal conductors that transfer heat through the latent heat of boiling and condensation of a low-boiling-point working fluid, are required.

Water is at its greatest density at a temperature of 4 ℃ and is universally found at an ocean depth of about 1000 m.

Heat directed through a heat engine to produce work would be a deletion of heat from the ocean because this work is undertaken on the land or at least at the ocean's surface.

In this study, the author advances the proposition; that the Laws of Thermodynamics are the only appropriate signpost for coherent climate policy.

2. The global heat engine as an archetype for anthropogenic heat engines

The oceans, constantly in motion, are the Earth's natural heat engine [7]. Although tides and waves are the obvious manifestations of this motion, the unseen bulk of this movement is driven by the push of dense brine sinking to the seafloor as surface water freezes at the poles each winter, and the spontaneous pull of warmed tropical waters seeking the poles in accordance the Second Law of Thermodynamics. This heat engine, known as the thermohaline circulation, is also known as "the global conveyor belt."

2.1. The ocean/atmosphere interface

The ocean and atmosphere are closely related dynamically. Energy transfers from the atmosphere to the mixed layer of the ocean, which drives upper ocean circulation [8]. In turn, there is a feedback of energy from the ocean back to the atmosphere that affects atmospheric circulation, the weather, and the climate.

In general, the ocean/atmospheric heat flux is due to differences in pressure. High pressures produce winds that distribute heat to low-pressure areas around the Earth's surface. And the Coriolis effect influences the east/west flow of the Trade Winds.

2.2. The heat source for the global heat engine

As shown in **Figure 1**, heat accumulates in the low latitudes and dissipates in the higher latitudes. In heat surplus, the low latitudes accumulate as much as 80 W/m^2. Whereas the high latitudes are in heat deficit as the heat accumulated in the tropics dissipates to space or is consumed as the latent heat of the fusion of melting ice. The net effect is 0.8 W/m^2 of global warming [2]. And since the Earth's surface is 510 million square kilometers (510 trillion square meters), the heat of warming was on average 408 TW between the years 1995 to 2016 [9].

In 2023, ocean temperatures reached a record high of 15 ± 10 Zeta Joules (ZJ), which converts to 476 TW [10]. Which represents a 17% increase in warming over 20 years. Whereas the Mauna Loa Volcano CO_2 record for the same period shows only a 12% rise in atmospheric CO_2 content. Making it clear that global warming is more than just emissions [11,12].

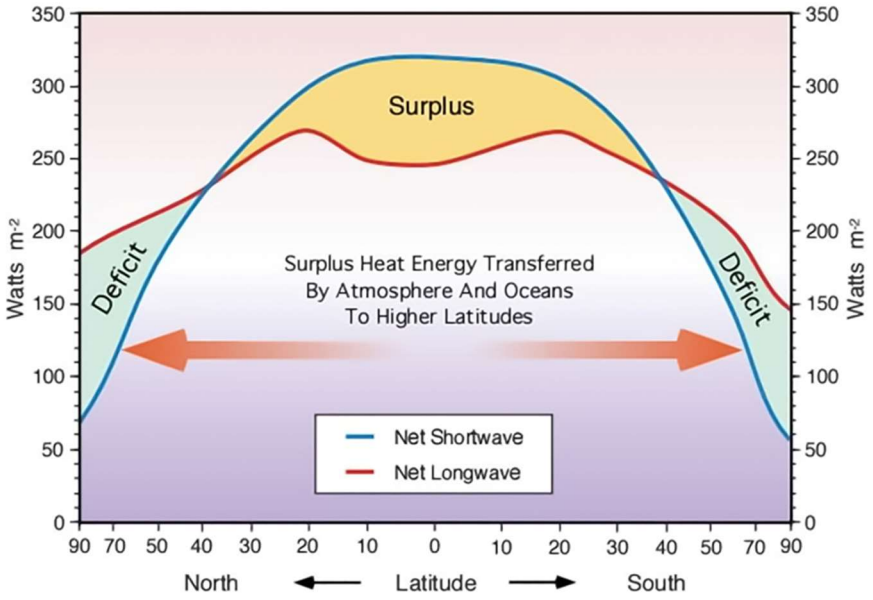

Figure 1. Heat energy transfer from surplus to deficit [13].

2.3. The heat sink for the global heat engine

The heat capacity of seawater is 3850 Joules per kilogram (J/kg) per degree Kelvin. The average seawater density is about 1027 kg/m^3 and since the volume of the ocean is 1.34 × 10^{18} cubic meters, and the mass of the ocean is 1.38 × 10^{21} kg, times 3850 J/kg, equates to an energy content of 5.3 × 10^{24} Joules/K [14].

Cooling the atmosphere by 2 ℃, starting from 2050, when cooling could reasonably commence after a 25-year period of research and development, and returning to preindustrial temperatures in an equal length of time as it took for the heat to build up, and since the average depth of the ocean is about 3682 m, and the atmospheric cooling would come at the expense of ocean warming, the total ocean would need to warm by about 0.0005 ℃ [15].

3. The global warming resource

Global warming is a use-it-or-lose-it proposition. About 89% of the heat of warming has accumulated in the world's oceans, but it won't stay there [16].

The oceans are stratified in three layers: a surface, mixed layer that contains about 50 million km^3 of water, a middle "thermocline" that contains about 460 million km^3 of water, and the deep oceans, which contain about 890 million km^3 of water [17]. The temperature differential between the top few meters of the tropical mixed layer, which can reach as high as 38 ℃, and the 4 ℃ of the bottom of the thermocline is the largest, potential, dispatchable source of renewable energy.

Utilizing data from the renewable energy map scenario, Hassan et al. found that renewable energy sources could command up to two-thirds of the global primary energy supply by 2050 [18].

3.1. Dispatchable sources of energy

Per **Table 1**, less than 1 megawatt of the most abundant sources of dispatchable energy, TG and OTEC, are being exploited.

Table 1. The annual potential of dispatchable energies [19,20].

Technology	Annual potential in terawatts
Thermodynamic geoengineering	31
Ocean thermal energy conversion	3–11
Hydro	3–4
Biomass	2–6
Geothermal	0.3–2
Waves	0.2–2
Tidal	0.3

The thermohaline circulation, with a cycle length of between 1600 to 2000 years, ensures that sequestered ocean heat will ultimately resurface. Unless it is converted to work and the waste heat of those conversions is dissipated to space. A task that would be enhanced by the depletion of the greenhouse blanket by the production of hundreds of years of negative emissions of energy.

3.2. Heat source

Resplandy et al. produced a whole ocean thermometer based on the estimated ocean heat content, the main source of thermal inertia in the climate system, as measured by increased atmospheric oxygen (O_2) and CO_2 levels resulting from the release of these gases as the surface warms [2].

The study showed, between 1991–2016, a mean date of 2004, the ocean gained $1.29 \pm 0.79 \times 10^{22}$ J of heat per year (409 TW). Equivalent to a planetary energy imbalance of 0.80 ± 0.49 W/m^2 of the Earth's surface.

While the latest estimate of ocean heat is 476 TW [11].

3.3. Heat sink

Per **Figure 2**, the combined heat transport of the atmosphere and the ocean peaks at about 5.5 petawatts in the Northern Hemisphere and about 4.5 petawatts in the Southern Hemisphere [3]. This poleward movement of heat is the path of least resistance for heat generated in the tropics. In the Northern Hemisphere, 78% of this movement is through the atmosphere, and in the Southern Hemisphere, it is 92%, with the balance circulating through the oceans [21].

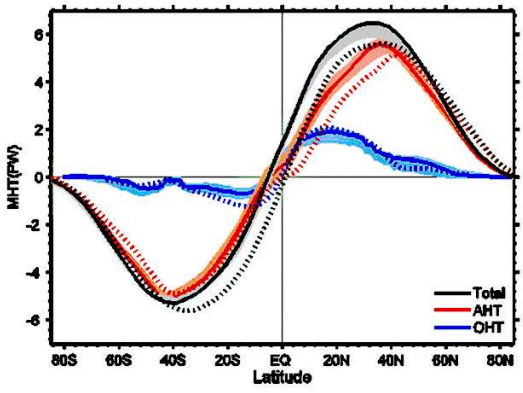

Figure 2. The heat transport of energy through the atmosphere and ocean [3].

The stored heat in the ocean will ultimately be released but at a much slower rate than it accumulates [22].

An alternative path for the heat of global warming

Figure 3 proposes an alternative route for tropical heat to reach a cold water heat sink.

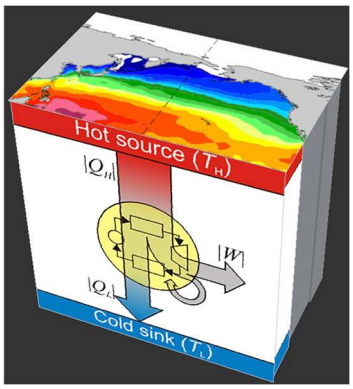

Figure 3. Surface heat transport into deep water [23].

The heat can be sent into deep water through a heat engine with the aid of a heat pipe [24]. Which is a countercurrent heat flow to the thermohaline that would extend the cycle life of the global conveyor belt and double the length of time it takes for heat sequestered in the ocean to resurface. Years that would be characterized by an absence of the ravages of global warming.

The diffusion rate of heat from deep water to the surface is 1 cm/day below the mixed layer (4 m a year) and 1 m/day through that layer. Thus, it takes about 226 years for heat released at a depth of 1000 m to regain the surface [25]. At this time, the heat unconverted to work can be recycled, 12 more times. Effectively doubling the number of years of climate respite, and the effectiveness of the oceans' heat sink.

Heat sequestered in the ocean is fungible because it represents only about 7% of the annual poleward migration of heat from the tropics to the poles.

3.4. The consequences of moving heat from the atmosphere into the ocean

The heat capacity of the ocean is about three orders greater than that of the atmosphere. The top 2.5 m of the ocean holds as much heat as the entire atmosphere [26]. Levitus et al. estimated the oceans warmed 0.09 °C between the depths of 0–2000 m during the period 1955–2010 [27]. And proposed that if all that heat was transferred to the lower 10 km of the global atmosphere, it would be warmed by 36 °C.

An analysis of the NOAA chart of ocean heat contact between 1960–2023 shows that from 1983 to the present, the midpoint of the Levitus study, to 2023, the amount of heat stored in the upper 2000 m of the global ocean more than doubled the 1955–2010 average [4]. The potential and inevitable heat transfer to the lower atmosphere is therefore at least 72 °C in a Business-As-Usual scenario where no effort is made to reduce emissions or cool the surface.

Accumulating ocean heat content is contributing to sea level rise, ocean heat waves, coral bleaching, melting of polar ice sheets and Greenland, Antarctic, and

Himalayan glaciers, wildfires, droughts, more severe storms, loss of species, greater health risk, reduced food supplies, poverty and displacement, and runaway heat that will make some areas too hot for human habitation [28].

Cooling the surface, as TG would provide, would mitigate these risks.

4. Carnot efficiency

Carnot efficiency is the maximum efficiency a heat engine can attain operating between two temperatures. Improving energy efficiency is regarded as a key path to tackling global warming and achieving the UN's Sustainable Development Goals (SDGs) [29].

For OTEC, ideally, the sea surface temperature (SST) is 30 ℃ and the deep water heat sink is 4 ℃ so, with this ΔT the theoretical efficiency is about 9%.

Nihous, however, introduced the concept of a heat ladder for OTEC, in which only half the available heat produces work in the OTEC turbine, 1/16th each is lost at the evaporator and condenser pinch points, and 3/8th each is lost in the evaporators and condensers [30].

OTEC parasitic pumping losses are influenced by power capacity, pipe type, cold water discharge, and cold water depth, but they are typically assessed at between 20% to 30%. Therefore, in ideal conditions, OTEC has a thermodynamic efficiency of about 3.6%.

Melvin Prueitt, a Los Alamos Labs theoretical physicist, however, devised a system that uses a deepwater condenser and heat pipe (he called a heat channel), and calculated the efficiency of his system, using ammonia as the working fluid, at 7.6% [31]. This was for a surface temperature of 27.5 ℃ rather than the 30 ℃ TG can attain due to its ability to seek out the ocean's highest SSTs.

This considerable improvement over conventional OTEC was produced by cutting the losses through the heat evaporators and condensers by half by using hot and cold water contiguous to the heat exchangers, rather than pumping cold water from a depth of 1000 to service condensers at or near the surface. But the biggest difference was the 5.3 ℃ temperature gain of the boiled working fluid vapor under the gravitational influence of a 1000 m long column of gas situated vertically in the ocean.

Prueitt calculated the parasitic pumping loss of his system at only 10% [31].

Manikowski proposed CO_2 OTEC with an estimated 7% system loss compared to an ammonia working fluid, offset by a 2% pumping gain due to the proximity of the density of the gas in its gaseous and liquid states [32].

The operating temperature of a CO_2 OTEC system would approach the critical point of CO_2, 31 ℃, and the 73.8 bar pressure, in the evaporator. Which would be exceeded at a depth of 1000 m due to the gravitational influence. However, since half of the heat of the system is lost through a turbine, a gas-to-liquid phase would occur within the turbine, which would tear up the equipment.

It would therefore be necessary to operate a CO_2 OTEC system below its critical temperature and pressure. Nevertheless, subcritical CO_2, turbines would be smaller, more efficient, and less costly than typical Rankine Cycle turbines of similar capacity. And CO_2 would be a more environmentally friendly working fluid than ammonia.

5. Exergy efficiency

The conventional wisdom is that OTEC is an irreversible system. Its exergy efficiency is defined as the ratio of the thermal efficiency of the system compared to the idealized Carnot efficiency. But with TG, 7.6% of the heat of warming is converted to work, and 92.4% of the heat, which, under normal circumstances would be considered waste heat, becomes a new input for another heat engine in 226 years. As soon as the original heat returns to the surface. This process is repeated 12 more times until all the heat of warming has been converted to work and the waste heat of those conversions has dissipated into space. Since it is estimated that somewhere between 20% to 50% of energy inputs are lost as waste heat in the form of exhaust gases, cooling water, and heat lost from hot equipment surfaces and heated products, only between 6 and 16 TW of the current warming of 476 TW would ever become true waste heat [11,33]. This makes TG, at between 96.6% to 98.7% efficient, the closest thing to a reversible process as can be found in nature.

6. Waste heat

Many engineers consider the heat of warming to be waste heat in view of the low efficiency of OTEC, which is the only technology that attempts to harness the diffuse heat of warming [1]. They have more experience with and are more comfortable working with energy inputs with efficiencies in the 50% to 80% range and at high temperatures.

They equate thermal efficiency with capital efficiency, but the waste heat of nuclear power is higher than that of coal or other fossil fuel-fired plants [34].

Waste heat can be used to heat homes and industry during winters, but in summer, heatwaves in 2003, 2006, 2015, and 2018 forced the shutdown of or curtailment of the output of nuclear plants. And escalating global warming can only exacerbate the waste heat problem [35,36].

Fusion produces temperatures of about 100 million degrees Kelvin and is considered energy's holy grail [37]. Its efficiency in energy storage and auxiliary heater modes is between 85.07% and 89.1%, respectively [38]. When used to produce hydrogen (H_2), its efficiency increases to 94.15% and 92.05% in the same modes. Which is still less than TG.

In Energy and Human Ambitions on a Finite Planet, Thomas Murphy reasoned that at the historical rate of energy growth since 1650, the Earth will come up against the severe thermodynamic limit of a boiling ocean in 400 years [39]. The only way to prevent this calamitous outcome, while providing the energy modern society needs, is to exclusively use endothermic processes, unlike fission or fusion, that absorb heat from the environment.

7. TG—Anthropogenic heat engines utilizing the global warming resource

The oceans are the only place in the climate system that stores heat. They do this principally at the surface. Between 1971–2018, of the 89% of the heat of warming that went into the ocean, 52% went into the upper 700 m, 28% to a depth of 700–2000 m,

and 9% below 2000 m [16]. As **Figure 4** shows, in 2023, the ocean's surface warmed about 8 times more than the temperature increase at a depth of 1000 m.

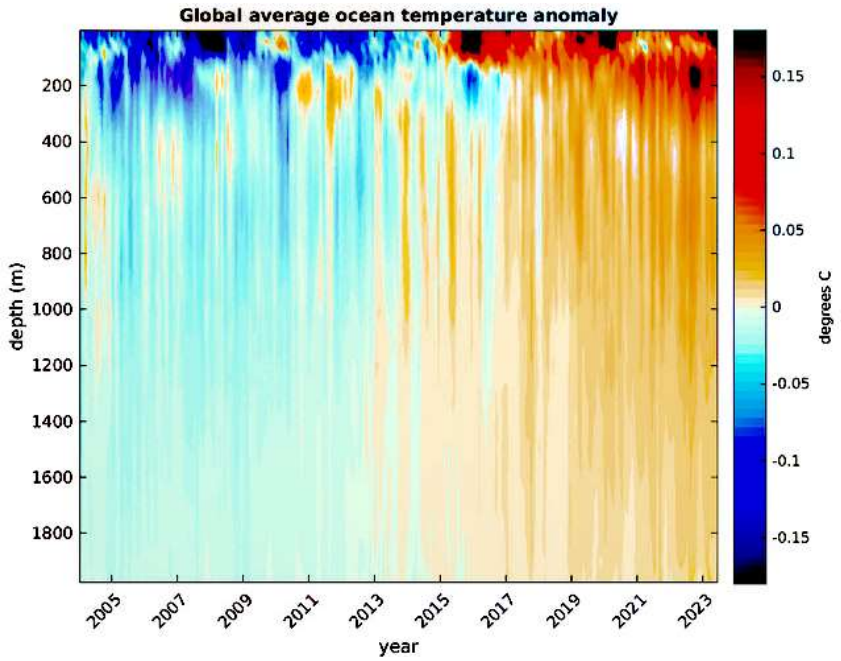

Figure 4. Ocean heat anomaly 2014–2023, 0 to 2000 meters [26].

The closer to the surface, the warmer the water, and since surface heat is problematic, the rational option is to try to relocate the heat of warming as far from the surface as possible, within reason. The thermocline is the layer beneath the ocean's mixed layer where the surface cools rapidly from a temperature of about 13 ℃ to 4 ℃ at a depth of 1000 m. After which, the rate of cooling declines very slowly. Therefore, intentionally moving heat below 1000 m is counterproductive. The efficacy of removing heat from the surface is enhanced by the fact that shifting the heat through a heat engine produces energy. And even more so, when this energy can be produced at less than the cost of burning fossil fuels. And even more so when this energy cools the surface and reverses the offgassing of CO_2 from the oceans to the atmosphere. And in fact, with cooling, this offgassing is reversed, and about 4.3 gigatons (Gt) of atmospheric CO_2 moves back into the ocean each year at no cost.

TG is the only productive way the heat of warming can be eliminated from the ocean/atmosphere system. This is an outcome that would be enhanced in an environment where no more emissions are created, and legacy emissions are dissipated to space over the course of about three thousand years.

Warming heat is significantly impacting the climate. But, in the alternative, it could be the catalyst for the fulfillment of the UN's 17 SDGs [29].

Solar energy has the potential to produce 23,000 TW of power and wind 25–70 TW annually, but they are not dispatchable sources of power [20]. They are intermittent, requiring expensive energy storage systems that in turn require metals that are both difficult and ecologically fraught to unearth.

Every square meter of the Earth's surface is impacted by waves, wind, ocean currents, and solar energy, a portion of which can be converted to electrical energy or an energy carrier like H_2 using photocatalytic and photoelectrochemical technologies

[40].

The British architect and inventor, Dominic Michaelis, devised the concept of an Energy Island, which is a hybrid approach utilizing each of the above sources to produce energy from the oceans [41]. The design was for a hexagonal platform where wind turbines, solar collectors, wave energy converters, and sea current turbines combine to produce 250 MW of energy from the water and wind flowing beneath and around the island.

Each hexagon has equal sides of 291 m, creating a surface area of 220,000 m^2. The hexagon is segmented into six equilateral triangles. Nineteen percent of the power derived from these hexagons would come from ancillary sources, with the bulk of the energy derived from OTEC per **Table 2**.

Table 2. Various energies derived from a 250 MW energy island [41].

Energy source	Megawatts	% of Total
Wind	18	7%
Wave	6	2%
Sea current	10	4%
Solar	13.5	5%
OTEC	202.25	81%
Total	250	100%

The hexagons are interlockable to facilitate scaling to greater capacities.

The islands are stationary, which is problematic because of the seasonal nature of the OTEC resource. For example, in September, in the Gulf of Mexico, the SST is consistently in the range of 30 ℃, which is ideal for OTEC (the ΔT between the surface and 1000 m where the temperature is 4 ℃ must be at least 20 degrees to produce power) [42]. In March, however, the average temperature of the Gulf is 18 ℃, leaving a ΔT of 14 ℃ which is anergy.

Another problem with the Energy Island concept is that it uses 81% of its ocean real estate to produce only 19% of its power, per **Table 2**. Furthermore, heat released in a condenser within the mixed layer of the ocean is statistically back at the surface within about 3 months; therefore, no climate respite is provided [25]. But even more importantly, at the energy capacity of TG's potential, conventional OTEC cools the tropical surface to the detriment of an equivalent warming of the poles and the fertile fishing grounds off the west coast of South America [43].

TG platforms are designed to be mobile, and capable of seeking out the highest SSTs that become inputs for heat engines that convert the heat to work.

The frontal area is obligatory for harvesting SSTs, but drag is an impediment to forward motion. To reduce drag, TG platforms use a chevron shape to cut through the surface, which in turn provides twice the frontal area along the leading edges of the chevron as the base, which provides rigidity to the equilateral triangle that comprises the upper section of the system.

Whereas the Energy Island produces 250 MW of power using 220,000 m^2 of ocean surface, a 1-GW TG platform would produce the same amount of power using only 42,900 m^2 of ocean real estate.

The frontal area of the chevron is angled top to bottom at 45 degrees to allow for the sloughing off of aquatic life too big to pass through the system's heat exchangers.

Above the submerged evaporators, surface overhangs of 8.5 m, front and back, incorporate wave accumulators and photovoltaic panels, spinnakers used for when the platform is moving downwind on the Trade Winds, and horizontal windmills for going upwind. All of these are incorporated into a 50 m-long surface platform from which 5 MW of ancillary power is produced to provide the impetus necessary to drive the system forward and force water through the system's heat exchangers.

The stripped-down version of an Energy Island embodied by TG provides considerable labor and material savings over the original Energy Island, or any other hybrid OTEC system.

The National Renewable Energy Laboratory estimates the total useful wind farm requires about 250,000 m^2 per megawatt [44]. And the total requirement for 1 megawatt of solar photovoltaics (PV) is 4 acres, or about 16,000 m^2 [45]. Whereas, TG's 42,900 m^2 produces 1 GW of power and provides 373 times the solar concentration of PV. This is consistent with the fact that PV is a surface effect, while TG evaporators are thirteen meters deep and boil 6.5 m worth of working fluid to produce the vapor that produces the power in the system's turbine.

PV panel's power productivity, conversion efficiency, and energy cost are affected by environmental factors such as dust, hail, humidity, and temperature and installation element parameters such as inclination angle, installation area, and altitude [46]. None of which are at play beneath the surface. Where the bottom of the evaporator contains 6.5 m of working fluid yet to be boiled.

To produce 1-GW with a TG system, 66 evaporators, 13 m wide by 34 m long by 13 m deep, are required.

The First Generation 50 MW OTEC Plantship design of Michaelis and Vega, incorporated 5–18 MW evaporators with 13 × 34 × 13 m dimensions and an equal number of condensers of the same size in its design [47]. This ship, however, situated its condensers at the surface, which required large cold water pipes to bring cold water from the depths to service the condensers. Whereas the TG design uses heat pipes that are 1/10th the size and are 2.5 times more efficient.

To produce 1-GW with the Michaelis/Vega design, one hundred evaporators and condensers would be required. So, for the TG design, either smaller heater exchangers or fewer of them are required, and the latter design consideration was selected due to a concern about the width of the platforms.

The wider they are, the more difficult they are to maneuver.

The minimum economically viable size for OTEC plants is estimated to be 100 megawatts, and each doubling of this capacity reduces the overall capital cost of larger systems by 22% [48,49].

Figures 5 and **6** are conceptual renderings by the author of 1-GW TG plants in an H_2 production configuration, **Figure 5**, and a greenfield format, **Figure 6**, where electricity is produced at sea.

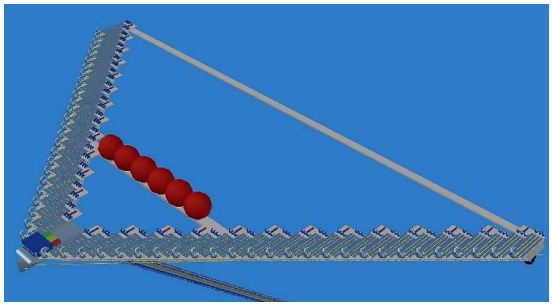

Figure 5. A 1 GW TG hydrogen-production plant.

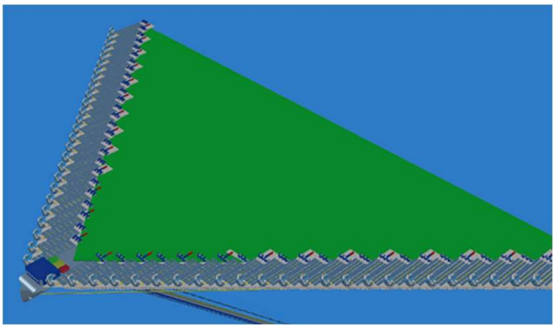

Figure 6. A 1 GW TG electricity production plant with greenfield.

Nobel Laureate Richard Smalley, in his "Terawatt challenge" found that energy was the answer to mankind's next nine concerns, including, water, food, environment, poverty, terrorism and war, disease, education, democracy, and population [50].

The 1-GW chevron would have wings, each side, 429 m long with a 26 m wide hull at the pinnacle of the triangle, making a greenfield of 84,595 m^2, which is 39% of the area of an Energy Island that produces a quarter of the energy.

On TG's green fields, steel, aluminum, cement, and fertilizer plants, which are the hardest industries to decarbonize, could flourish. As could artificial intelligence and data mining operations. Metal and mineral extraction from seawater could be undertaken, amongst a myriad of other opportunities requiring electricity. All in the service of cooling the surface and restoring the environment.

Unlike cryptocurrencies, which some liken to "fool's gold", the oceans contain 47 real minerals and metals, including gold and silver, some of which are already being harvested [51].

TG platforms, harvesting surface heat by passing millions of tonnes of water through their heat exchangers, could be adapted to extract a portion of the 47 quadrillion tons of trace elements that are dissolved in solution (Each liter of seawater contains about 35 g of dissolved salts) [52].

The combined ocean volume is roughly 1.335 sextillion liters of water [53].

Thirty-one thousand 1-GW TG plants, moving 124,000,000 tonnes/sec through their heat exchangers, could move the equivalent of 1.4 quintillion short tons of water (the ocean's total mass) in about 350 years.

Electrical production with TG would be 25% cheaper than H_2 production due to the cost of electrolysers and storage infrastructure. But Green Hydrogen could play a significant role in achieving low and net-zero emissions [54].

Artificial intelligence (AI) technology could contribute to the solution of the

energy production problem by using AI for the analysis and prediction of energy production data [55].

Global warming is more energy than can be consumed in a single tranche; therefore, low thermal efficiency makes no difference to the amount of work that can be produced with global warming's copious amount of energy.

An energy carrier like H_2 would be better suited to the conveyance of ocean-derived power to terrestrial consumers than electricity, which can be hazardous in its own right, as evidenced by the California forest fires triggered by the electrical grid [56].

Heat source

The mean date of the Resplandy paper was 2004, and the mean warming was 409 TW [2].

A joint NASA and NOAA study found the Earth's energy imbalance doubled over the 14-year period from 2005 to 2019 [57]. This was prior to the International Maritime Organization's introduction of limits on the amount of Sulphur in fuel oil for ships, in 2020 [58]. James Hansen et al. estimated an increase in global absorbed solar radiation by 30% over the prior 5-year average [59]. It is assumed therefore it is likely the ocean heat content will be at least 3 times greater than it was in 2004, about 3300 TW, in 2046, which is likely the earliest TG platforms could start reversing the global warming sign.

Although it is beyond the scope of this paper, and since warming has been ongoing for at least 270 years and the TG cycle is 226 years, the 409 TW average of 2004 seems like a reasonable annual objective for reducing the surface heat over the course of 226 years. After which the heat of warming would be depleted by recycling captured ocean heat between the depths of 1000 m and the surface.

8. The climate benefit of anthropogenic heat engines

Richard Smalley's "terawatt challenge" was "To give all 10 billion people on the planet the level of energy prosperity we in the developed world are used to, a couple of kilowatt-hours per person, we would need to generate 60 TW around the planet—the equivalent of 900 million barrels of oil per day" [50]. But this goal runs up against the thermodynamic limit identified by Tom Murphy, whereby the historical growth rate of consumption would demand the total output of the sun used here on Earth in 1000 years [39].

The compromise is endothermic and baseload energy. As **Table 1** demonstrates, TG has three times the capacity of its closest contender and over one order of magnitude more than the rest.

As Smalley ranked them, energy, water, food, and the environment will be the greatest drivers of climate migration [60].

Heat can reasonably be seen as a proxy for the environment and H_2 as a proxy for water. The latter is an energy carrier, unlike electricity, which has a single function, and in a fuel cell H_2 combines with O_2 to produce electrical energy and water, the source of life on the planet, in a process that thermodynamically is the mirror image of electrolysis.

H_2 produced at sea level would have an average hydrological head of 840 m on land, over four times the hydraulic head of the Hoover Dam with a head of 180 m, when combined with O_2 in a fuel cell to produce energy and water [61].

Another proxy for the environment is "sea level rise", especially in conjunction with storm surges, which many see as the greatest risk of warming. Along with saltwater intrusions that destroy fresh groundwater supplies [62].

In the global ocean, the thermal expansion coefficient (TEC) varies from 0.3×10^{-4} °C^{-1} near the freezing temperature (≤0 °C) to 3.5×10^{-4} °C^{-1} in tropical waters [63]. At a depth of 1000 m, it is about half as deep as the tropical surface. Heat moved to a median depth of 500 m with TG heat pipes, which would therefore produce 25% less thermal expansion of the seawater. But more importantly, it would be unavailable to melt ice sheets or glaciers, which currently account for about 21% of the recorded sea level rise of the past two decades [64]. But it could induce 60 m of sea level in the foreseeable future [65].

9. The entropy of carbon dioxide removal from the atmosphere

IPCC AR6 WGIII says, CDR is required to achieve global and national targets of net zero CO_2 and greenhouse gas emissions [66]. One part per million (ppm) equals 2.1 gigatons of carbon (GtC) or 7.8 gigatons of carbon dioxide ($GtCO_2$). But ~55% of emissions are absorbed by oceans or the land, so 1 ppm of emissions or reduction equals 17.3 $GtCO_2$ [67]. To go from 11 March 2024, an atmospheric CO_2 concentration of 425 ppm to 280 ppm (the estimated preindustrial level) would require the removal of 2509 $GtCO_2$ plus future emissions [68]. At a removal rate of 40 $GtCO_2$/year net, this would take 63 years. With Negative-CO_2-emissions ocean thermal energy conversion (NEOTEC), 1 gigawatt of electricity production would avoid 1.1×10^6 tonnes of CO_2 emissions/year and consume and store (as dissolved mineral bicarbonate) approximately 5×10^6 tonnes CO_2/year [19].

Thirty-one thousand 1-GW TG plants, as is TG's potential, would therefore sequester 155 Gt of CO_2 in the ocean in one year. The estimated cost per tonne of this sequestration would be $154/tonne so, the total annual cost would be $24 trillion [69]. And the 2509 $GtCO_2$ removal required to return the atmosphere to the preindustrial CO_2 level, would be met in about 16 years. At a total cost of $384 trillion.

And to further complicate matters, the working life of TG plants is about 31 years, so they would sequester about 4900 $GtCO_2$ over their working life at a sequestration cost of about $744 trillion, or equivalent to the global GDP of the next 7.5 years.

Since the atmosphere alone holds about 3276 Gt CO_2 the TG plants would need to start pulling CO_2 out of the ocean.

Beyond the economic incongruity of CDR, its thermodynamics do not add up. The atmosphere holds about 890 GtC compared to 38,000 GtC in the upper, deep, and sedimentary layers of the ocean [70]. If the atmosphere were to become devoid of carbon on account of CDR, entropy would soon ensure that ocean carbon would fill the atmospheric void.

In short, entropy would seek to spread the carbon beyond the oceans.

CarbonBrief estimates that as much as a quarter of global energy will need to be dedicated to CDR by 2100, which has implications for waste heat, as was examined

above [71].

The Black Body temperature of the planet is −23 ℃, whereas the actual temperature is 15 ℃. The difference is the greenhouse gas (GHG) blanket. If 25% of the energy produced by TG was used for CDR, there would soon be no CO_2 in the atmosphere with the result the surface would soon reach the Black Body temperature. Plus, the 2 ℃ TG removed to the ocean, times 4, for the Stefan-Boltzmann constant, would leave an average surface temperature of −15 ℃. Which would make for an equally unhabitable planet as global warming is beginning to make the existing one.

10. The economics of anthropogenic heat engines

TG is a nascent renewable energy technology with a theoretical potential of 31 TW, but this potential is indefinite considering there are no operating commercial plants. And there are knowledge gaps that need addressing.

10.1. Spatial boundaries

OTEC runs on the same fuel as a tropical cyclone. Ocean surface temperatures of 26.5 ℃ or greater are required to produce a storm. A total of 88 named storms occurred across the globe in 2022, which was near the 1991–2020 average [72]. A single storm can produce as much as 600 TW of energy, at least 20% more than the heat of global warming, so there is no spatial boundary [73]. But for the Small Island Developing States (SIDS), which control 30% of the economic exclusion zones that comprise the prime OTEC areas. But the SIDS doesn't have sufficient electrical demand to justify the cost of OTEC, which demands plants of at least 100 MW capacity to be commercially viable [74].

The other 70% of the ocean are global commons over which no country, technology, or individual will ever hold sway.

10.2. Natural, location-specific influences on the real net power output

In the Atlantic SSTs of 30 ℃ off the top end of South America and in the Gulf of Mexico are common in September as they are in the Eastern Pacific and Indian Ocean temperatures at that time of year.

March is the peak of the typhoon season in the southern hemisphere, where 30 ℃ temperatures are still common in the Pacific and Indian Oceans, but south of where those temperatures are reached in September.

In the off-peak storm season between the latitudes 20 degrees north and 20 degrees south latitudes temperatures of 24 ℃ are common and are at the lower limit for TG energy production.

A ΔT of 6 ℃ between the surface and 1000 m would make a 24% difference in the output of a TG plant.

10.3. Capital cost

TG systems are an arrangement, in order of cost, of a platform and hull, heat exchangers, turbines, electrolysers (if H_2 is to be produced), pumps, a heat pipe, and an interface between the platform, the pipe, and the condensers and/or the electrolysers situated in deep water.

Large heat exchangers are a function of low thermodynamic efficiency and are linearly scalable in accordance with the requisite power.

Table 3 shows the cost of TG plants based on the literature, where:

1) The 10 MW plant is land based.
2) All other plants have a floating ship design.
3) The cost of the 100 MW plant is 66 percent of the base cost of the conventional 100-MW plant of $4000/kW [75].
4) Each doubling of the size of plants 100 MW or greater lowers plant costs by 22% [76].
5) An inflation adjustment between 2010–2024 of 38% is assumed [77].
6) The cost of ship design using a deepwater condenser is 66% of cold water pipe design [78].
7) The annual operating cost is 5% [79].
8) Energy subsidies for 2023 were $7 trillion USD [80].

Table 3. The historical and projected cost of OTEC and TG.

Plant size	**10**	**Conventional 100**	**100**	**1000**
Rating	**MW**	**MW**	**MW**	**MW**
$2010/kw (installed)	$16,400	$4,000	2,640	1,394
Overnight cost	$164,000,000	$400,000,000	$264,000,000	$1,393,759,224
Number of plants	3,100,000	310,000	310,000	31,000
Total cost OTEC	$508,400,000,000,000	$124,000,000,000,000	$81,840,000,000,000	$43,206,535,944,000
Inflation adjustment (38%)	$701,592,000,000,000	$171,120,000,000,000	$112,939,200,000,000	$59,625,019,602,720
Interest at 5.5% for 30 years	$701,592,000,000,000	$171,120,000,000,000	$112,939,200,000,000	$59,625,019,602,720
Principal plus interest	$1,403,184,000,000,000	$342,240,000,000,000	$225,878,400,000,000	$119,250,039,205,440
Plant life in years	30	30	30	30
Capacity	95%	95%	95%	97%
Annual operating cost	5%	5%	5%	5%
Annual cost per year	$25,848,126,315,790	$6,304,421,052,632	$4,160,917,894,737	$2,151,418,233,088
Terawatt hours	271,560	271,5560	271.560	271,560
Kilowatt hours	271,560,000,000,000	271,560,000,000,000	271,560,000,000,000	271,560,000,000,000
Cost per hour	$0.095	$.023	$.015	$0.008
Annual fossil fuel subsidy	$7,000,000,000,000	$7,000,000,000,000	$7,000,000,000,000	$7,000,000,000,000
Annual (loss) return	$18,848,126,315,790	$695,578,947,368	$2,839,082,105,263	$4,848,581,766,912

In 2022, global energy costs were 13% of a global GDP of $101 trillion [81,82]. This is 6.5 times the cost of TG, not including the IMF's estimated $7 trillion for the environmental cost of doing business burning fossil fuels.

Oil prices have reached their highest level since 2008, and higher energy prices in general have contributed to sharply increased inflation, which has led to widespread political unrest [83].

A recent study of OTEC for Indonesia shows 45 GW of OTEC capacity can be installed for a Net Present Value (NPV) of up to $23 billion (this is for conventional OTEC, which is 33% more expensive than TG), so **Table 3** is in the ballpark [84].

10.4. Operational cost and useful lifetime

The operational life of an OTEC system is estimated to be 30 years [74]. And the annual operating cost is estimated to be 5% of the capital cost [79].

10.5. The impact of interest rates

Table 3 calculates interest at 5.5% over 30 years, which equals the capital cost. The Stern Review on the Economic Effects of Climate Change, however, argued that any discounting is ethically inappropriate for a global issue like climate change. However, a minuscule discount rate of 0.1 percent per annum might be justifiable [85]. Over the 30-year life of the plants, this would total 3% of the capital cost and reduce the total cost of 31,000 plants by about $57 trillion.

10.6. Speed, can the technology be deployed in time to make a difference in the climate

Universities are failing to meet the growing demand for a clean energy workforce. Since a career may last 30–40 years, this creates a risk of long-term carbon lock-in and stranded skill sets through (mis)education [86]. Even if this wasn't the case, it will take at least 10 years of R&D and scaling from a 300-watt, closed system, that confirms the thermodynamics, confirms the movement of atmospheric CO_2 to the ocean as the surface cools, and tests various working fluids, to 10 MW, 100 MW, and 1-GW ocean going plants. After the 1-GW scale is attained, it will take another 10 years to ramp up to 1000 plants a year.

In 2022, there were 105,395 registered vessels [87]. Current worldwide shipyard capacity is about 1200–1300 ships per year, compared with about 2000 ships per year between 2005 and 2010 [88]. Seventy-five percent of these plants were built by only three countries: China, Korea, and Japan [77]. Should global warming finally, widely, be recognized as the existential threat it is, the other 192 countries of the world are likely to make a commensurate effort to solve the problem. Which would entail the production of at least 1000 1-GW ships a year.

Since the working life of these plants is 31 years, and the objective is to produce 31 TW of energy, the oldest ships would be replaced each year to maintain a stable energy supply.

10.7. Does the technology scale

According to Langer and others, it does [74,84].

10.8. Availability of resources

If there were enough resources to build 2000 ships per year between 2005 and 2010, it is reasonable to assume there are enough resources to build 1000 TG plants a year [77].

Magnesium, currently valued at about $2600/tonne, exists at a concentration of 1272 ppm in seawater, 3 times higher than the concentration of CO_2 in the atmosphere.

It is a viable metal for use in many major components, mainly heat exchangers and heat pipes in TG plants [89].

A method of precipitating magnesium from seawater has been known for over a

century and new techniques have been discovered more recently [90,91].

Magnesium alloys reduce the weight of heat-removing elements like TG heat exchangers by a third without losing efficiency [92]. With the ocean's abundance of magnesium and the technical ability to secure it, the current cost of the metal would be reduced by orders of magnitude when the metal is produced as an adjunct to energy production using the TG method.

10.9. Equity

The SIDS are the most vulnerable nations to the global warming risks of sea level rise, storm surge, and the vagaries of fossil fuel costs. But paradoxically, they control 30% of the EEZs in the most promising OTEC regions.

They could leverage these EEZs in return for free energy, among other considerations, and offer their territories as test beds for the nascent TG technology, benefiting mankind even if only inadvertently.

10.10. Fairness

The concept of a "just transition" away from fossil fuels is a concept that says to meet our climate goals, all communities, all workers, and all social groups must be brought along in the pivot to a net-zero future [93]. It is a concept designed to include and therefore bring on board as many interested parties as possible.

Workers in the fossil fuel industry would be the most impacted by a phaseout of their resource, but they also have the most experience and technology working in deepwater, so they need never suffer for a lack of jobs during and after a "just transition."

Minimizing the existing occupational health and safety risks of people working in all institutions is the main task of any occupational health and safety culture and is another milestone that TG would meet [94].

10.11. Economic analysis

Since there is no operational experience with large OTEC or TG systems, the best alternative is to take the example of a Nimitz-class aircraft carrier, which is indestructible by the elements when under power and commanded by a competent captain.

TG plants will operate exclusively within the Inter-Tropical Convergence Zone (ITCZ), in which cyclones, hurricanes, and typhoons do not occur, but where vigorous thunderstorms are interspersed with the doldrums, which are periods of calm that have stranded sailors for days or weeks.

The predicted service life of Nimitz-class aircraft carriers is about 50 years, but it is assumed that the service life of an OTEC platform is 31 years [74]. In 1997 dollars, the CapEx for the carrier was $4.1 billion, and its maintenance costs were $5.7 billion [95]. This is in line with an overnight cost of $1.4 billion for a 1-GW TG plant plus a 150% maintenance cost over 30 years.

11. Conclusion

The thermodynamics of global warming invite the conclusion that the more

energy produced by the heat of warming, the cooler the surface becomes, sustainability goals are met, and the impacts of global warming are mitigated. TG redistributes the certain accumulation of ocean heat and removes a part of it to the land in the service of as many as ten billion people. This is heat that is currently lying fallow and, in the alternative, will ultimately resurface and wreak havoc. Its use can cool the surface, and when deployed at scale, it could generate 1.6 times the world's current primary energy while removing CO_2 from the atmosphere and solving the fossil fuel replacement problem. The infrastructure is capital intensive, but this is capital that is in many cases also lying fallow and instead could be generating prodigious economic returns and climate respite [96]. To derisk this capital, a lab-scale, and small ocean-going prototype should be financed and constructed as soon as possible.

Conflict of interest: The author declares no conflict of interest.

References

1. Thapar S. Energy and Climate Change. In: Renewable Energy: Policies, Project Management and Economics. Springer; 2024. doi: 10.1007/978-981-99-9384-0_1
2. Resplandy L, Keeling RF, Eddebbar Y, et al. Quantification of ocean heat uptake from changes in atmospheric O_2 and CO_2 composition. Scientific Reports. 2019; 9(1). doi: 10.1038/s41598-019-56490-z
3. Yang H, Zhao Y, Liu Z, et al. Heat transport compensation in atmosphere and ocean over the past 22,000 years. Scientific Reports. 2015; 5(1). doi: 10.1038/srep16661
4. Lindsey R, Dahlman L. Climate change: Ocean heat content. Available online: https://www.climate.gov/news-features/understanding-climate/climate-change-ocean-heat-content (accessed on 4 April 2024).
5. Li G, Cheng L, Zhu J, et al. Increasing ocean stratification over the past half-century. Nature Climate Change. 2020; 10(12): 1116-1123. doi: 10.1038/s41558-020-00918-2
6. Zanna L, Khatiwala S, Gregory JM, et al. Global reconstruction of historical ocean heat storage and transport. Proceedings of the National Academy of Sciences. 2019; 116(4): 1126-1131. doi: 10.1073/pnas.1808838115
7. Manighetti B. Ocean circulation: the planet's great heat engine. Available online: https://niwa.co.nz/publications/water-and-atmosphere/vol9-no4-december-2001/ocean-circulation-the-planets-great-heat-engine (accessed on 4 April 2024).
8. Rogers DP. Air-sea interaction: Connecting the ocean and atmosphere. Reviews of Geophysics. 1995; 33(S2): 1377-1383. doi: 10.1029/95rg00255
9. Lock S. How big is Earth? Available online: https://www.space.com/17638-how-big-is-earth.html (accessed on 4 April 2024).
10. Cheng L, Abraham J, Trenberth KE, et al. New record ocean temperatures and related climate indicators in 2023. Advances in Atmospheric Sciences. 2024; 2024: 1-15. doi: 10.1007/S00376-024-3378-5/METRICS
11. Etheridge DM, Steele LP, Langenfelds RL, et al. Global monitoring laboratory—Carbon cycle greenhouse gases. Available online: https://gml.noaa.gov/ccgg/trends/data.html (accessed on 4 April 2024).
12. Bush E. Oceans are record hot, puzzling and concerning scientists. Available online: https://www.nbcnews.com/science/environment/oceans-record-hot-rcna143179 (accessed on 4 April 2024).
13. Pidwirny M. Global heat balance: Introduction to heat fluxes. In: Fundamentals of Physical Geography, 2nd ed. Rowman & Littlefield; 2006.
14. Angliss B. Climate science for everyone: How much heat can the air and ocean store? Available online: https://scholarsandrogues.com/2013/05/09/csfe-heat-capacity-air-ocean/ (accessed on 4 April 2024).
15. Greenaway SF, Sullivan KD, Umfress SH, et al. Revised depth of the Challenger Deep from submersible transects; including a general method for precise, pressure-derived depths in the ocean. Deep Sea Research Part I: Oceanographic Research Papers. 2021; 178: 103644. doi: 10.1016/J.DSR.2021.103644
16. von Schuckmann K, Minière A, Gues F, et al. Heat stored in the Earth system 1960-2020: where does the energy go? Earth System Science Data. 2023; 15(4): 1675-1709. doi: 10.5194/essd-15-1675-2023

17. UCAR. Transfer and storage of heat in the oceans. Available online: https://scied.ucar.edu/learning-zone/earth-system/climate-system/transfer-and-storage-heat-oceans (accessed on 4 April 2024).
18. Hassan Q, Viktor P, J. Al-Musawi T, et al. The renewable energy role in the global energy transformations. Renewable Energy Focus. 2024; 48: 100545. doi: 10.1016/j.ref.2024.100545
19. Rau GH, Baird JR. Negative-CO_2-emissions ocean thermal energy conversion. Renewable and Sustainable Energy Reviews. 2018; 95: 265-272. doi: 10.1016/j.rser.2018.07.027
20. Perez M, Perez R. Update 2022 - A fundamental look at supply side energy reserves for the planet. Solar Energy Advances. 2021; 2: 100014. doi: 10.1016/j.seja.2022.100014
21. Trenberth KE, Caron JM. Estimates of meridional atmosphere and ocean heat transports. Journal of Climate. 2001; 3433-3443. doi: 10.1175/1520-0442(2001)014<3433:EOMAAO>2.0.CO;2
22. Oh JH, Kug JS, An SI, et al. Emergent climate change patterns originating from deep ocean warming in climate mitigation scenarios. Nature Climate Change. 2024; 14(3): 260-266. doi: 10.1038/s41558-024-01928-0
23. Baird JR. CA2958456 method and apparatus for load balancing trapped solar energy. Available online: https://patentscope.wipo.int/search/en/detail.jsf?docId=CA225415072 (accessed on 4 April 2024).
24. Chan CW, Siqueiros E, Ling-Chin J, et al. Heat utilisation technologies: A critical review of heat pipes. Renewable and Sustainable Energy Reviews. 2015; 50: 615-627. doi: 10.1016/j.rser.2015.05.028
25. Liang X, Spall M, Wunsch C. Global ocean vertical velocity from a dynamically consistent ocean state estimate. Journal of Geophysical Research: Oceans. 2017; 122(10): 8208-8224. doi: 10.1002/2017jc012985
26. Warming ocean—Argo. Woods hole oceanigraphic institution. Available online: https://www2.whoi.edu/site/argo/impacts/warming-ocean/ (accessed on 10 March 2024).
27. Levitus S, Antonov JI, Boyer TP, et al. World ocean heat content and thermosteric sea level change (0-2000 m), 1955-2010. Geophysical Research Letters. 2012; 39(10). doi: 10.1029/2012gl051106
28. Vecellio DJ, Kong Q, Kenney WL, et al. Greatly enhanced risk to humans as a consequence of empirically determined lower moist heat stress tolerance. Proceedings of the National Academy of Sciences. 2023; 120(42). doi: 10.1073/pnas.2305427120
29. Wang X, Lu Y, Chen C, et al. Total-factor energy efficiency of ten major global energy-consuming countries. Journal of Environmental Sciences. 2024; 137: 41-52. doi: 10.1016/j.jes.2023.02.031
30. Nihous GC. A preliminary assessment of ocean thermal energy conversion resources. Journal of Energy Resources Technology. 2006; 129(1): 10-17. doi: 10.1115/1.2424965
31. Prueitt ML. US20070289303A1—Heat transfer for ocean thermal energy conversion—Google Patents. Available online: https://patents.google.com/patent/US20070289303A1/en (accessed on 4 April 2024).
32. Manikowski AF. Deep water condenser OTEC using carbon dioxide working fluid. In: Proceedings of "Challenges of Our Changing Global Environment"; 9-12 October 1995; San Diego, California, USA; 1995. pp. 1092-1099. doi: 10.1109/oceans.1995.528578
33. Fallis A. Waste heat recovery: Technology and opportunities in U.S. industry. Journal of Chemical Information and Modeling. 2013; 53(9): 1689-1699.
34. Zevenhoven R, Beyene A. The relative contribution of waste heat from power plants to global warming. Energy. 2011; 36(6): 3754-3762. doi: 10.1016/j.energy.2010.10.010
35. Jowit J, Espinoza J. Heatwave shuts down nuclear power plants. Available online: https://www.theguardian.com/environment/2006/jul/30/energy.weather (accessed 4 April 2024).
36. Karagiannopoulos L. In hot water: How summer heat has hit Nordic nuclear plants. Available online: https://jp.reuters.com/article/us-nordics-nuclearpower-explainer-idUSKBN1KM4ZR (accessed on 4 April 2024).
37. Haider Q. Nuclear Fusion: One Noble Goal and a Variety of Scientific and Technological Challenges. BoD-Books on Demand; 2019. doi: 10.5772/intechopen.82335
38. Norouzi N, Joda F. Exergy and stabilization design of a fusion power plant and its waste heat recovery to produce hydrogen. Available online: https://www.researchgate.net/publication/357657220_Exergy_and_stabilization_design_of_a_fusion_power_plant_and_its_waste_heat_recovery_to_produce_hydrogen (accessed on 7 March 2024).
39. Murphy TWJ. Energy and Human Ambitions on a Finite Planet. eScholarship; 2021. pp. 7-17. doi: 10.21221/S2978-0-578-86717-5
40. Arli F, Dumrul H, Taskesen E. Hydrogen Production from Solar Water Splitting Using Photocatalytic and

Photoelectrochemical Technologies. BIDGE Publ.; 2023. pp. 107-140.
41. Michaelis D. Energy island. In: Proceedings of Oceans 2003: Celebrating the Past... Teaming Toward the Future. 22-26 September 2003; San Diego, CA, USA. pp. 2294-2302. doi: 10.1109/OCEANS.2003.178267
42. EIA. Ocean thermal energy conversion—U.S. Energy Information Administration. Available online: https://www.eia.gov/energyexplained/hydropower/ocean-thermal-energy-conversion.php (accessed on 5 March 2024).
43. Rajagopalan K, Nihous GC. An assessment of global ocean thermal energy conversion resources with a high-resolution ocean general circulation model. Journal of Energy Resources Technology. 2013; 135(4). doi: 10.1115/1.4023868
44. Denholm P, Hand M, Jackson M, et al. Land Use Requirements of Modern Wind Power Plants in the United States. Office of Scientific and Technical Information (OSTI); 2009. doi: 10.2172/964608
45. Imhan N. Area Required for solar PV power plants—Suncyclopedia. Available online: http://www.suncyclopedia.com/en/area-required-for-solar-pv-power-plants/ (accessed on 4 April 2024).
46. Dumrul H, Fatih AR, Taşkesen E. Dust effect on PV modules: Its cleaning methods. In: Innovative Research in Engineering. Duvar Publishing; 2023.
47. Vega LA, Michaelis D. First generation 50 MW OTEC plantship for the production of electricity and desalinated water. Presented at the Offshore Technology Conference; May 2010; Houston, Texas, USA. doi: 10.4043/20957-ms
48. Adiputra R, Utsunomiya T, Koto J, et al. Preliminary design of a 100 MW-net ocean thermal energy conversion (OTEC) power plant study case: Mentawai island, Indonesia. Journal of Marine Science and Technology. 2019; 25(1): 48-68. doi: 10.1007/s00773-019-00630-7
49. Hurtt J, Pellen A, Nagurny J. OTEC power efficiency challenges. In: Proceedings of the Offshore Technology Conference; May 2010; Houston, Texas, USA. doi: 10.4043/20498-MS
50. Smalley RE. Future global energy prosperity: The terawatt challenge. MRS Bulletin. 2005; 30(6): 412-417. doi: 10.1557/mrs2005.124
51. Diallo MS, Kotte MR, Cho M. Mining Critical metals and elements from seawater: Opportunities and challenges. Environmental Science & Technology. 2015; 49(16): 9390-9399. doi: 10.1021/acs.est.5b00463
52. Henderson GM. Ocean trace element cycles. Philosophical Transactions of the Royal Society A: Mathematical, Physical and Engineering Sciences. 2016; 374(2081): 20150300. doi: 10.1098/rsta.2015.0300
53. harette M, Smith W. The volume of earth's ocean. Oceanography. 2010; 23(2): 112-114. doi: 10.5670/oceanog.2010.51
54. Shaterabadi M, Sadeghi S, Jirdehi MA. The role of green hydrogen in achieving low and net-zero carbon emissions: Climate change and global warming. In: Vahidinasab V, Mohammadi-Ivatloo B, Shiun Lim J (editors). Green Hydrogen in Power Systems. Springer; 2024. pp. 141-153. doi: 10.1007/978-3-031-52429-5_6
55. Dirik R, Taşkesen E, Dirik Ö. Using artificial intelligence in renewable energy sources (Turkish). Int Conf Recent Acad Stud. 2023; 1(1): 28-35. doi: 10.59287/icras.667
56. Binns C. A solution for California's wildfire safety deficit. Stanford News Service. Available online: https://news.stanford.edu/press-releases/2023/08/07/resilient-power-grids/ (accessed on 9 March 2024).
57. NASA. Joint NASA, NOAA Study finds earth's energy imbalance has doubled. Geophysical Research Letters. Available online: https://www.climate.gov/news-features/feed/joint-nasa-noaa-study-finds-earths-energy-imbalance-has-doubled (accessed on 9 March 2024).
58. International Maritime Organization. IMO 2020: consistent implementation of MARPOL Annex VI. Available online: https://www.imo.org/en/MediaCentre/PressBriefings/pages/34-IMO-2020-sulphur-limit-.aspx (accessed on 9 March 2024).
59. Hansen JE, Sato M, Simons L, et al. Global warming in the pipeline. Oxford Open Climate Change. 2023; 3(1). doi: 10.1093/oxfclm/kgad008
60. Caldwell Z. Climate Migration. CQ Press; 2023. doi: 10.4135/cqresrre20231013
61. Baird J. The Diverse Energy Potential of the Water Carrier Hydrogen. Climate CoLab; 2015.
62. USGS. Saltwater intrusion. https://www.usgs.gov/mission-areas/water-resources/science/saltwater-intrusion (accessed on 9 March 2024).
63. Roquet F, Ferreira D, Caneill R, et al. Unique thermal expansion properties of water key to the formation of sea ice on Earth. Science Advances. 2022; 8(46). doi: 10.1126/sciadv.abq0793
64. Hugonnet R, McNabb R, Berthier E, et al. Accelerated global glacier mass loss in the early twenty-first century. Nature. 2021; 592(7856): 726-731. doi: 10.1038/s41586-021-03436-z
65. Baynes K, Boening C. Ice Melt, Global sea level—NASA sea level change portal. Available online:

https://sealevel.nasa.gov/understanding-sea-level/global-sea-level/ice-melt (accessed on 9 March 2024).
66. IPCC. IPCC AR6 WGIII: CDR Factsheet. Available online: https://www.ipcc.ch/report/ar6/wg3/downloads/outreach/IPCC_AR6_WGIII_Factsheet_CDR.pdf (accessed on 11 March 2024).
67. Vidler F. Accountability for CO_2 Climate Crisis by Carbon Majors' Emissions in Oil and Gas Production? Available online: https://ssrn.com/abstract=4403449 (accessed on 11 March 2024).
68. Daily CO_2. Available online: https://www.co2.earth/daily-co2 (accessed on 11 March 2024).
69. Rau GH, Carroll SA, Bourcier WL, et al. Direct electrolytic dissolution of silicate minerals for air CO_2 mitigation and carbon-negative H_2 production. Proceedings of the National Academy of Sciences. 2013; 110(25): 10095-10100. doi: 10.1073/pnas.1222358110
70. Shepherd JM. Carbon, climate change, and controversy. Animal Frontiers. 2011; 1(1): 5-13. doi: 10.2527/af.2011-0001
71. Evans S. Direct CO_2 capture machines could use 'a quarter of global energy' in 2100. Available online: https://www.carbonbrief.org/direct-co2-capture-machines-could-use-quarter-global-energy-in-2100/ (accessed on 12 March 2024).
72. National Centers for Environmental Information, National Oceanic and Atmospheric Administration. Annual 2005 Tropical Cyclones Report. Available online: https://www.ncei.noaa.gov/access/monitoring/monthly-report/tropical-cyclones/202213 (accessed on 12 March 2024).
73. Donahue MZ. Can we capture energy from a hurricane? Available online: https://www.smithsonianmag.com/innovation/can-we-capture-energy-hurricane-180960750/ (accessed on 12 March 2024).
74. Martel L, Smith P, Rizea S, et al. Ocean Thermal Energy Conversion Life Cycle Cost Assessment, Final Technical Report, 30 May 2012. Office of Scientific and Technical Information (OSTI); 2012. doi: 10.2172/1045340
75. Vega LA. Economies of ocean thermal energy conversion (OTEC): An update. Proceedings of the Annual Offshore Technology Conference. 2010; 4: 3239-3256. doi: 10.4043/21016-MS
76. Muralidharan S. Assessment of ocean thermal energy conversion. Available online: http://dspace.mit.edu/handle/1721.1/76927#files-area (accessed on 4 April 2024).
77. Canada B of Inflation Calculator—Bank of Canada. Inflation calculator. Available online: https://www.bankofcanada.ca/rates/related/inflation-calculator/ (accessed on 13 March 2024).
78. Srinivasan N, Sridhar M, Agrawal M. Study on the cost effective ocean thermal energy conversion power plant. Presented at the 2010 Offshore Technology Conference; 3-6 May 2010; Houston, Texas, USA. doi: 10.2523/20340-MS
79. Xiao C, Gulfam R. Opinion on ocean thermal energy conversion (OTEC). Frontiers in Energy Research. 2023; 11: 1115695. doi: 10.3389/fenrg.2023.1115695
80. IMF. Fossil fuel subsidies surged to record $7 trillion. Available online: https://www.imf.org/en/Blogs/Articles/2023/08/24/fossil-fuel-subsidies-surged-to-record-7-trillion (accessed on 13 March 2024).
81. Gillespie T. Energy costs set to reach record 13% of global GDP in 2022—Bloomberg. Available online: https://www.bloomberg.com/news/articles/2022-03-16/energy-costs-set-to-reach-record-13-of-global-gdp-this-year (accessed on 13 March 2024).
82. World Bank. Gross Domestic Product 2022, PPP. Available online: https://databankfiles.worldbank.org/public/ddpext_download/GDP_PPP.pdf (accessed on 13 March 2024).
83. Gajdzik B, Wolniak R, Nagaj R, et al. The influence of the global energy crisis on energy efficiency: A comprehensive analysis. Energies. 2024; 17(4): 947. doi: 10.3390/en17040947
84. Langer J, Quist J, Blok K. Upscaling scenarios for ocean thermal energy conversion with technological learning in Indonesia and their global relevance. Renewable and Sustainable Energy Reviews. 2022; 158: 112086. doi: 10.1016/j.rser.2022.112086
85. Stern N. The stern review on the economic effects of climate change. Population and Development Review. 2006; 32(4): 793-798. doi: 10.1111/j.1728-4457.2006.00153.x
86. Vakulchuk R, Overland I. The failure to decarbonize the global energy education system: Carbon lock-in and stranded skill sets. Energy Research & Social Science. 2024; 110: 103446. doi: 10.1016/j.erss.2024.103446
87. Unctad. Review of maritime transport 2023—Chapter 2: World Shipping Fleet, Services, and Freight Rates. Available online: https://shop.un.org/ (accessed on 13 March 2024).
88. Service CR. U.S. Commercial shipbuilding in a global context. Available online: https://crsreports.congress.gov (accessed on

13 March 2024).
89. Trading Economics. Magnesium—Price—Chart—Historical Data—News. Available online: https://tradingeconomics.com/commodity/magnesium (accessed on 13 March 2024).
90. Irving L. The precipitation of calcium and magnesium from sea water. Journal of the Marine Biological Association of the United Kingdom. 1926; 14(2): 441-446. doi: 10.1017/s002531540000792x
91. Sharkh BA, Al-Amoudi AA, Farooque M, et al. Seawater desalination concentrate—A new frontier for sustainable mining of valuable minerals. npj Clean Water. 2022; 5(1). doi: 10.1038/s41545-022-00153-6
92. Coxworth B. Magnesium alloys claimed to lighten heat removal systems by one third. Available online: https://newatlas.com/materials/magnesium-alloys-heat-removal-systems/ (accessed on 4 April 2024).
93. UNDP. What is just transition? And why is it important? Available online: https://climatepromise.undp.org/news-and-stories/what-just-transition-and-why-it-important (accessed on 13 March 2024).
94. Taşkesen E, İlbeyoğlu S, Üren R. Evaluation of Coronavirus in Terms of Occupational Health and Safety. YAZ; 2023. pp. 119-139.
95. United States Government Accountability Office. NAVY AIRCRAFT cost-effectiveness of conventionally and nuclear-powered carriers. Available online: https://www.gao.gov/products/nsiad-98-1 (accessed on 4 April 2024).
96. Biden J. Remarks by President Biden in meeting on the build back better world initiative. Available online: https://www.whitehouse.gov/briefing-room/speeches-remarks/2021/11/02/remarks-by-president-biden-in-meeting-on-the-build-back-better-world-initiative/ (accessed on 15 March 2024).

EnPress Publisher, LLC

Add: 9650 Telstar Avenue, Unit A, Suite 121, El Monte, CA 91731, USA.
Email: contact@enpress-publisher.com
Web: https://systems.enpress-publisher.com